공학박사학위논문

Surface-enhanced Raman Scattering Active Plasmonic Nanoparticles for Encoding and *In Vitro/In Vivo* Multiplex Detection

인코딩과 체내/외 다중 검출을 위한 표면 증강 라만 산란 활성 플라즈모닉 나노입자에 관한 연구

2014년 2월

서울대학교 대학원

협동과정 나노과학기술전공

강 호 만

A Dissertation for the Degree of Doctor of Philosophy

Surface-enhanced Raman Scattering Active Plasmonic Nanoparticles for Encoding and *In Vitro/In Vivo* Multiplex Detection

February, 2014

by

Homan Kang

Interdisciplinary Program in Nano-Science and Technology

Graduate School of Seoul National University

Surface-enhanced Raman Scattering Active Plasmonic Nanoparticles for Encoding and *In Vitro/In Vivo* Multiplex Detection

인코딩과 체내/외 다중 검출을 위한 표면 증강 라만 활성 나노입자에 관한 연구

지도 교수 이 윤 식

이 논문을 공학박사 학위논문으로 제출함
2014년 2월
서울대학교 대학원
협동과정 나노과학기술전공
강호만

강호만의 공학박사 학위논문을 인준함
2013년 12월

위 원 장 장 정 식 (인)

부위원장 이 윤 식 (인)

위 원 정 대 홍 (인)

위 원 이 호 영 (인)

위 원 전 봉 현 (인)

ABSTRACT

Surface-enhanced Raman Scattering Active Plasmonic Nanoparticles for Encoding and *In Vitro*/*In Vivo* Multiplex Detection

(Supervisor: Yoon-Sik Lee, Ph.D.)

Homan Kang

Interdisciplinary Program in Nano-Science and Technology

College of Natural Science

Graduate School of Seoul National University

SERS (surface-enhanced Raman scattering) technology has broadened the applications of Raman spectroscopy in biomedical analysis field. Recently, we have developed SERS active nanoparticles (SERS probe/dot), which have many advantages; a lack of photo-bleaching, narrow band width and a use of single laser excitation for detection of multiple targets. They were successfully utilized in peptide encoding and identifying biological molecules *in vivo* system.

In chaper 1, simple and efficient surface-enhanced Raman scattering (SERS) based encoding method for high-throughput screening (HTS) system was discribed. Recently, the preparation and screening of compound libraries remain one of the most challenging tasks in drug discovery, biomarker

detection, and biomolecular profiling processes. So far, several distinct encoding/decoding methods such as chemical encoding, graphical encoding, and optical encoding have been reported to identify active compounds from those libraries. Peptides were synthesized on TentaGel (TG) microbead (35 μm) by using Fmoc chemistry. During peptide coupling, the TG microbeads were encoded by the combination of several kinds of SERS dots, which are physically adsorbed on the microbead surface. When the microbead was encoded by the combination of 2 kinds of the SERS dots, more than 10,000 codes can be generated. The advantages of this SERS dots based encoding method lies in the availability of a large number of Ramam active molecules which can be utilized as Raman label compounds. Moreover, a single excitation is used for the detection of multiple encodings.

In chapter 2, near-IR (NIR)-sensitive Plasmonic Au/Ag hollow-shell (HS) assemblies on the surface of silica nanospheres were described. The diameter of the HS interior was adjusted from 3 to 11 nm by varying the amount of Au^{3+} added, which resulted in a red-shift of their plasmonic extinction of Ag/Au nanoparticle toward the NIR window (700–900 nm). The red-shifted plasmonic extinction of NIR SERS dots caused enhanced SERS signals in the NIR optical window where endogenous tissue absorption coefficients are more than two orders of magnitude lower than those for ultra-violet and visible light. In particular, a single NIR SERS dot could be detected with high reproducibility owing to approximately 3×10^5 times SERS enhancement on average and a large number of SERS-active sites on single silica nanosphere.

The signals from NIR SERS dots were detectable effectively from 8-mm depth in animal tissues. Three kinds of NIR SERS dots, which were injected into live animal tissues, produced strong SERS signals from deep tissues without spectral overlap, demonstrating their potential for *in vivo* multiplex detection of specific target molecules.

In chapter 3, silver nanoshell based NIR SERS nanoprobes were described. Silver nanoshells (AgNSs) composed of a dielectric core and a silver shell are of great interest due to excellent SERS sensitivity, and to their tunable surface plasmon frequencies in the NIR spectral region, so called biological window (700-900 nm). Previous synthetic approaches to AgNS have not been satisfactory for the effective synthesis under mild conditions. Here, we first report a seedless and single-step synthetic method for bumpy AgNSs, and AgNS based NIR-sensitive SERS nanoprobes. The bumpy AgNSs were fabricated in fully extended form without using seed metals under a mild condition (1h, 25 ^{o}C) and the silver shell thickness could be easily controlled in the range of ~32 nm to ~76 nm. In particular, the NIR-SER probes, bumpy AgNSs coded with simple aromatic compounds, were capable of generating strong SERS signal from a single particle level in the NIR window (average SERS enhancement factor value 6.4 $\times 10^5$). In addition, NIR-SERS probes were successfully applied to cell tracking in living animals using a portable Raman system.

Keywords: Surface-enhanced Raman scattering, SERS active nanoparticles,

nanoprobe, cluster/assembly-based NPs, Au/Ag, hollow shell, nanoshell, bumpy nanostructure, multiplex detection, optical encoding, peptide encoding, bio-imaging, near-IR imaging, single-particle detection, cell tracking

Student number: 2007-20461

TABLE OF CONTENTS

LIST OF TABLES

Introduction

Capter 1 Optical Encoding by Using SERS Nanoparticles During Solid-phase Peptide Synthesis

No Table

Capter 2 Near-IR SERS Nanoprobes with Au/Ag Hollow-Shell Assemblies for *In Vivo* Multiplex Detection

No Table

Capter 3 Seedless Fabrication of Bumpy Silver Nanoshells for *In Vivo* Cell Tracking with Near-IR SERS

LIST OF FIGURES

Introduction

Capter 1 Optical Encoding by Using SERS Nanoparticles During Solid-phase Peptide Synthesis

Capter 2 Near-IR SERS Nanoprobes with Au/Ag Hollow-Shell Assemblies for *In Vivo* Multiplex Detection

Chapter 3 Seedless Fabrication of Bumpy Silver Nanoshells for *In Vivo* Cell Tracking with Near-IR SERS

LIST OF ABBREVIATIONS

SERS	surface-enhanced Raman scattering
HTS	high-throughput screening
TG	TentaGel
HS	hollow-shell
AgNS	silver nanoshell
RLC	Raman label compound
NP	nanoparticle
SERRS	surface-enhanced resonance Raman scattering
PEG	poly(ethylene glycol)
BSA	bovine serum albumin
QD	quantum dot
NIR	near-infrared
MRI	magnetic resonance imaging.
UV	ultraviolet
TEOS	tetraethylorthosilicate
MPTS	3-mercaptopropyl trimethoxysilane
EG	ethylene glycol
PVP	poly(vinyl pyrrolidone)
HOBt	1-hydroxybenzotriazole
DIEA	*N, N*-diisopropylethylamine
BOP	(benzotriazol-1-yloxy)-tris(dimethylamino)phosphonium hexafluorophosphate
NMP	*N*-methylpyrrolidone
BT	benzenethiol
4-MT	4-mercaptotoluene

2-NT	2-naphthalenethiol
4-ATP	4-aminothiophenol
4-IBT	4-isopropylbenzenethiol
3, 5-DMT	3, 5-dimethylbenzenthiol
3, 4-DMT	3, 4-dimethylbenzenthiol
4-MOBT	4-methoxybenzenethiol
3, 4-DMOBT	3, 4-dimethoxythiophenol
3, 5-DMOBT	3, 5-dimethoxythiophenol
4-CBT	4-chlorobenzenethiol
2-CBT	2-chlorobenzenethiol
3, 4-DCT	3, 4-dichlorobenzenethiol
3, 5-DCT	3, 5-dichlorobenzenethiol
2-FBT	2-fluorobenzenethiol
4-FBT	4-fluorothiophenol
4-BBT	4-bromobenzenethiol
2-BBT	2-bromobenzenethiol
2-MMP	2-mercapto-6-methylpyridine
2-MMI	2-mercapto-1-methylimidazole
2-MBI	2-mercapto-5-methylbenzimidazole
5-PHTT	5-phenyl-1H-1,2,4-triazole-3-thiol
2-ATFT	2-amino-4-(trifluoromethyl)benzenethiol
2-ACBT	2-amino-4-chlorobenzenethiol
3-MBA	3-mercaptobenzoic acid
4-NPDSF	4-nitrophenyl disulfide
PITC	phenyl isothiocyanate
3-CBA	3-cyanobenzoic acid
4-CBAL	4-cyanobenzylaldehyde
4-PPD	4-(pyridine-4-yl)pyridine

Fmoc	9-fluorenylmethoxycarbonyl
Fmoc-Rink linker	*p*-[(R,S)-α-[1-(9H-fluoren-9-yl)-methoxyformamido]-2,4-dimethoxybenzyl]-phenoxyacetic acid
SEM	scanning electron microscope
TEM	transmission electron microscope
SERS dot	SERS active nanoparticle
OA	octylamine
Ag-NPA	Ag nanoparticles-assembled silica nanosphere
Au/Ag HSA	Au/Ag hollow-shell assembled silica nanospheres
DI water	deionized water
NA	numerical aperture
EF	enhancement factor
FEM	finite element method
FDTD	finite difference time domain
HR-TEM	high resolution-transmission electron microscopy
EDX	energy dispersive X-ray spectroscopy
HAADF-STEM	high angle annular dark field-scanning transmission electron microscopy
DTTC	3,3'-diethylthiatricarbocyanine iodide
mPEG-SH	methoxy poly(ethylene glycol) sulfhydryl
A549 cells	adenocarcinomic human alveolar basal epithelial cells
FBS	fetal bovine serum
MTT	3-(4,5-dimethylthiazol-2-yl)2, 5-diphenyltetrazolium bromide
DMSO	dimethylsulfoxide
ELISA	enzyme-linked immunosorbent assay
fcc	face-centered-cubic
XRD	X-ray diffraction
SiNP	silica nanosphere
AgNS	silver nanoshell

Surface-enhanced Raman Scattering Active Plasmonic Nanoparticles for Encoding and *In Vitro*/*In Vivo* Multiplex Detection

Introduction

1. General Introduction

1.1 Design of SERS Active Nanoparticles (SERS Nanoprobes)

Surface-enhanced Raman scattering (SERS) is an ultra-sensitive vibrational spectroscopic technique for probing molecules on the surface of plasmon-resonant nanostructures.[1] The SERS effect can increase the Raman high signal intensity by up to 10^{14} times, which can allow signal sensitivity to detect even a single molecule.[2,3] The extra-ordinary signal enhancement is attributed to two mechanisms: a highly-localized effect of the electromagnetic field near the metal surface[4,5] and a chemical resonance effect.[6-8] The former is attributed to 10 to 11 orders of enhancement while the latter explains the 2 to 4 orders of enhancement.[9]

SERS spectroscopy shows a great potential as a multiplex detection tool due to efficient excitation and detection of various distinct Raman labels and the narrow bandwidth of <1 nm.[10-13] SERS spectroscopy also has several advantages such as high signal-to-noise ratio, non-photobleaching features and its use of single photo-excitation.[14-16] After the first SERS-active

nanoparticles (called as SERS nanoprobes/labels/tags) were reported by the Tarcha group,[17] they have become an alternative to fluorescence-based labels in the field of detection of biological molecules *in vivo*[18-32] as well as *in vitro*[33-40]. The SERS nanoprobes are composed of three parts: metallic SERS substrate, organic Raman label compound (RLC), and a protective layer or shell (Figure I). As SERS substrate with the desired optical properties and signal enhancement, various metal nanostructures such as nanospheres,[10,18,21,23,26,34,36,37,41] nanoshells,[13,42-45] nanorods,[25,29,46-48] nanocubes,[49-52] multi-branched nanoparticles (NPs),[53-58] cluster/assembly-based NPs,[59-66] and bimetallic NPs[67-69] have been reported (Figure II). Among these particles, gold and silver nanospheres are most widely used as SERS substrate, which have maximum plasmonic bands around 400-600 nm, because this plasmonic band is in resonance with the wavelength of common illuminating lasers.[70] The geometry and chemical composition can influence the Raman enhancement. Specially designed structures were considered to generate stronger SERS signals and red-shifted plasmonic bands to near-IR region for *in vivo* SERS detection. Especially, the desired optical properties and previously reported SERS substrates for *in vivo* multiplex detection will be explained in the Section 3.

Fluorescence dye molecules, which consist of resonant aromatic rings

and an affinity group to metal surface, are generally used as Raman label compounds/reporter molecules. These fluorescence dyes give rise to extra signal enhancement compared with electronically non-resonant molecules because the fluorescence dye have an additional resonance Raman effect (SERRS, surface-enhanced resonance Raman scattering).[1] However, fluorescence dyes have limitation for multiplex detection becuase of complicated Raman signatures. Therefore, simple and symmetric RLCs have been used to avoid spectral overlapping. The requirements of RLC for multiplex detection will be discussed in the next section 1.2. In order to prevent desorption of RLC and colloidal aggregation, various encapsulation materials such as silica,[23,36,37,54,59,60,65,71] poly(ethylene glycol) (PEG),[18,24,25,72] bovine serum albumin (BSA),[11,26,27,58,73] and so on are generally used as protective shell/layer. The protective shell also can provide water compatability and subsequent bioconjugation functionalities. Although thiolated-PEG coating is widely used due to very simple coating procedure, the PEG does not provide high mechanical property under harsh conditions. The silica shell is beneficial for high mechnical and chmical stability. However, the silica shell coating step is a relatively complicated one and causes an undesirable agrregation. Organo-silane compounds for silica shell and heterobifunctional PEG spacer can be used for the further

bioconjugation step. A chose of each component for aimed SERS nanoprobe is very important in designing and preparation of congruous properties and applications.

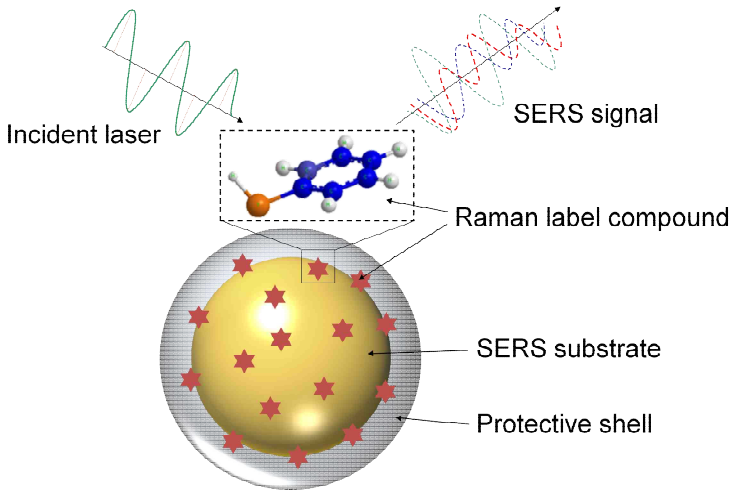

Figure I. Schematic illustration for components of typical SERS nanoprobes: SERS substrate, Raman label compounds, and protective shell.

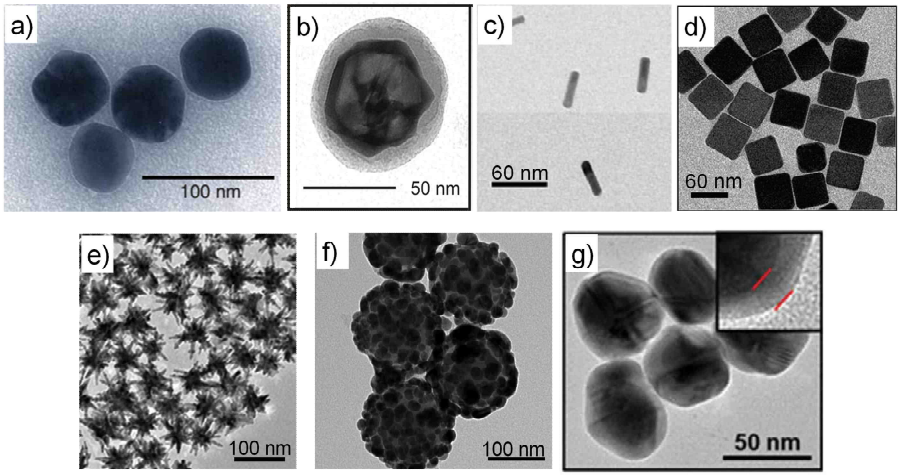

Figure II. Typical TEM images of various SERS substrates. a) nanospheres (here: gold nanosphere),[18] b) nanoshells (here: Au/Ag nanoshell),[43] c) nanorods (here: gold nanorod),[25] d) nanocubes (here: silver nanocube),[52] e) multi-branched NPs (here: gold nanostar),[58] f) cluster/assembly-based NPs (here: silver NPs assembled silica),[60] and g) bimetallic NPs (here: Au-Ag core-shell NP).[69]

1.2 Multiplexing Capability of SERS Nanoprobes

In recent years, a bioanalysis/assay of biomolecules such as nucleic acids and proteins relies on multiplex detection because a single label-based analysis is unlikely to provide sufficient information for precise diagnosis and high-throughput screening.[22,74,75] Generally, the term multiplexing refers to the parallel determination of serveral unique parameters within a single experiment.[15] The multiple identification can be accomplished by utilizing characteristic signatures of the multiple labels coded to tracer molecules or microbead/suspension array. Among optical labeling materials, fluorescenece dye and semiconducter nanocrystals (called as quantum dots, QDs) are well known labeling agents. However, the luminescence based optical probes are limited to use because the number of available distinct signals for multiplex detection is small due to broad bandwidth causing signal overlap. More recently, SERS active nanoparticles has been an overwhelming interest in multiplex detection both of *in vitro* and *in vivo* because SERS labeling technique offer many advantages compared with other optical nanoprobes. The superior features of SERS labeling technique in multiplex detection are as follows: a high multiplexing capability due to a narrow width of vibrational Raman bands (even less than 1 nm full width at half maximum)[35,65,75]; from a

practical point of view, only a single laser line excitation is required for simultaneous excitation of the various distinct SERS nanoprobes[75]; and the laser line can be chosen with large freedom depending on the spectral region of the SERS substrate and the chemical resonance condition if surface-enhanced resonance Raman scattering (SERRS) is utilized.[16] Figure III shows a narrow bandwidth of SERS nanoprobe signal in comparison to those of fluorescence dye and QD.

The multiplexing capability of the SERS nanoprobes comes from the unique signatures of each RLC with narrow bandwidth. Therefore, a choice of RLC is one of the important processes for preparing SERS nanoprobes in multiplexing analysis. Considering points of RLC for multiplex detection are as follows: a small number of atoms and high symmetry, leading to a minimal number of Raman bands to avoid signal overlap of labels; surface-seeking groups for chemisorption onto the metal surface; high Raman scattering cross sections for high signal levels; and low or no photobleaching for signal stability.[1,16,70]

Simple aromatic compounds were used for multiplex detection due to the simplicity of Raman signatures. Porter and co-workers have used arylthiols (thiophenol, 2-naphthalenethiol, and 4-mercaptobenzoic acid) as RLCs to demonstrate dual-analyte sandwich type immunoassay. The detection

antibodies were conjugated to gold colloids that are labeled with different RLCs (called as Raman labeled immuno gold NPs), which serve as extrinsic labels for each type of antibody. The presences of each specific antigen were detected simultaneously with the distint SERS signatures of the RLCs (Figure IV).[34] The Irudayaraj group has also demonstrated simultaneous identification of up to eight SERS probes in a mixture, and four-plex detection of DNA using gold NPs with non-fluorescent RLCs (Figure V).[10,76] Although non-fluorescent RLCs have relatively high multiplex capability, it has still complicated signatures and needs sophisticated deconvolution methods to extrapolate possible signatures/valuable information from a mixture spectrum.

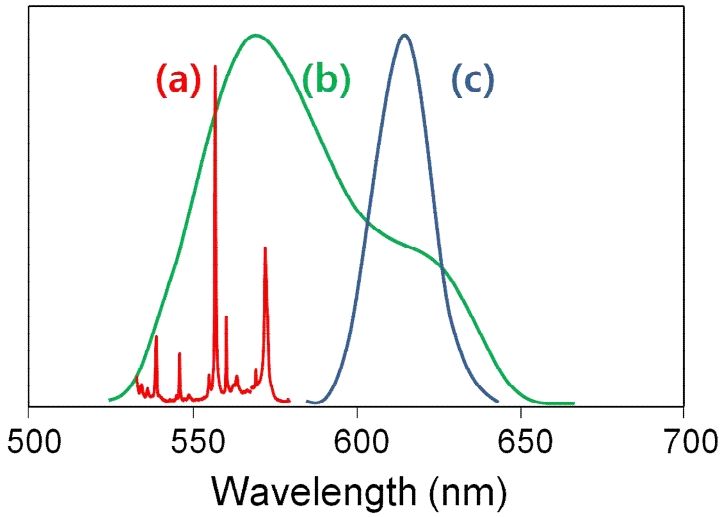

Figure III. Comparison of optical signals; (a) Raman scattering, (b) fluorescence of dye, and (c) photo-luminescence of quantum dot.

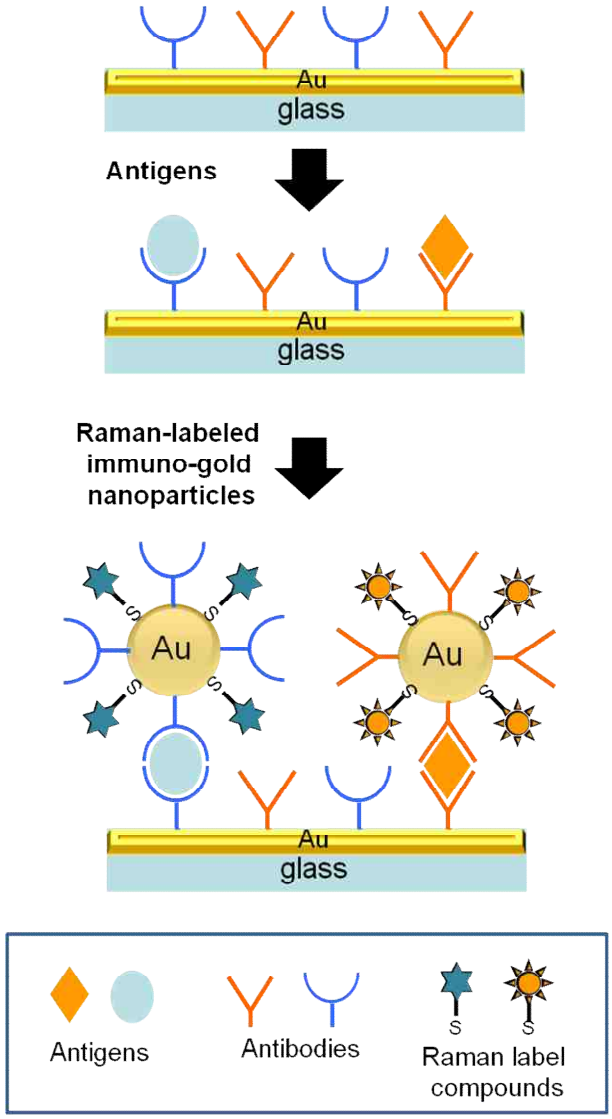

Figure IV. Surface-enhanced Raman scattering-based immunoassay.[34]

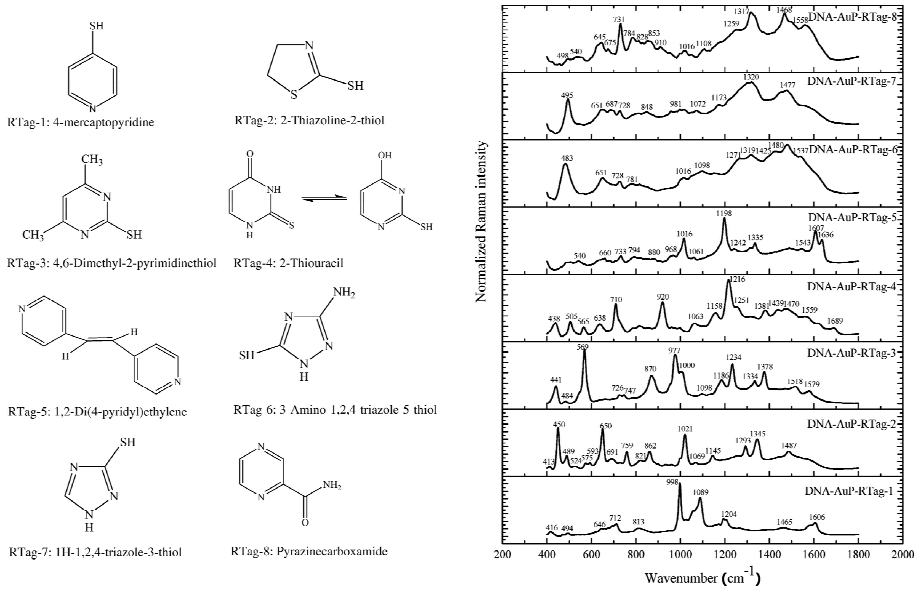

Figure V. Structures of non-fluorescent Raman label compounds (left) and their SERS spectra (right).[10]

2. Optical Encoding Methods for Chemical Library and High-Throughput Detection

The preparation and screening of large chemical libraries remain one of the most challenging tasks in drug discovery process, multiplexed disease biomarker detection, and biomolecular profiling process.[77,78] Especially, solid-phase combinatorial synthesis has been widely utilized for creating enormous amounts of chemical libraries using amino acids, sugars, and nucleic acids and optimizing the lead compounds.[77-81] However, it is very challenging to simply and rapidly identify each compound on solid supports. To write codes on polymer beads, several distinct encoding methods have been reported such as chemical encoding, graphical encoding, and optical encoding.[82,83] In chemical encoding, the polymer beads are encoded by attaching detectable molecular tags, such as oligonucleotide, haloaryls, trityls, fluorescence dyes.[84] This encoding method, however, needs compatible tags and tag synthesis reactions that may cause artifacts against the library synthesis. In addition, the laborious procedures are required to analyze the molecular tags for the compound identification. Alternative graphical and optical encodings including the use of pre-encoded microparticles[85-88] have been reported, which can be directly decoded without cleavage of ligands. In graphical encoding, microparticles are

distinguished based on their shape or internal pattern of optical elements,[89] which can be modulated using lithographic microfabrication processes[90,91] or selective photobleaching/curing[92,93]. Stripe rods,[94,95] ridged particles,[96] and dot-patterned particles[90,96,97] have been reported as graphically encoded paticles. Doyle's group has presented a method based on continuous-flow lithography that combines dot-patterned particle synthesis and probe incorporation into a single process to generate multifuctional encoded particles bearing over a million unique codes (Figure VI).[97] Optical encoding commonly relies on specific color or spectroscopic information of light emitted from several optical materials such as fluorescence dyes[98-101] or quantum dots (QDs)[102,103] photonic structures[104,105] and Raman tags[86-88]. Nie's group has reported optical coding technology based on QDs entrapped into polystyrene microbeads by solvent swelling methods.[103] In theory, six colors at six different intensities would yield around 40,000 different codes, but in pratice overlap between the different intensities is a major limitation.[82] In addition, these encoding methods suffur from several technical drawbacks such as (i) massive parallel coding is not available to make "encoded particle", (ii) the encoded beads, which is initially non-biocompatible, are required to functionalize, (iii) sequential attachment bio-ligand is needed, and (iv) the decoding process is not suitable for automation because slow to read the complicated codes and

the orientation of encoded particle must be determined before decoding process.

For combinatorial library encoding, Trau and colleagues have developed "colloidal barcoding" method, which invoves attaching fluorescently encoded microparticles to polymer beads during a split-and-mix synthesis (Figure VII).[98,100,101,106] However, a novel encoding method, which imparts a high signal to noise ratio, a large number of codings with high resolution and photostable signals, is still required for the easy and rapid identification of large chemical libraries on polymer beads. Therefore, it is very challenging to encode simply on the polymer beads and to decode directly, and rapidly during combinatorial synthesis of chemical library.

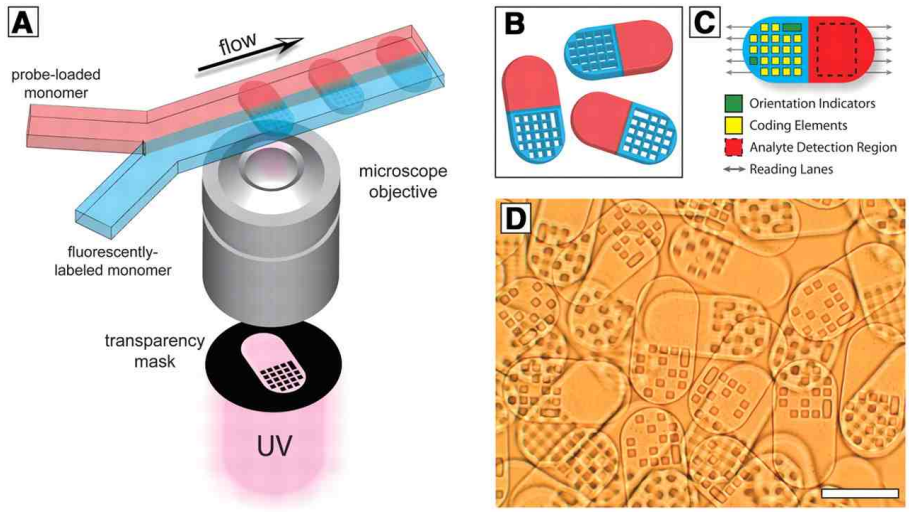

Figure VI. Graphical encoded microparticles; (a) schematic diagram of dot-patterned particles synthesis with flow lithography, and (b) half-fluorescent particles. (c) Diagrammatic representation of particle features for encoding and analyte detection. (d) Image of encoded microparticles.[97]

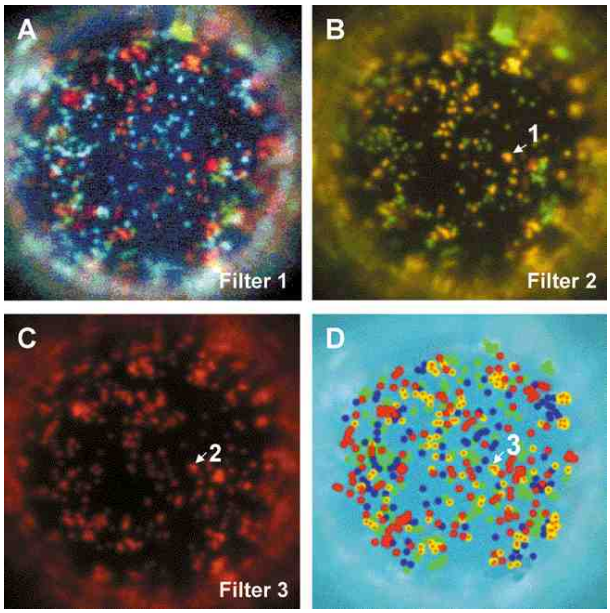

Figure VII. Fluorescence microscopy images of the colloidal barcodes that identifies the chemical structure of the compound on a single bead.[98]

3. SERS Active Nanoparticles for *In Vivo* Application

Molecular imaging holds a great potential as a tool for discovering the basic functions of biological molecules and the mechanism of various diseases.[107,108] Among various molecular imaging techniques, optical imaging has gained much attention in biology, medicine, and nanobiotechnology fields due to several advantages such as the lack of a radioactivity hazard, higher sensitivity, improved spatial resolution, and better high-throughput capability.[109,110] However, *in vivo* optical imaging applications have been hampered by low penetrating capability of optical signals as in the case of organic fluorescent dyes against animal's deep tissues of emanating autofluorescence, resulting in lowering sensitivity and signal reproducibility.[107-110] Optical probes producing signals in the near-infrared (NIR) window region (~700–900 nm), where endogenous tissue absorption coefficients are more than two orders of magnitude lower than those for ultra-violet and visible light, have been considered suitable candidates for *in vivo* applications.[111] Several types of optical probes emitting NIR photoluminescence such as NIR fluorescence dyes,[112,113] carbon nanotubes,[114-116] and quantum dots (QDs)[117,118] have been used to detect and image biomolecules *in vivo*. However, they still have some

limitations due to the limited number of distinct fluorescence signals in the NIR window, photobleaching, and cytotoxicity.[18,22]

Surface-enhanced Raman scattering (SERS) spectroscopy has received growing interest in the field of optical imaging and detection of biological molecules *in vivo*[18-28] as well as *in vitro*[36-39,41,59,65,119-125]. SERS spectroscopy shows great potential as a multiplex detection tool *in vivo* due to efficient excitation and detection of various distinct Raman labels in the NIR window and the narrow bandwidth of <1 nm.[10,11,13,43] SERS spectroscopy also has several advantages such as high signal-to-noise ratio, non-photobleaching features and its use of single photo-excitation.[14-16] Several SERS nanoprobes have been developed for *in vivo* SERS imaging and therapeutic applications as alternatives to organic fluorescent dyes or QDs. In particular, for successful applications of SERS technology to *in vivo* detection and imaging, as above mentioned, SERS-active nanostructures must not only be effectively excited inside the deep tissues of living animals but also their signals must come out of the deep tissues for detection. In this regard, it is very important to tune the plasmonic absorption bands of nanostructures toward the NIR spectral region.[21,22,24-28,60,111,126-128] Therefore, a strategy to design NIR-active nanostructures which are able to maximize the SERS

signals by absorbing NIR excitation light remains crucial for practical applications of SERS technologies *in vivo*.

Nie's group have first reported tumor targeting and non-invasive SERS imaging using 60 nm colloidal Au NPs (Figure 8).[18] In their approach, Au NPs were encoded with NIR dyes as RLCs and stabilized by thiol-modified PEG. The tumor-targeting with antibody-conjugated SERS nanoprobes was demonstrated in human cancer cells and a xenograft tumor in mice *via* tail vein injection. Since then, to enhance the sensitivity of SERS nanoprobes in *in vivo* application, several approaches have been presented. For instance, optically tuned SERS substrates involving nanoshells,[42-44] nanorods,[29,46,47] nanostars,[53,54,58] and cluster/assembly-based NPs[59-64] have been developed to create NIR-active hot spots. These NIR SERS nanoprobes are summarized in Table I. In addition, Raman label compounds, which are more active in the NIR window, have been developed using a combinatorial synthesis technique for *in vivo* detection of biological molecules.[26,27]

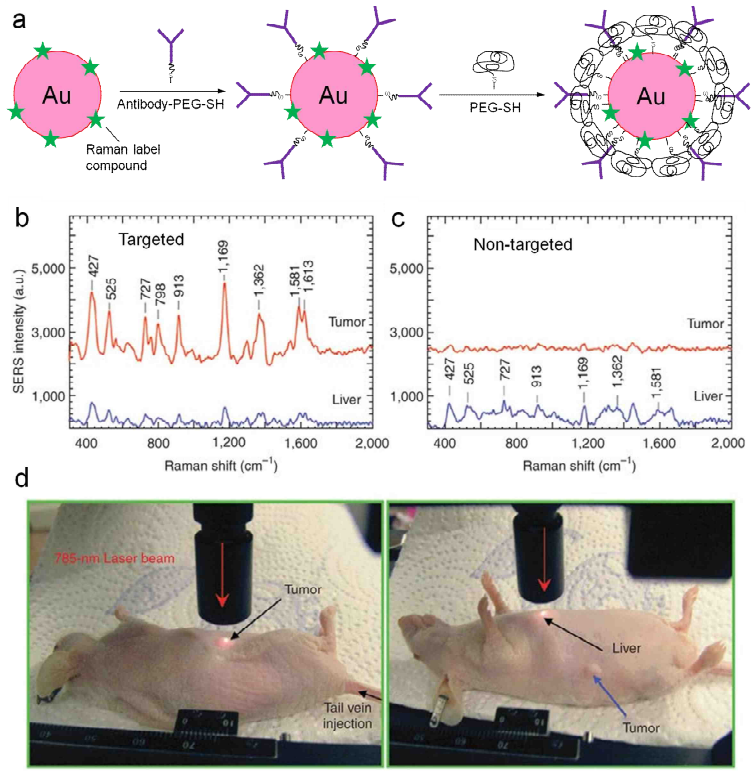

Figure VIII. First reported SERS nanoprobes for *in vivo* tumor targeting and SERS detection. (a) Preparation of PEGylated gold nanoparticle SERS tags. SERS spectra obtained from a tumor and a liver by using (b) targeted and (c) nontargeted PEGylated gold nanoparticle SERS tags. The particles were administered via a single tail vein injection. SERS spectra were obtained 5 h after the injection. (d) Photographs showing a laser beam focused on the tumor site (left) or the anatomical location of the liver (right).[18]

Table I. SERS Nanoprobes for *In vivo* Application[a]

SERS substrate	Raman label compound	Protective shell/layer	Main characteristics and advantages	Multiplex capacity	Ref
Au NPs	Commercial NIR dye	PEG	First *in vivo* tumor targeting	1	18
Au NPs	Small aryl compounds	Silica	Large multiplex capability	10	22,23
Au nanorods	Commercial NIR dye	PEG	RLC screening, thermal therapy	3	25
Au NPs	Small aryl compounds	No shell	Biodistribution study using zebrafish embryo	2	21
Au nanorods	Commercial NIR dye	PEG or silica	Dual imaging modality (fluorescence)	1	24,29
Au NPs	Synthetic NIR dye	BSA	RLC combinatorial synthesis and screening	3	26,27
Iron oxide /Au NPs cluster	Commercial NIR dye	PEG	Dual imaging modality (MRI)	1	28
Au/Ag hollow prism	Commercial NIR dye	PEG	Substrate screening, thermal therapy	3	129

[a]Abbreviations: NPs, nanoparticles; NIR, near infrared; RLC, Raman label compound; PEG, poly(ethylene glycol); BSA, bovine serum albumin; MRI, magnetic resonance imaging.

3.1 Nanoshell Composed of Dielectric/hollow Core and Metal Shell

Noble metal nanoshells (NSs) composed of a dielectric/hollow core and a metal nanoshell are of great interest due to their tunable surface plasmon frequencies from the ultraviolet (UV) to the NIR region (*ca*. 400–1200 nm)[12,130-132] by varying their core size, shell thickness, and composition, indicating that they can be good candidates as SERS-sensitive substrates in the NIR optical window (Fig 9).[12,15,42,130,131] Among various metal NSs, gold and silver metal NSs have been considered as proper SERS-active substrates for the sensitive detection of target molecules due to the considerable amplification of Raman signals by the strong electromagnetic field.[44,45] In case of metallic hollow-shell structures, the galvanic replacement reaction, which is a well-established method for preparing hollow-shell (HS), has ability to finely tune the extinction bands of the Au/Ag HS.[132,133] However, strategies for creating nanostructures with SERS hot-spots for signal amplification in NIR window, which are simple, reproducible and scalable, are still required for effective multiplex bio-imaging and *in vivo* detection of targets. Therefore, designing SERS nanoprobes that are ultra-sensitive in the

NIR window region is worth to pursue for effective *in vivo* and multiplex detection of biological molecules.

Previously, several synthetic methods for the fabrication of silver NS including multi-step layer-by-layer deposition,[134-136] the two-step seed-growth process,[45,131,137-145] and the sonochemical process[146] have been reported. However, the previous approaches have not been satisfactory for the effective synthesis of fully covered silver NS under mild conditions.[45,131,135,137-140,143-150] In particular, the two-step seed-growth method for silver NS generally involves the self-assembly of a seed metal (gold or palladium) and the subsequent seed-mediated silver growth at relatively high temperature (80 ^{o}C). However, even a thin layer of different seed metals can strongly dampen the plasmonic resonance of silver metal.[138] In addition, this strategy often suffers from the time-consuming multi-step procedure and it is difficult to control the thickness of the silver shell for plasmonic absorption in a desired electromagnetic spectrum such as an NIR window. Hence, a simple and reproducible approach without seed metals for the synthesis of uniform sized silver NS with NIR plasmonic absorption remains important. In addition, the deposition of rough silver shells in which stronger near-field enhancement in the vicinity of metal nanoparticles can be induced is more

desirable than that of smooth silver shells for sensitive SERS detection.[44,134,151]

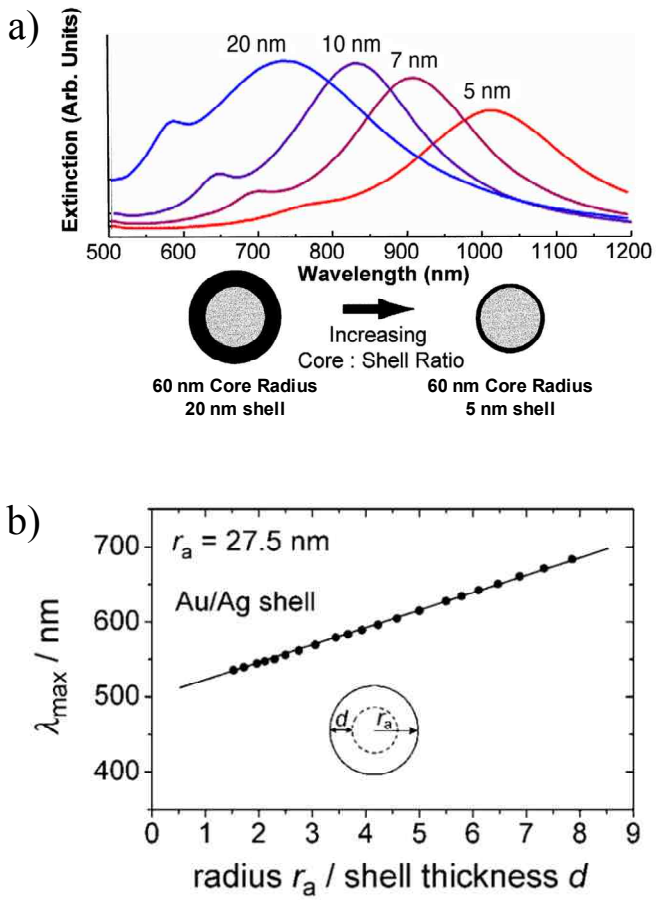

Figure IX. Tuneable surface plasmon resonance band of metal nanoshells. (a) Theoretically calculated optical resonances of metal nanoshells (silica core, gold shell) over a range of core radius/shell thickness ratios.[130] (b) Position of the plasmon band for Au/Ag nanoshells in water as a function of shell thickness d for a constant radius of r_a=27.5 nm.[15]

4. Research Objectives

In chapter 1, an encoding method for peptide libraries with surface-enhanced Raman spectroscopic nanoparticles (SERS dots) is described. The SERS dots are chemically and physically adsorbed on the microbead surface during peptide synthesis to encode the corresponding each amino acid. SERS dots-based peptide encoding permits a large number of codings with high resolution and photostability encoding, and easy and rapid decoding by simple Raman spectroscopy on the microbeads.

In chapter 2, an approach to develop NIR-sensitive SERS nanoprobes (NIR SERS dots) consisting of the plasmonic Au/Ag hollow-shells (HS) assembled silica nanospheres (Au/Ag HSA) and simple aromatic compounds for *in vivo* multiplex detection was described. The plasmonic band of the Au/Ag HS assemblies was modulated by using a galvanic replacement reaction, which resulted in a red-shift of their extinction bands from the visible (480 nm) to the NIR region (825 nm). The red-shifted plasmonic extinction of NIR SERS dots enables them to produce more enhanced SERS signals at NIR excitation window (785 nm) than at the visible excitation window (532 nm). The NIR SERS dots produced reproducible and strong NIR-active SERS signals sufficient for single particle detection, which

cannot be obtained with single spherical Au NPs. The NIR SERS signals from these probes were detectable from 8 mm depth of animal tissues due to these features. Finally, the NIR SERS dots were successfully applied for *in vivo* multiplex detection by injecting them into live animal tissues, which demonstrated their potential for multiplex detection of specific targets *in vivo*.

In chapter 3, the seedless and single-step synthetic strategy for the thickness-controllable and reproducible fabrication of bumpy silver nanoshells (AgNS) was described. They show the plasmonic resonance bands in the NIR region. This new approach enables us to quickly synthesize AgNS with a uniform bumpy surface in a single-step without seed deposition under a mild condition (1 h, 25 ^{o}C). AgNS-based NIR-SERS probes were also designed by incorporating Raman labels and biocompatible polymers on the AgNS surface for effective tracking of cells in living animals with SERS spectroscopy.

Chapter 1 Optical Encoding by Using SERS Nanoparticles for Screening of Solid-phase Peptide Library

1. Experimental Section

1.1 Chemicals and materials

Tetraethylorthosilicate (TEOS), 3-mercaptopropyl trimethoxysilane (MPTS), ethylene glycol (EG), poly(vinyl pyrrolidone) (PVP), *N, N*-diisopropylethylamine (DIEA), *N*-methylpyrrolidone (NMP), benzenethiol (BT), 4-mercaptotoluene (4-MT), 2-naphthalenethiol (2-NT), 4-aminothiophenol (4-ATP), 4-isopropylbenzenethiol (4-IBT), 3, 5-dimethylbenzenthiol (3, 5-DMT), 3, 4-dimethylbenzenthiol (3, 4-DMT), 4-methoxybenzenethiol (4-MOBT), 3, 4-dimethoxythiophenol (3, 4-DMOBT), 3, 5-dimethoxythiophenol (3, 5-DMOBT), 4-chlorobenzenethiol (4-CBT), 2-chlorobenzenethiol (2-CBT), 3,4-dichlorobenzenethiol (3, 4-DCT), 3, 5-dichlorobenzenethiol (3, 5-DCT), 2-fluorobenzenethiol (2-FBT), 4-fluorothiophenol (4-FBT), 4-bromobenzenethiol (4-BBT), 2-bromobenzenethiol (2-BBT), 2-mercapto-6-methylpyridine (2-MMP), 2-mercapto-1-methylimidazole (2-MMI), 2-mercapto-5-methylbenzimidazole (2-MBI), 5-phenyl-1H-1,2,4-triazole-3-thiol (5-PHTT), 2-amino-4-(trifluoromethyl)benzenethiol (2-ATFT), 2-amino-4-chlorobenzenethiol (2-ACBT), 3-mercaptobenzoic acid (3-MBA), 4-nitrophenyl disulfide (4-NPDSF),

phenyl isothiocyanate (PITC), 3-cyanobenzoic acid (3-CBA), 4-cyanobenzylaldehyde (4-CBAL) and 4-(pyridine-4-yl)pyridine (4-PPD) were purchased from Sigma-Aldrich Inc. and used without further purification. TentaGel^{TM} microbead (0.25 mmol NH_2/g, 35 μm) was purchased from Rapp Polymere (Tübingen, Germany). Fmoc-amino acids were purchased from BeadTech Inc. (Seoul, Korea). 1-Hydroxybenzotriazole (HOBt), (benzotriazol-1-yloxy)-tris(dimethylamino)phosphonium hexafluorophosphate (BOP) were purchased from GL Biochem Ltd. (Shanghai, China).

1.2 Preparation of Ag Nanoparticle Coated Silica Nanospheres

Tetraethylorthosilicate (TEOS, 1.6 mL) was dissolved in 40 mL of absolute ethanol into which a 3 ml portion of aqueous ammonium hydroxide (27 %) was added. The resulting mixture was vigorously stirred using magnetic bar for 20 h at 25 ^{o}C. The silica nanoparticles (NPs) were centrifuged and then washed with ethanol several times to remove the excess reagents. These silica NPs were then functionalized with thiol group. Silica NPs (300 mg) were dispersed in 6 mL ethanol containing 60 μL of MPTS and 150 μL of aqueous ammonium hydroxide (27 %). The mixture was stirred for 12 h at 25 ^{o}C. The resulting MPTS-treated silica NPs were centrifuged and washed with ethanol several times. A 100 mg portion of MPTS-treated silica NPs was thoroughly dispersed in 100 mL of $AgNO_3$ solution (3 mM in ethylene glycol). An 82.7 μL portion of octylamine (5 mM) was then rapidly added into the dispersed MPTS-treated silica NPs. The resulting dispersion was stirred for 1 h at 25 ^{o}C. Afterwards, the Ag NP-embedded silica NPs were centrifuged and washed with ethanol several times for purification.

1.3 Fabrication of SERS Active Nanoparticles (SERS dots)

A 500 μL portion of MPTS (0.2 M in ethanol) and 250 μL of Raman label compound (0.2 M in ethanol) were simultaneously added into 10 mg of Ag NP-embedded silica NPs. The resulting dispersion was shaken for 1 h at 25 ^{o}C. The Ag NP-embedded silica NPs, bearing both MPTS and Raman label compound, were centrifuged and washed with ethanol several times. To encapsulate Ag NP-embedded silica NPs with silica shell, the Ag NP-embedded silica NPs were dispersed in 15 mL of poly(vinyl pyrrolidone) solution (0.02 wt% PVP, M_w 40,000) and sodium silicate aqueous solution (7.2 mL, 0.03 wt% SiO_2). The dispersion was stirred with a magnetic bar for 20 h at 25 ^{o}C. Ethanol (60 mL) was added to the reaction mixture while mixing vigorously with magnetic bar and then the dispersion was stirred for additional 6 h for the formation of a thin silica shell. Finally, 250 μL of aqueous ammonium hydroxide (27 %) and 40 μL of TEOS were added to the reaction mixture and were stirred for 24 h at 25 ^{o}C. Finally, SERS dots were centrifuged and washed with ethanol several times.

1.4 Encoding Tripeptides with SERS dots on Microbeads

The peptide was synthesized on Fmoc-Rink amide-TentaGel™ (100 mg, Fmoc-Rink-TG) resins using conventional Fmoc chemistry accompanied by SERS dot encoding. After removing the Fmoc group from Fmoc-Rink-TG resin with 20% piperidine/NMP for 10 min, Fmoc-amino acid (3 equiv) was coupled to the free amino group using BOP (3 equiv., 25.2 mg), HOBt (3 equiv., 7.7 mg) and DIEA (3 equiv., 13.6 μL) in NMP (0.5 mL) for 1 h at 25 ^{o}C. The first amino acid-loaded resin was washed serially with NMP, DCM and MeOH. After removing Fmoc group from the first amino acid with 20% piperidine/NMP, one type of SERS dot (final concentration: 0.3 wt% to resin) was added to the resin suspension to encode the first amino acid. The resulting mixture was shaken for 5 min at 25 ^{o}C. The SERS dots that was not absorbed, were removed by filtration. This process which involves coupling of amino acids and subsequent encodings with SERS dots was repeated.

1.5 Raman Instrument

A micro-Raman system (JY-Horiba, LabRam 300) was utilized for the Raman measurement. The signal was collected by a ×10 objective lens (Olympus, 0.40 NA), and a ×100 objective lens (Olympus, 0.90 NA) with the back-scattering geometry equipped with a thermoelectrically cooled CCD detector. The 514.5 nm laser line from a continuous wave Ar ion laser (Melles Griot, 35-MAP-321) was used for the micro Raman measurements. The laser power at the sample was 7.0 mW with a ×10 objective lens. In the case of using a ×100 objective lens, the laser power at the sample was 1.0 mW, the acquisition time was 10 s, and the beam diameter size was 1 μm.

1.6 Barcode Presentation Method

We presented barcode diagram using the SERS spectrum of 4-BBT as an example. (Figure 1-1) First, relevant marker bands (492, 722, 1071, 1179, and 1585 cm^{-1}) were selected. Then, selected marker bands were normalized to the most intense Raman band (1071 cm-^{1}). The barcode x_i was finally presented from integration values of the Raman intensities I(x) around the Raman bands with full width at half maximum (FWHM).

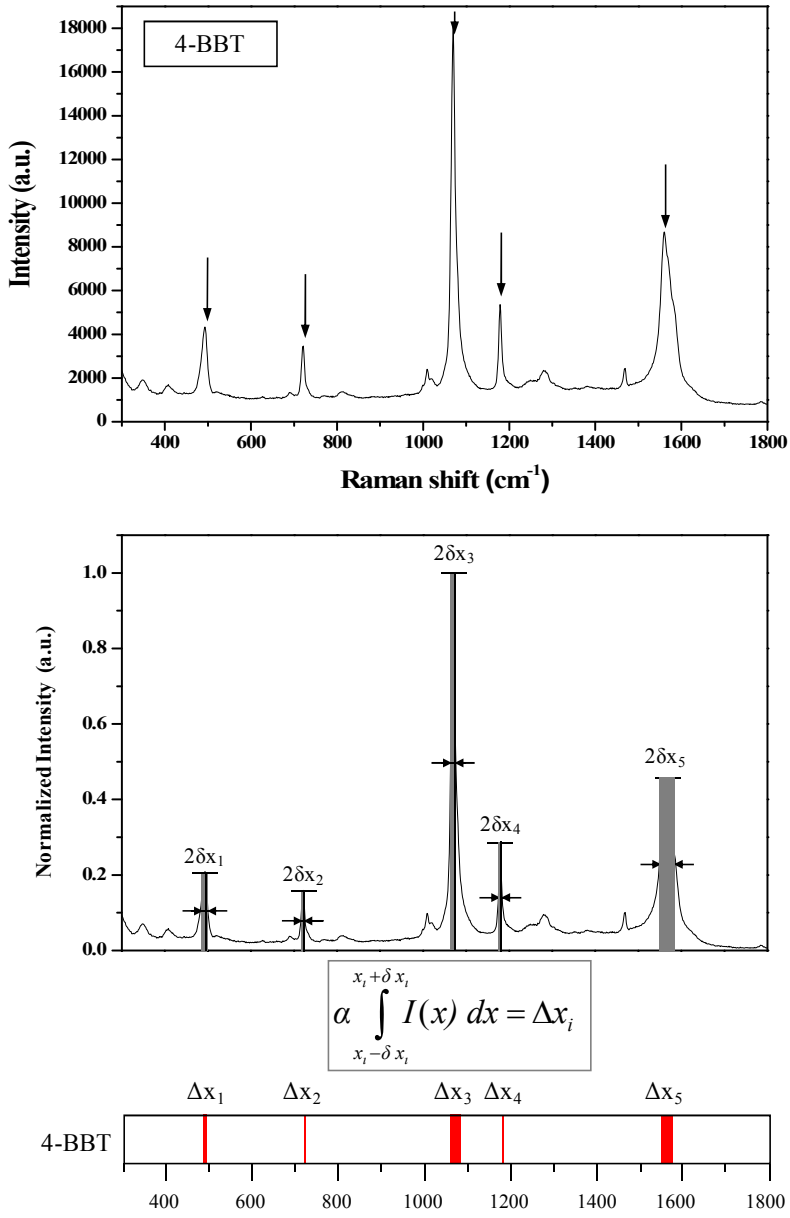

Figure 1-1. An example of barcode presentation from integration values of the Raman intensities I(x) around the Raman bands with FWHM.

2. Results and Discussion

2.1 Stretagy of SERS Dots Based Peptide Encoding

As shown in Figure 1-2a, microbeads are partitioned in separate reaction vessels, in which different amino acids are coupled using standard Fmoc chemistry.[152] Upon cleavage of the Fmoc group from the amino acid on microbeads, one type of SERS dot with its unique Raman signature is attached to the microbeads to encode each amino acid for different reactions. This process involving the coupling reaction of amino acids and their subsequent encodings with the SERS dots is repeated for the chosen number of cycles. Then, the peptide sequences generated on the microbeads can be readily identified by decoding the Raman signatures of each SERS dots. Figure 1-2b shows the scanning electron microscope (SEM) images of the microbead encoded with a large number of SERS dots (57,700 dots/bead could be loaded), indicating that long peptide seqence can be encoded. SERS dots consist of an Ag NPs-coated silica core bearing Raman chemicals and silica shell (Figure 1-2c). Figure 1-3 shows the barcode diagram of the SERS spectra based on the unique Raman peaks obtained from the different types of SERS dots. The barcode diagrams for each SERS dot are generated from the integrated intensity of peaks of full width at half maximum (Figure 1-1)[75], showing that SERS dots have their own unambiguous Raman signatures

without overlapping. In order to encode the enormous number of peptide libraries generated on microbeads, the number of SERS dots should be large enough to encode all of them. As shown in Figure 1-4a, we initially found thirty five kinds of commercially available aromatic compounds with different functional groups, such as thiol, disulfide, amine, cyano and isothiocyanate moieties, as proper Raman labels, indicating that a variety of chemicals with different functional groups can be chosen for distinct encoding. In addition, a large number of Raman encodings can be created by employing an appropriate combination of chemicals. For instance, when two kinds of Raman chemicals, such as 4-methylbenzenethiol (4-MT) and 2-naphthalenethiol (2-NT), are mixed at different molar ratios (4-MT:2-NT, 3:1, 7:1, 12:1, 19:1, 39:1), the representative peaks for each chemical can be clearly resolved in terms of their Raman shift and intensity as shown in Figure 1-5. The total number of possible encoding signature (*T*) can be described as follows:

$$T = \sum_{k=1}^{M} \frac{L!}{(L-k)!k!} P(i,k) \qquad (1)$$

where *L* is the number of available Raman labels; *M* is the number of possible incorporated Raman labels; and *i* is the number of possible intensity levels, respectively. The *P* is calculated by $P(i, k) = i^k - i + 1$. Based on this

combination strategy, more than 10,000 different types of SERS dots with their specific signatures can be generated, indicating that a large number of peptide libraries could be uniquely encoded.

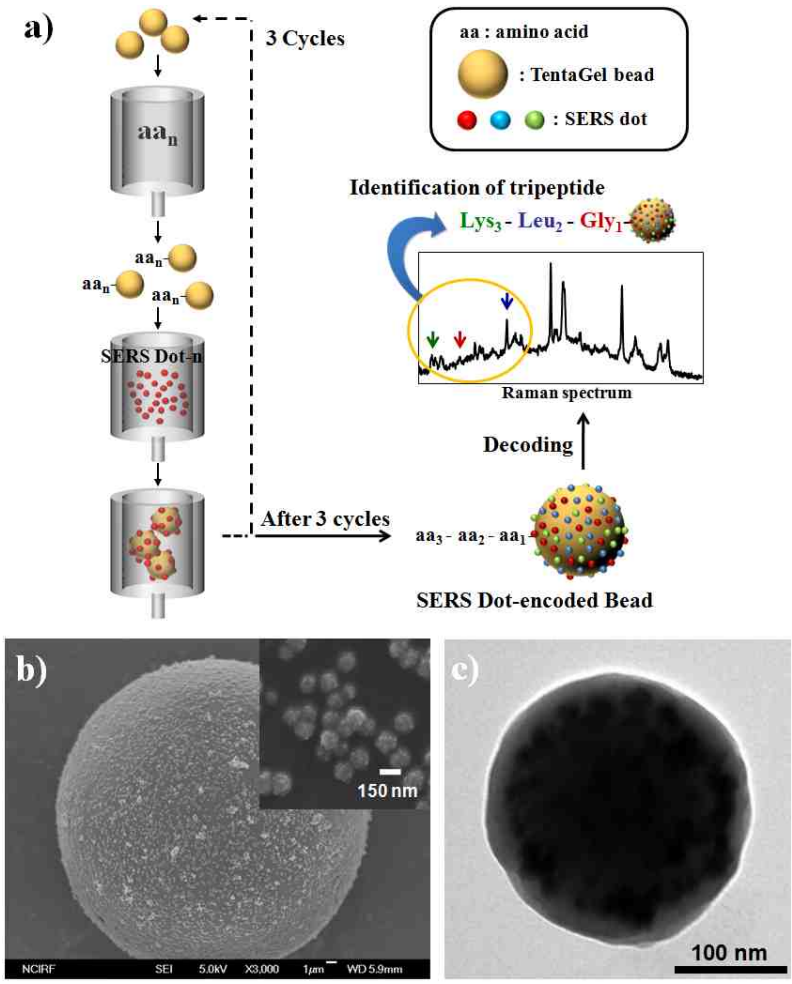

Figure 1-2. Encoding peptide libraries with SERS dots; a) Schematic illustration of SERS dot-based peptide encoding on microbeads. b) SEM image of TentaGel microbead encoded with a large number of SERS dots. Inset shows a high magnification SEM image of SERS dots attached to the microbead surface. c) TEM image of SERS dot (*ca.* 220 nm).

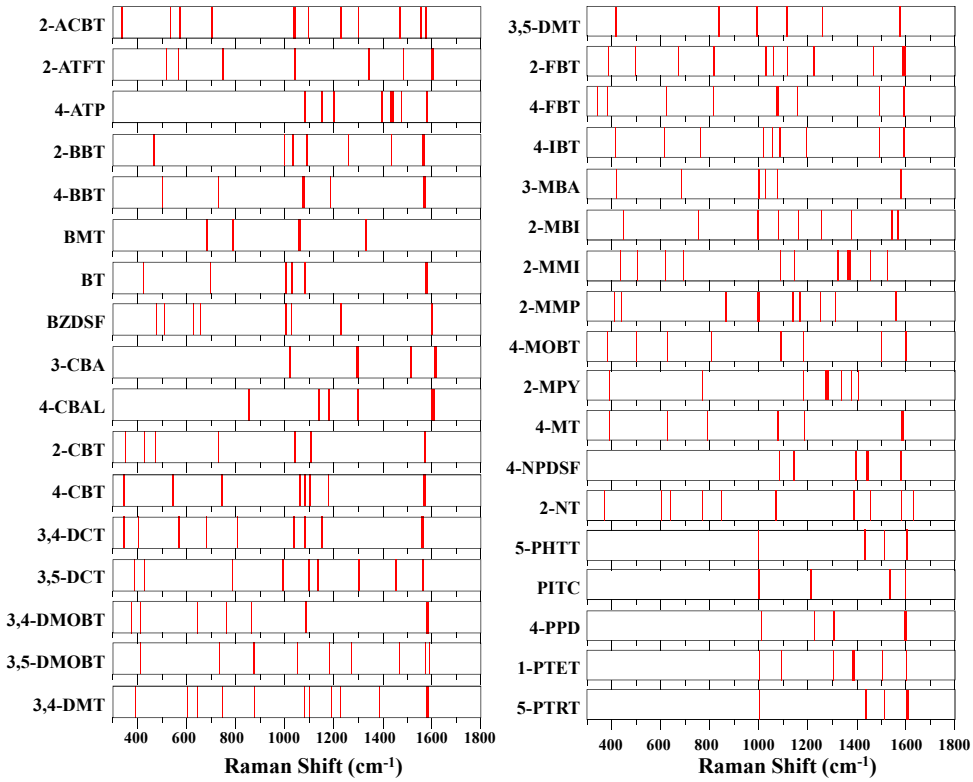

Figure 1-3. Barcode diagram of SERS spectra based on the unique Raman peaks of the different types of SERS dots.

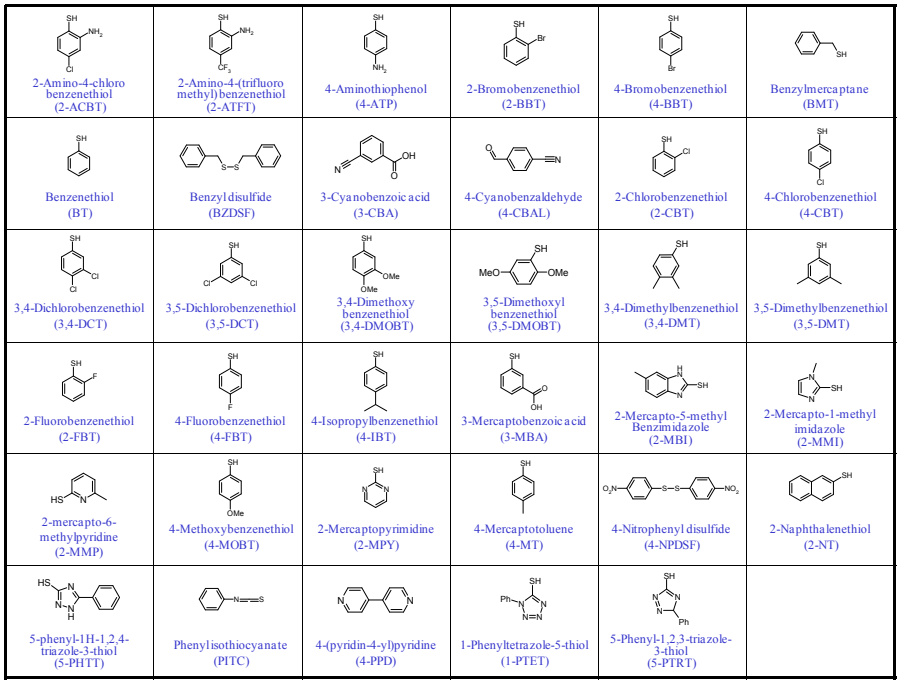

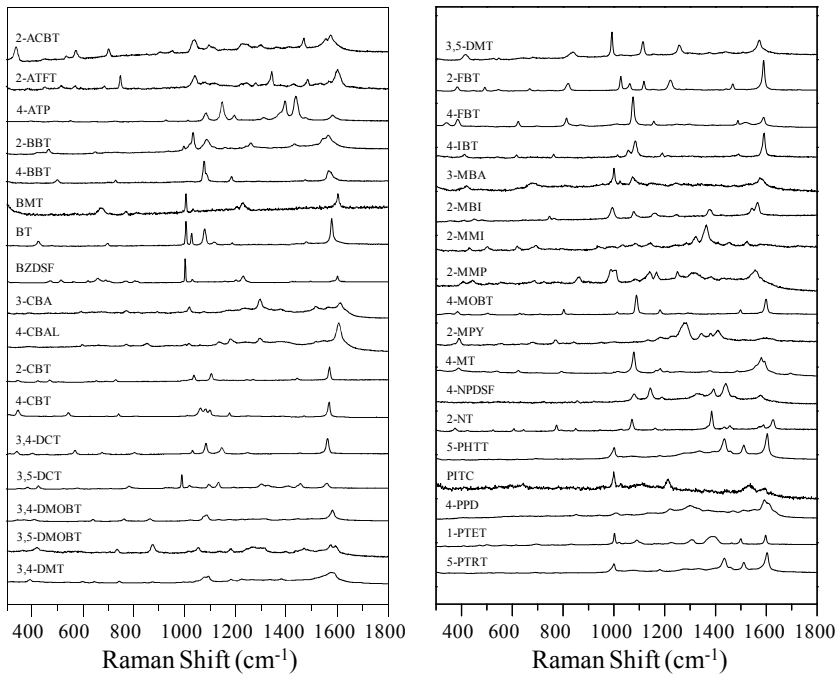

Figure 1-4. Chemical structures and SERS spectra of Raman label compounds for peptide encodings.

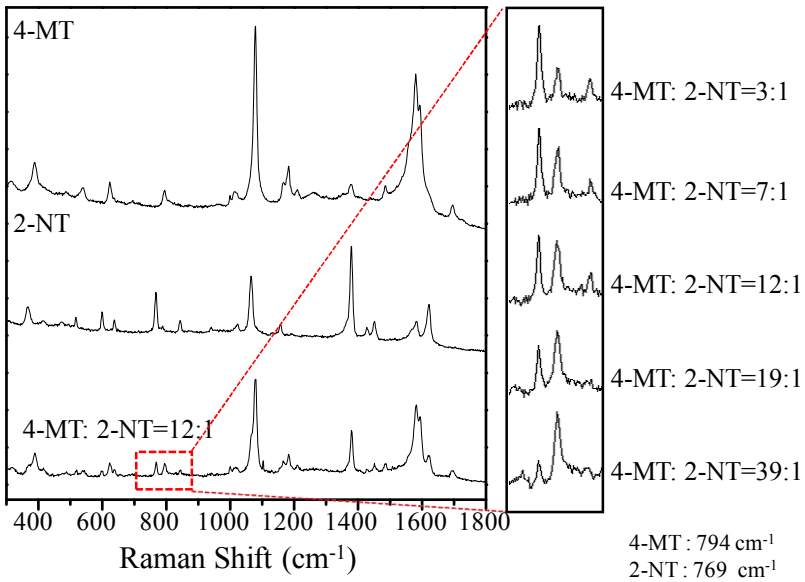

Figure 1-5. Raman spectra obtained from a combination of 4-MT and 2-NT with different molar ratios (4-MT:2-NT; 3:1, 7:1, 12:1, 19:1, and 39:1, respectively).

2.2 Stability and Mechanism Studies of SERS Dot based Encoding

In order to accurately identify the peptide libraries on microbeads, SERS dots should remain stable until the peptide synthesis is completed. Therefore, we investigated the stability of SERS dot encoding under washing, peptide coupling and Fmoc cleavage conditions. SERS dot with 4-MT RLC (SERS dot_{4MT}) was added to the suspension of H-Gly-TentaGel beads in NMP. The resulting mixture was shaken for 5 min at 25^{o}C, and then the free SERS dots were removed. As shown in Figure 1-5, the initial number of SERS dots in an area of 100 m^2 was counted from the SEM image of the SERS dot-encoded microbeads, and then compared to the values obtained after shaking the microbeads under the washing and coupling conditions for 12 h at 25 ^{o}C and in 20% piperidine solution for 1 h at 25 ^{o}C respectively. It was found that almost the same number of SERS dot_{4MT} remained adsorbed on the microbead surface (Figure 1-6a), indicating that the SERS dot-based encoding is stable. In addition, we further investigated the cross-contamination of SERS dots between the microbeads encoded with different kinds of SERS dots (SERS dot_{4MT} and SERS dot_{2NT}) during the peptide synthesis. After mixing two differently encoded beads under the coupling condition for 2 h, the encoded beads were analyzed by Raman spectroscopy. According to the results of the SERS mapping created from the representative peaks for each Raman

chemical (388 cm^{-1} for 4-MT, 767 cm^{-1} for 2-NT), both SERS dot_{4MT} and SERS dot_{2NT}-encoded beads show only their original coding (Figure 1-6b), indicating that cross-contamination did not occur between SERS dot_{4MT} and SERS dot_{2NT}-encoded beads during the peptide synthesis. Besides, these SERS mapping results demonstrate that the SERS dot encoding remains intact and distinguishable after the peptide synthesis.

In order to investigate the mechanism underlying the high stability of SERS dot encoding on microbeads, we performed additional experiment. SERS dots were added to both Fmoc-Gly-TentaGel and H-Gly-TentaGel beads, and then the beads were analyzed by SEM. As shown in Figure 1-7a, there are no SERS dots on the surface of the Fmoc-Gly-TentaGel beads, whose surface charge is neutral. However, a large number of SERS dots are attached to the surface of the H-Gly-TentaGel beads (Figure 1-7b). This indicates that the electrostatic attraction is the driving force for the initial adhesion of the negatively charged SERS dots (ζ-potential, -21.24±1.32 mV). However, this electrostatic interaction is not the only factor keeping SERS dots attached to the microbead, because, after coupling the second amino acid, Fmoc-Gly, to the amine groups on the beads, the surface charge of the microbeads becomes neutral. Based on the SEM analysis of the SERS dot-encoded beads (Figure 1-7c), we noticed that SERS dots are somethat buried inside the microbeads, suggesting that the nanoparticles bridge the polymer chains. This kind of networking with nanoparticles on microbeads might

enhance the stability of SERS dots on the surface of polymer microbead.

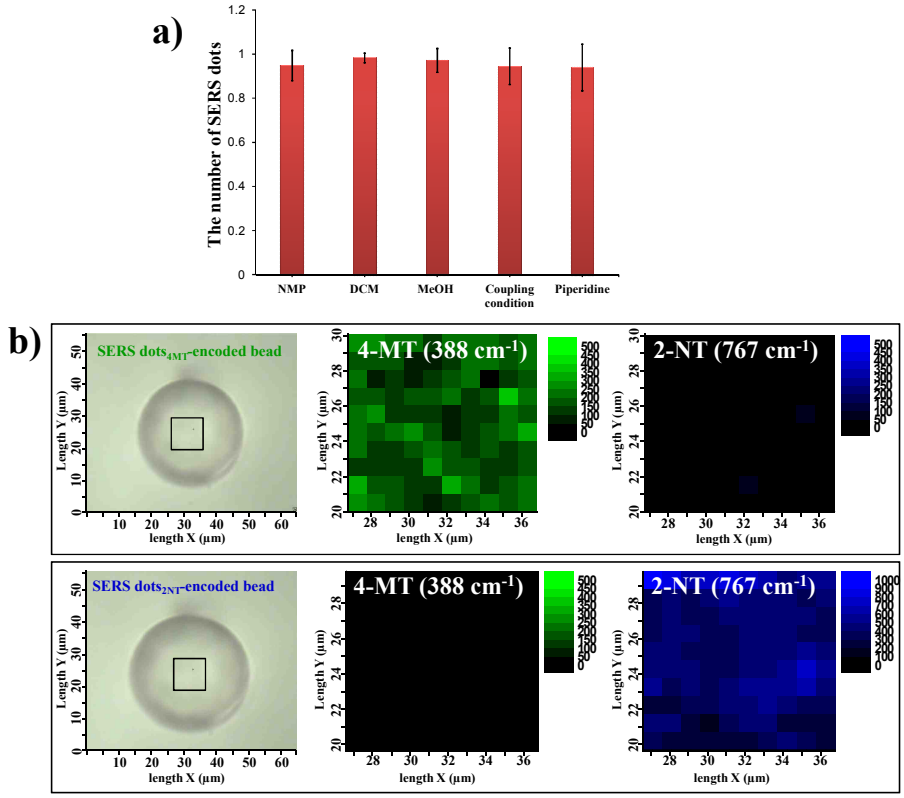

Figure 1-6. Stability of SERS dot encoding on microbeads; a) The normalized number of SERS dots on microbeads after the treatment of SERS dot-encoded beads with washing solvents, coupling reagents (BOP, HOBt and DIEA) and 20% piperidine. b) Optical pictures and SERS mapping of SERS dot_{4MT} and SERS dot_{2NT}-encoded beads.

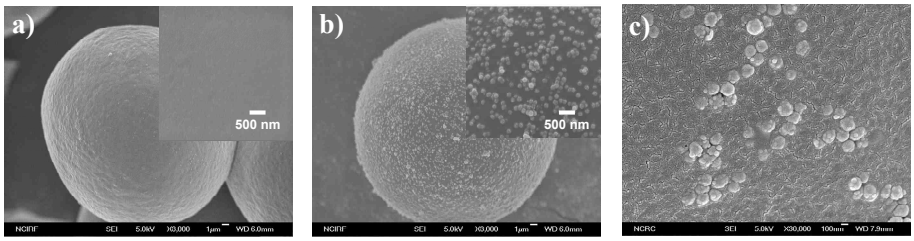

Figure 1-7. FE-SEM images of SERS dot-encoded microbeads; a) Fmoc-Gly-TentaGel beads treated with SERS dot_{4MT}. b) H-Gly-TentaGel beads treated with SERS dot_{4MT}. c) Magnified image of SERS dot adsorbed on the surface of TentaGel beads.

2.3 Identification of Tri- or Penta-peptide Encoded with SERS Dots

Finally, as a model reaction, we encoded two kinds of tripeptides with six different types of SERS dots containing 4- fluorobenzenethiol (4-FBT), benzenethiol (BT), 4-chlorobenzenethiol (4-CBT), 4-bromobenzenethiol (4-BBT), 4-aminothiophenol (4-ATP) or 2-NT as Raman label compounds. The first sequence is Lys-Leu-Gly, encoded with SERS dot_{4FBT}, SERS dot_{BT} and SERS dot_{2NT}, respectively. The second one is Asp-Ile-Asp, encoded with SERS dot_{4CBT}, SERS dot_{4BBT} and SERS dot_{4ATP}, respectively. (Figure 1-8) As shown in Figure 1-9b, each sequence is rapidly identified via decoding of representative Raman signature obtained from SERS dots at low magnification using short laser exposure time (1 sec). The Raman signatures for 4-FBT, BT and 2-NT are identified on the beads containing the Lys-Leu-Gly sequence. Moreover, the unique peaks for 4-CBT, 4-BBT and 4-ATP are observed on the Asp-Ile-Asp sequence, indicating that the SERS dot-based peptide encoding is successful and readily readable. Each peptide sequence is more obviously read out from the high-resolved scanning of a single bead (Figures 1-9c, and d). In addition, penta-peptide (Asp-Ile-Lys-Leu-Asp) is also successfully encoded by SERS dots SERS dot_{4CBT}, SERS dot_{4BBT}, SERS dot_{4FBT}, SERS dot_{BT} and SERS dot_{4ATP}, respectively (Figure 1-10). Mass spectroscopic analysis of the tripeptides after cleavage from the beads shows

good quality peptides, indicating that SERS dot encoding does not interfere with peptide synthesis (Figure 1-11).

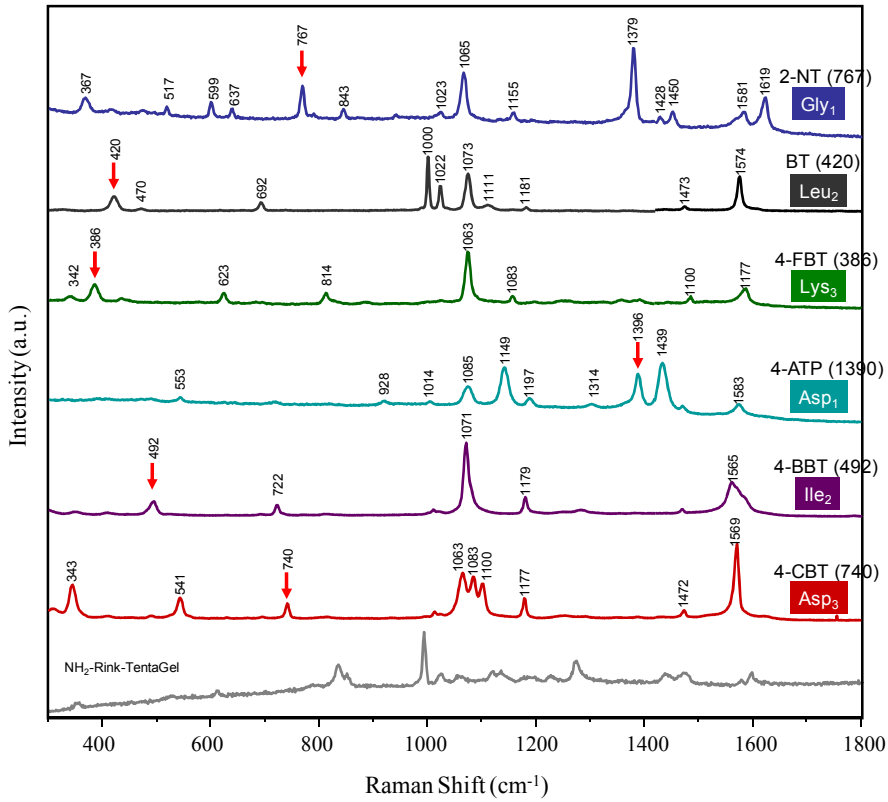

Figure 1-8. Raman spectra of six types of SERS dots and Rink-TentaGel bead (background). The representative Raman peaks (red arrows) of the SERS dots could be selected without overlapping from others.

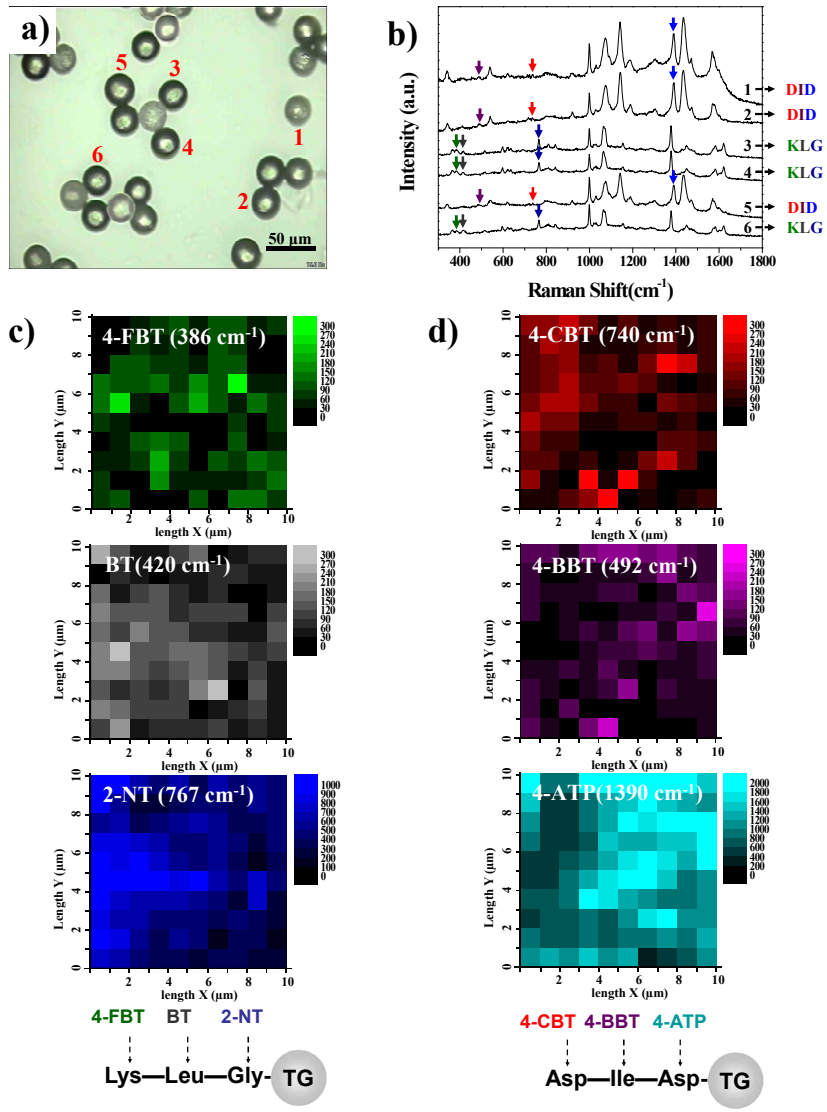

Figure 1-9. Tripeptide encoding with SERS dots; a) Optical picture of SERS dot-encoded beads having two kinds of tripeptide sequences. b) Tripeptide identification on each microbead based on Raman spectra from different types of SERS dots obtained at low magnification (numbers correspond to each of the microbeads in a). c) SERS mappings of Lys-Leu-Gly-TentaGel bead encoded with SERS dot_{4FBT}, SERS dot_{BT} and SERS dot_{2NT}. d) SERS mappings of Asp-Ile-Asp-TentaGel bead encoded with SERS dot_{4CBT}, SERS dot_{4BBT} and SERS dot_{4ATP}.

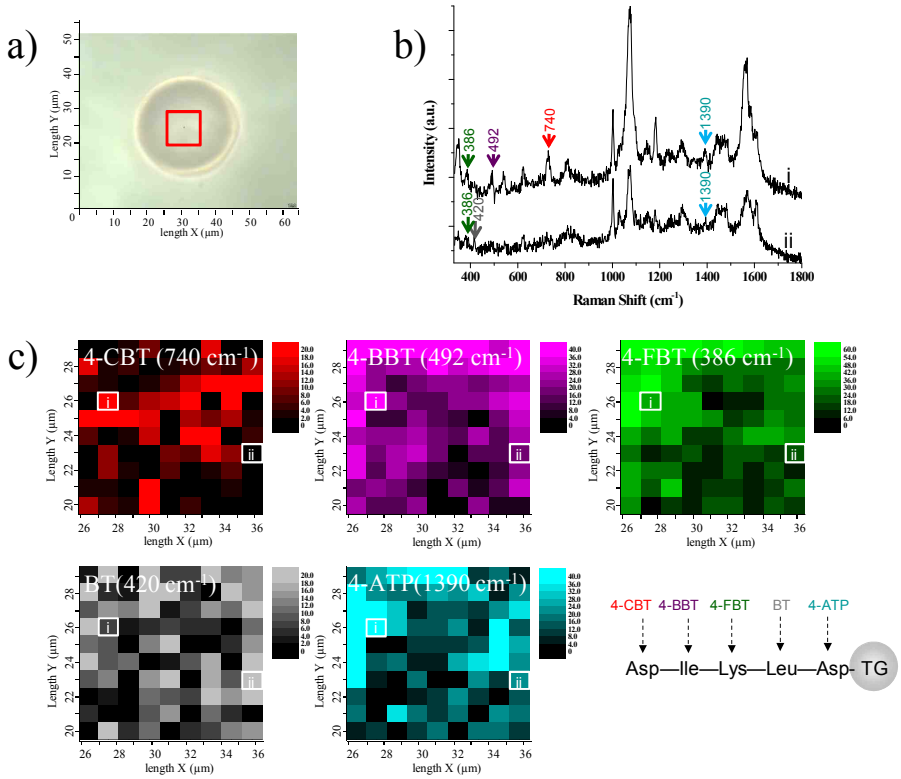

Figure. 1-10 Penta-peptide encoding with SERS dots; a) Optical image of SERS dot-encoded bead having penta-peptide sequence. b) Raman spectra of Asp-Ile-Lys-Leu-Asp-TentaGel bead encoded with different types of SERS dots from SERS mappings (point i and ii), showing the specific peaks for each Raman label (4-FBT, 386 cm^{-1}; BT, 420 cm^{-1}; 4-BBT, 492 cm^{-1}; 4-CBT, 740 cm^{-1}; 4-ATP, 1390 cm^{-1}). c) SERS mapping of penta-peptide (Asp-Ile-Lys-Lue-Asp) generated from SERS $dot_{4\text{-CBT}}$ for first Asp, SERS $dot_{4\text{-BBT}}$ for Ile, SERS $dot_{4\text{-FBT}}$ for Lys, SERS dot_{BT} for Leu and SERS $dot_{4\text{-ATP}}$ for second Asp.

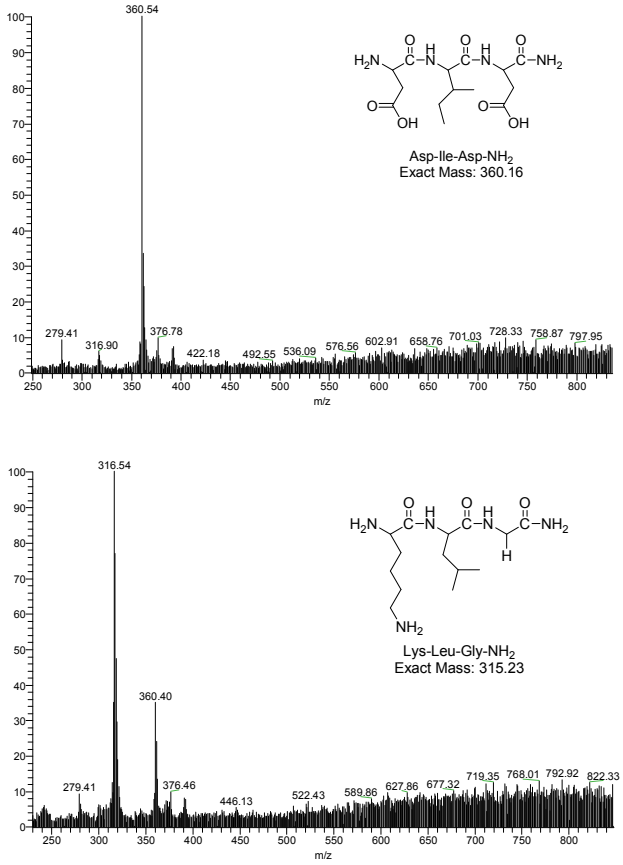

Figure 1-11. ESI-MS spectra of Asp-Ile-Asp-NH_2 and Lys-Leu-Gly-HN_2.

3. Conclusion

We demonstrate more simple and efficient optical encoding system, which involves encoding by highly sensitive SERS active nanopaticles (so called SERS dots). SERS dot encoding was found to be very stable and readily readable. The strong point of this SERS nano-encoding method is that a large number of simple aromatic molecules which have thio, isothiocyanato, azido, amino or cyano group can be utilized as Raman label compounds. This new encoding method is successfully applied to tri- and penta-peptide encoding.

Chapter 2 Near-IR SERS Nanoprobes with Au/Ag Hollow-Shell Assemblies for *In Vivo* Multiplex Detection

1. Experimental Section

1.1 Chemicals and Materials

Tetraethylorthosilicate (TEOS), 3-mercaptopropyl trimethoxysilane (MPTS), ethylene glycol (EG), poly(vinyl pyrrolidone) (PVP, M_W ~40,000), silver nitrate ($AgNO_3$, 99.99+%), octylamine (OA), tetrachloroaurate trihydrate ($HAuCl_4 \cdot 3H_2O$, 99.9+%), 4-aminothiophenol (4-ATP), 4-fluorothiophenol (4-FBT), 4-bromobenzenethiol (4-BBT), and 3,3'-diethylthiatricarbocyanine iodide (DTTC) were purchased from Sigma-Aldrich (St. Louis, MO, USA) and used without further purification. Absolute ethanol (99.8%) was purchased from Carlo Erba (Milano, Italy). 4-Chlorobenzenthiol (4-CBT) was purchased from TCI (Tokyo, Japan). Ammonium hydroxide (NH_4OH, 27%), sodium chloride, and ethanol (98%) were purchased from Daejung (Busan, Korea). Gold colloid (80 nm) was purchased from BBInternational (Cardiff, U K). Deionized (DI) water was used for all experiments.

1.2 Preparation of Ag Nanoparticles-assembled Silica Nanosphere (Ag-NPA)

TEOS (1.6 ml) was dissolved in 43 ml of absolute ethanol containing ammonium hydroxide (7.5 *v/v* %), and vigorously stirred for 20 h at 25 ^{o}C. The resulting silica nanospheres were centrifuged at 8000 rpm for 15 min, and washed with ethanol several times to remove excess reagents. These silica nanospheres were then functionalized with a thiol group. The silica nanospheres (300 mg) were dispersed in 6 ml ethanol containing 300 μl of MPTS and 60 μl of ammonium hydroxide. After the mixture was stirred for 12 h at 25^{o}C, the MPTS-treated silica nanospheres were centrifuged and washed with ethanol several times. A 100 mg aliquot of MPTS-treated silica nanospheres were thoroughly dispersed in 100 ml of $AgNO_3$ solution (3.5 mM in ethylene glycol). An 82.7 μl aliquot of octylamine was then rapidly added into the dispersed MPTS-treated silica nanospheres. The resulting dispersion was stirred for 1 h at 25^{o}C. Then, the resulting Ag-NPAs were centrifuged and washed with ethanol several times. Finally, the washed Ag-NPAs were dispersed in ethanol (10 mg/ml) for further investigation.

1.3 Fabrication of Au/Ag Hollow-shell Assembled Silica Nanospheres (Au/Ag HSA)

A 100 μL aliquot of Ag-NPA (10 mg/ml) was dispersed in 5 ml of PVP (8 wt %, MW 40,000) aqueous solution. A 0.1 mM of $HAuCl_4$ solution was loaded into a disposable plastic syringe (20 ml) with PVC tubing, and was placed on a syringe pump. Portion volumes of 0.1 mM $HAuCl_4$ aqueous solution (0.5, 1.0, 1.5, 2.0, 2.5, and 3.0 ml, respectively) were added to the Ag-NPA dispersion at a rate of 0.75 ml/min using the syringe pump. After adding the $HAuCl_4$ solution, the resulting dispersion was allowed to stabilize the Au/Ag HS assemblies for 10 min and then cooled to room temperature with vigorous magnetic stirring. The resulting mixture was washed with a saturated solution of NaCl to remove residual AgCl. Then, the resulting dispersion was centrifuged and washed with DI water (×3) and ethanol (×3).

1.4 Silica Coating of Au/Ag HSA

A 1 ml of Raman label compound (RLC) (2 mM in ethanol) was added to 1 mg of Au/Ag HSA. The resulting dispersion was shaken for 1 h at 25^{o}C. The Au/Ag $HSA_{[RLC]}$, bearing a self-assembled monolayer of RLC, were transferred to 50 mL of 2-propanol with 1 mg of PVP (MW 40,000). A 2 ml of ammonium hydroxide was added to the reaction mixture under vigorous stirring, followed by the addition of 250 μL of TEOS solution (TEOS/2-propanol, 0.8 *v/v* %) in four separate portions with a time interval of 30 min. After adding the TEOS, the mixture was allowed to react for 12 h. Then, the resulting mixture was centrifuged at 7000 rpm for 15 min and re-dispersed in ethanol (×5).

1.5 Micro-Raman Instrument

Raman measurements were performed using a confocal microscope Raman system (LabRam 300, JY-Horiba, Edison, NJ, USA) equipped with an optical microscope (Olympus, Tokyo, Japan).The Raman scattering signals were collected in a back-scattering geometry and detected by a spectrometer equipped with a thermo-electrically cooled (−70 ^{o}C) CCD detector. The excitation laser was focused and the Raman signals were collected by the same open-field ×5 or ×100 microscope lens (NA 0.90, Olympus). The excitation source was a 785 nm diode laser with 53 mW or 2.5 mW output power at a sample point for ×5 and ×100 objective lenses, respectively.

1.6 Single-particle SERS Measurement

SERS intensity of a single NIR SERS $dot_{[4FBT]}$ (Au/Ag $HSA_{[4FBT]}$ with a silica shell) was measured to evaluate SERS activity in the NIR window. The SERS signal of a single Au NP labeled with 4-FBT was also measured for comparison. Au NPs were treated with 4-fluorobenzenethiol (2 mM in ethanol) for 1 h at 25°C. Then, 1 mg of PVP (MW ~40,000) was added to the gold NP dispersion. The resulting mixture was shaken for 12 h. The Au NPs were washed three times with ethanol. A patterned slide glass was sonicated in acetone for 20 min and dried by N_2-blowing to eliminate dust on a slide glass and dried. Then, the diluted NP dispersion (0.1 mg/ml in ethanol) was dropped on the patterned slide glass. SERS of the prepared sample was measured by point-by-point mapping with a 0.5 μm step size. All mapping experiments were carried out using a ×100 objective lens (NA 0.90) with a 2 sec acquisition time. Raman spectra were obtained in a range between 750 and 1250 cm^{-1} using a 785 nm laser. After the Raman measurement, the same area of Raman mapping was observed using field emission-scanning electron microscopy (JSM-6701F, JEOL, Tokyo, Japan) to ensure that only single particles were used for quantification.

1.7 Calculation of the SERS Enhancement Factor

SERS enhancement factors (EF) for the NIR SERS dots$_{[4FBT]}$ were estimated using the following equation:

$$EF = (I_{SERS} \times N_{normal})/(I_{normal} \times N_{SERS}),$$

where I_{SERS} and I_{normal} are the intensity of the bands from SERS and normal Raman scattering, respectively, and N_{normal} and N_{SERS} are the number of 4-FBT molecules in pure form and self-assembled on the Au/Ag HSA. The peak at 1075 cm^{-1} (for 4-FBT) was used to estimate the EF. Raman signal intensity was measured for both single particles and neat 4-FBT using identical laser power for the EF calculation. Probing volume (18.8 μm^3) was approximated as a cylinder form with a diameter of 2 μm and a height of 6 μm for the normal Raman measurements. N_{SERS} was calculated by geometrically estimating the particle's surface area and a molecular footprint of 4-FBT (0.383 nm^2/molecule)[153], assuming that the thiolate molecules formed a complete monolayer. 4-FBT molecules did not produce any absorption bands that overlapped with the excitation laser wavelength, eliminating the resonance Raman effect.

1.8 Theoretical Calculation of Electric Field Enhancement

Finite element method (FEM, COMSOL ver 3.4a Multiphysics software) was used to model Au/Ag HSA suspended in water and to achieve a solution to the Helmholtz wave equation: $\nabla \times (\mu_r^{-1} \nabla \times E) - k_0^2 (\varepsilon_r - j\sigma\omega\varepsilon_0) E = 0$. The calculating mesh structure of Au/Ag HSA was constructed using hybrid mesh generation. The relative permeability of gold and silver were assumed to be $\varepsilon_r = 1$ and the complex permittivity of gold ε_r and silver ε_r were assumed to be a function of wavelength[154]. The model dimension of Au/Ag HSA (silica backbone diameter = 120 nm, Au/Ag HS diameter = 18 nm, Au/Ag HS thickness = 6 nm, and averaged distance between Au/Ag HS surface to Au/Ag HS surface = 8 nm) was based on the TEM analysis as shown in Figure 2. We assumed that Au/Ag HS was composed of uniformed Au/Ag alloy. The Au/Ag HSA was estimated by a composition-weighted linear combination of the dielectric functions of the metals[155]. The Au/Ag atomic molar composition ($Au_{\chi}/Ag_{1-\chi}$) on Au/Ag HSA was $Au_{0.07}/Ag_{0.93}$ based on the EDX analysis, and relative permittivity was achieved using the following relationship: $\varepsilon_{Au/Ag} = (\varepsilon_{Au} + 13 \cdot \varepsilon_{Ag})/14$. The polarization vector is typically taken in the parallel direction to the structure of Au/Ag HSA, whereas the direction of the k-vector is taken to be perpendicular to the plane of the structure. A perfectly matched layer and an integration layer, modeled by concentric space, were

used to reach perfect absorption at the outer boundary and minimize spurious reflections. The target structure was excited at λ = 785 nm. The adaptive mesh was refined until the maximum electric field converged. We used the FEM primarily because of its ability to produce adaptive mesh, and because it is advantageous over the finite difference time domain (FDTD) method for the complex geometry[156].

1.9 Penetration Depth Profiling

The tissue transparency of NIR SERS dots was investigated using animal tissues. A 10 μL aliquot of NIR SERS dots$_{[4CBT]}$ (0.72 nM in DI water) was injected into porcine tissue at different injection depths (1, 3, 5, 7, 8 and 9 mm) using a 26-gauge needle. The SERS spectra from each injection depth were obtained by changing the focal point from the surface to 10 mm into the tissue at intervals of 1 mm focal depth using the confocal microscope Raman system. All depth profiling was carried out with a 785 nm excitation laser, 53 mW laser power, open-field ×5 microscope lens and 10 s acquisition time. The SERS intensities at each injection depth were averaged from the three strongest SERS spectra. The two 4-CBT peaks (342 and 541 cm^{-1}) were used to evaluate the capability of NIR SERS dots signal penetration. The averaged SERS intensities were normalized with the intensity of the NIR SERS dot suspension (0.72 nM).

1.10 *In vivo* Multiplex Detection with NIR SERS Dots

Male nude mice were anesthetized with an intraperitoneal injection of ketamine and xylazine mixture solution. The NIR SERS dot$_{[4CBT],}$ NIR SERS dot $_{[4FBT],}$ and NIR SERS dot $_{[4BBT]}$ dispersions (in PBS, pH 7.0) were injected subcutaneously into three locations on the gluteal region of the mouse, respectively. The suprascapular area of the mouse was chosen to be subcutaneously inject a mixture of NIR SERS dots$_{[4CBT],}$ NIR SERS dots$_{[4FBT],}$ and NIR SERS dots$_{[4BBT]}$. SERS spectra were obtained from each injection depth (*ca.* 3 mm) using a micro Raman system with a 785 nm excitation laser.

2. Results and Discussion

2.1. Synthesis of Plasmonic Au/Ag Hollow-Shell Assemblies

Au/Ag HS nanostructures exhibit tunable extinction bands from visible to NIR regions (*ca*. 400–1200 nm),[12,130-132] indicating that they can be good candidates as SERS-sensitive substrates in the NIR optical window.[15,42] The galvanic replacement reaction, which is well-established method for preparing metallic HS, has ability to finely tune the extinction bands of the Au/Ag HS.[132,133] Plasmonic Au/Ag HSs were fabricated on the surface of silica nanospheres *via* galvanic replacement reaction of Ag NPs that were pre-assembled on silica to prepare the NIR SERS dots (Figure 2-1). After synthesizing the silica nanospheres (*ca.* 125 nm in diameter) using the Stöber method,[26] they were functionalized with thiol groups to directly grow Ag NPs on their surface using the amine reduction method,[66] as shown in Figure 2-1a. The aliphatic amine (octylamine) was used as both a reducing agent and a stabilizer during this process to grow Ag NPs on the silica surfaces under mild conditions. As shown in Figure 2-1c, Ag NPs were densely introduced onto the surface of thiol-functionalized silica nanospheres. The number of Ag NPs formed on a single silica nanosphere was 66 ± 12 (counted from 10 silica nanospheres, based on their transmission electron microscopic [TEM] images), and their average size

was 18.3 ± 3.7 nm (counted from 115 Ag NPs, based on their TEM images) (Figure 2-1d).

Then, a $HAuCl_4$ aqueous solution (0.1 mM) was added, using a syringe pump, into a 5 mL dispersion of Ag NPs-assembled silica nanospheres (Ag-NPAs, 0.2 mg/ml) containing poly-*N*-vinyl-2-pyrrolidone (PVP, MW ~40000, 400 mg) (Figure 2-2a). The amount of $HAuCl_4$ solution added to the Ag-NPAs was varied from 0.5 to 3.0 ml. Figures 2-2b–e show the high resolution-transmission electron microscopy (HR-TEM) images of plasmonic Au/Ag HSAs. A small pinhole (< *ca.* 3 nm) was created on the Ag NPs as 1 ml of $HAuCl_4$ solution was added, while the oxidation of Ag NPs proceeded by Au^{3+} ions at their weakest point (Figure 2-2c). Then, after adding 1.5 ml of $HAuCl_4$ solution, the size of pinholes increased to about 5 nm, and the Au/Ag hollow nanostructure matured (Figure 2-2d). In addition, the Au atomic fraction, which was estimated by energy dispersive X-ray spectroscopy (EDX), increased with the added amount of $HAuCl_4$ solution (Figure 2-3a), indicating that an Au/Ag alloy structure had been created on the silica nanospheres. Finally, hollow interiors of 11-nm size in average were formed in the Au/Ag HS on the silica nanospheres as 3.0 ml of $HAuCl_4$ solution was added (Figure 2-2e). The Au/Ag hollow nanostructures began to change to Au nanosphere structures when more than 3.0 ml of $HAuCl_4$ solution were added, which eventually came off from the silica surface. (Figure 2-3). The structure of the Au/Ag HS on the silica nanospheres was

confirmed by atomic profile analysis using scanning transmission electron microscope (STEM) equipped with an EDX (Figure 2-2g). According to the atomic line profile analysis results, the intensity of both Au and Ag atoms was higher at the exterior of the nanosphere than that in the interior, further indicating that it had a hollow-shell structure of Au and Ag alloy. The Au/Ag atomic molar composition in Au/Ag HSA has gradually changed to $Au_{0.3}/Ag_{0.7}$ (Figure 2-4a). This Au/Ag molar composition was consistent with previously reported results for the galvanic replacement reaction.[157]

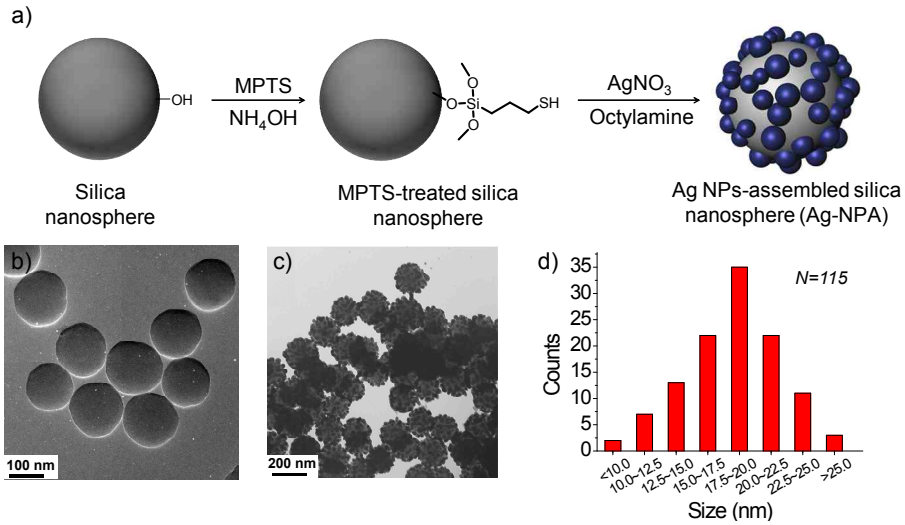

Figure 2-1. Preparation of Ag nanoparticles-assembled silica nanospheres (Ag-NPAs). a) Schematic diagram for Ag-NPAs using the modified ployol method. b) Transmission electron microscopic (TEM) images of MPTS-treated silica and c) Ag-NPA. d) Size distributions of Ag NPs on the surface of MPTS-treated silica.

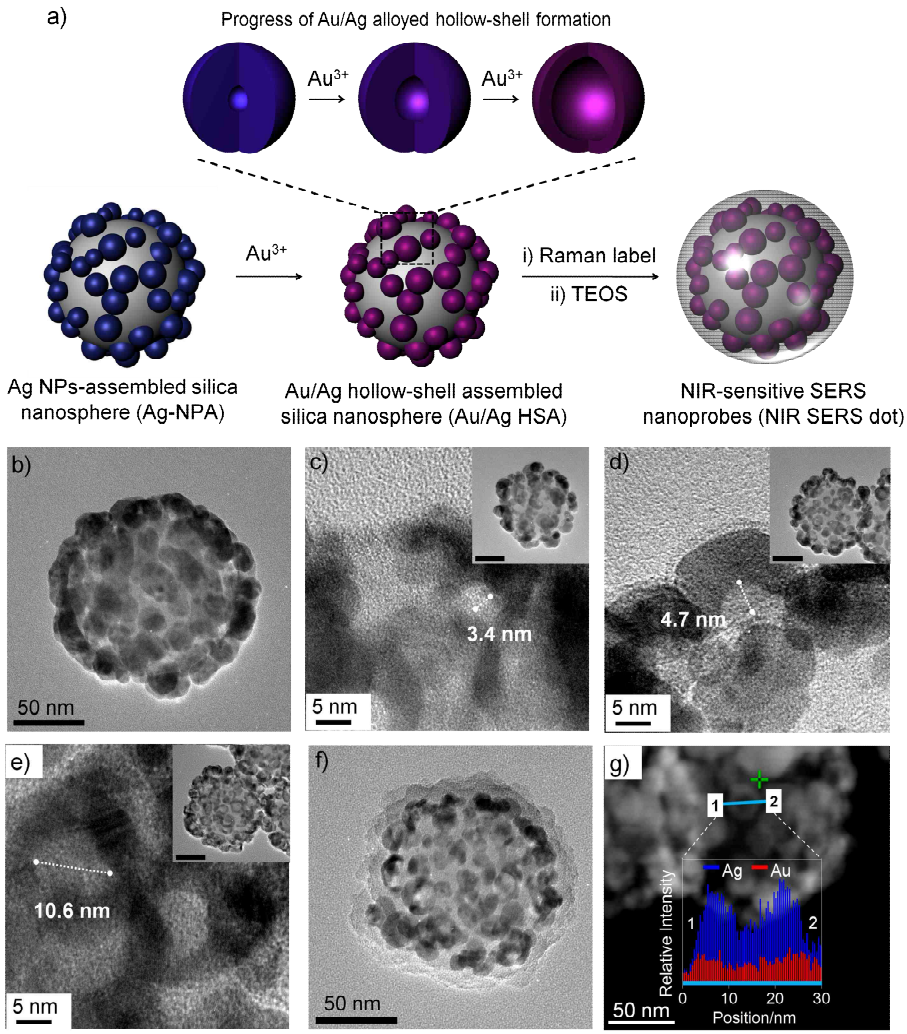

Figure 2-2. Preparation of Au/Ag hollow-shell (HS) assembly-based near-IR SERS nanoprobes (NIR SERS dots). a) Schematic diagram of fabricating the Au/Ag hollow shell (HS) assembly-based NIR SERS dots by the galvanic replacement reaction followed by silica encapsulation. Transmission electron microscopic (TEM) images of b) Ag NPs-assembled silica nanosphere (Ag-NPA), and Au/Ag HSs on the silica surface after adding c) 1.0 ml, d) 1.5 ml, and e) 3.0 ml of 0.1 mM-$HAuCl_4$, respectively. The hollow interior is represented by a white dotted line in (c – e). The insets are lower magnified TEM images of the Au/Ag HSs assembled silica nanosphere (Au/Ag HSA) (scale bar, 50 nm). f) TEM image of NIR SERS dots (silica shell-coated

Au/Ag HSA). g) High angle annular dark field-scanning transmission electron microscopy (HAADF-STEM) image of Au/Ag HSA for Ag and Au atomic profiling of single Au/Ag HS for the sample in (d). The cyan line indicates the atomic profiling region of Au/Ag HSA.

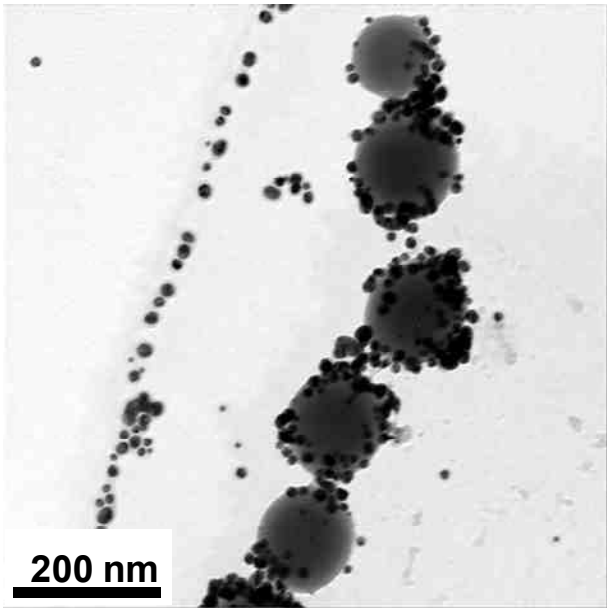

Figure 2-3. TEM image showing Au NPs on silica nanospheres and off the silica nanospheres after the addition of 20 ml of $HAuCl_4$ solution (0.1 mM).

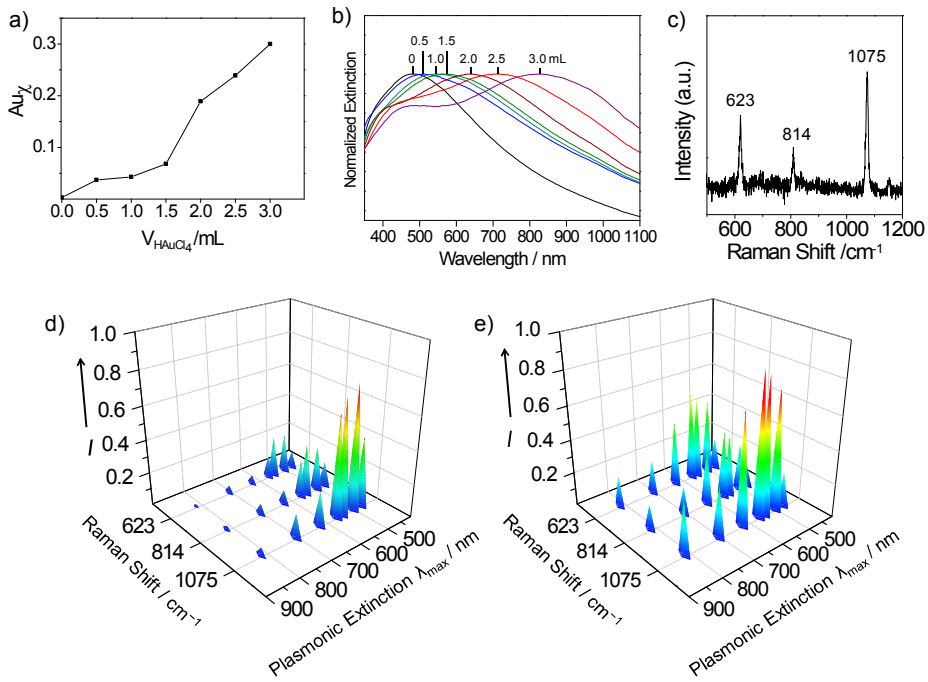

Figure 2-4. Analysis of Au atomic fraction (Au_χ), plasmonic extinction, and the SERS effect for Au/Ag HSA as a function of different volume of $HAuCl_4$ solution (0.1 mM): 0, 0.5, 1.0, 1.5, 2.0, 2.5, and 3.0 ml, respectively. a) Au atomic fraction and b) the plasmonic extinction spectra of various Au/Ag HSAs with various volumes of $HAuCl_4$ solution. c) Typical SERS spectrum of 4-fluorobenzenthol (4-FBT) adsorbed on Au/Ag HSAs. Normalized SERS intensities of 4-FBT adsorbed on various Au/Ag HSAs at 623, 814 and 1075 cm^{-1} by photo-excitation of d) visible light (532 nm wavelength and 2.3 mW laser power) and e) near-infrared (NIR) light (785 nm wavelength and 13 mW laser power). The laser beam diameter at the sample is 2 μm and 3 μm at the sample using ×10 objective lens for 532 nm and 785 nm excitations, respectively, and signal acquisition time was 30 s for all measurements.

2.2. Optical Properties of Plasmonic Au/Ag Hollow-Shell Assemblies

We investigated the extinction bands of the plasmonic Au/Ag HSA and their SERS effects. The plasmonic extinction of Au/Ag HSA was red-shifted toward the NIR region accompanied by broadening of the extinction band as the adding amount of $HAuCl_4$ was increased (Figure 2-4b). This plasmonic red-shift indicates that the surface plasmon of Au/Ag HSA can be tuned to the NIR window by simply adding the appropriate amount of $HAuCl_4$. The broadening of the plasmonic extinction band can be interpreted by size-heterogeneity of Au/Ag hollow-shells and random plasmonic coupling between hollow-shells of various sizes. In order to find the most active SERS nanoparticles in the NIR window, 4-fluorobenzenethiol (4-FBT) as a labeling compound was adsorbed on the surface of the Au/Ag HSA (this probe is denoted as Au/Ag $HSA_{[4FBT]}$). Each Au/Ag HSA has the unique optical property characterized by extinction maximum λ_{max} ranging from 480 to 825 nm depending on the amount of $HAuCl_4$ (Figure 2-4b). Then, the SERS spectra of Au/Ag $HSA_{[4FBT]}$ were obtained by photo-excitation of two different laser-lights: One is 532 nm in the visible range and the other is 785 nm in the NIR range. Figures 2-4d and 2-4e show the SERS intensities of Au/Ag $HSA_{[4FBT]}$ at 623, 814, and 1075 cm^{-1} obtained by visible photo-excitation (532 nm) and NIR photo-excitation (785 nm), respectively. The

SERS intensities of Au/Ag $HSA_{[4FBT]}$ were normalized with the Raman intensity of the 882-cm^{-1} band of ethanol in order to roughly compensate roughly for the dependency of excitation wavelength.[158] In particular, the Au/Ag HSA with a plasmon extinction of λ_{max} = 565 nm exhibited the strongest SERS intensity by NIR laser excitation, which is more than four times stronger than that of Ag-NPA (Figure 2-4e). A mismatch of the SERS excitation maximum and the plasmonic extinction maximum is commonly observed,[30] particularly in heterogeneous samples, and this phenomena has been interpreted in terms of heterogeneous nature of SERS hot spots.[158,159] Taken together, these results show that Au/Ag HSA is a good candidate as a NIR-sensitive SERS nanoprobe, producing a very strong signal in the NIR window.

2.3. Evaluation of Single-particle SERS Activity

We performed the SERS measurement on a single Au/Ag HSA to further evaluate its SERS activity in the NIR window. After introducing 4-FBT onto Au/Ag HSA, the resulting particles were coated with a silica shell using the modified Stöber method (Figure 2-2f). The silica shell-coated Au/Ag $HSA_{[4FBT]}$ (NIR SERS $dot_{[4FBT]}$, 0.1 mg/ml in ethanol) solution was drop-cast on a patterned slide glass to measure the SERS signal from single Au/Ag HSA, allowing us to easily distinguish the SERS-measured particles one another using scanning electron microscopy (SEM) images. After mapping the SERS signals with a 0.5-μm step size for 2 s using a 785-nm laser line, the resulting images were then overlaid with the corresponding SEM images. As shown in Figure 2-5a, the area of intense signals in the SERS intensity map corresponded to the position of the single NIR SERS $dot_{[4FBT]}$ taken by SEM, indicating that SERS signal is strong enough for every single probe particle to be detected (dotted circle in Figure 4a). We also measured the SERS signal from a single Au NP (80 nm, λ_{max} = 548 nm)[32] to compare their signal intensities. As shown in Figure 2-5b, the SERS signal from a 4-FBT-coded single Au NP (Au $NP_{[4FBT]}$) was not detectable by NIR excitation (dotted circle in Figure 2-5b). The SERS signal was detected only when two Au NPs formed a dimer (solid circle in Figure 2-5b) generating plasmonic coupling between the Au $NPs_{[4FBT]}$. Figure 2-5c shows the SERS spectra

obtained from a single NIR SERS $dot_{[4FBT]}$ and a single Au $NP_{[4FBT]}$, respectively. These results clearly indicate that the Au/Ag HSA-based SERS nanoprobes exhibit single particle-detectable strong Raman signals in the NIR window. In order to support these experimental results, we calculated the electric field (E-field) enhancements of the Au/Ag HSA and Au NP using the finite element method (FEM) at λ = 785 nm (Figures. 2-6a and b) and compared them each other. The dimension of Au/Ag HSA was defined based on the TEM analysis shown in Figure 2-6a. The calculation revealed that the E-field enhancement was highly localized at the Au/Ag HSA surface, and the field enhancement was maximized at the edge between Au/Ag HSs. The local field enhancement in the Au/Ag HSA was about 10^2 times higher than that in the Au NP (80 nm). Considering that the light intensity is proportional to the square of optical field and, incident and scattered fields are enhanced close to the hot spots, these FEM simulations demonstrate why Au/Ag HSA is able to generate strong SERS signals even from a single particle. In addition, we calculated the SERS enhancement factor (EF) for 26 single NIR SERS $dots_{[4FBT]}$ and plotted their distribution (Figure 2-5d). The average SERS EF value was 2.8×10^5. The distribution of the SERS EF values was very narrow with high reproducibility, which was attributed to the ensemble-average effect of the numerous Au/Ag HSs. These results strongly suggest that the NIR SERS dots can be applied for more accurate and quantitative detection of target biomolecules than previously reported single-hollow

particles or NP aggregates.[28,43]

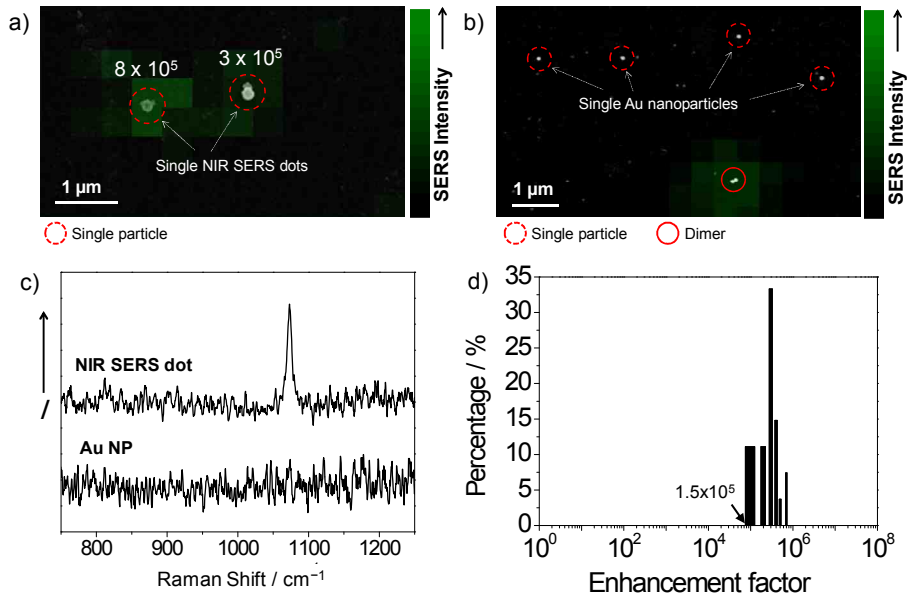

Figure 2-5. SERS measurements and signal distribution from single NIR SERS dot. a) SERS intensity map of NIR SERS dot bearing 4-FBT (NIR SERS dot$_{[4FBT]}$), showing SERS signals (with enhancement factors of 8×10^5 and 3×10^5): the SERS intensity map was overlaid with its corresponding scanning electron microscopic (SEM) image. b) SERS intensity map of single Au NPs bearing 4-FBT (Au NPs$_{[4FBT]}$, 80 nm), showing no SERS signals. The solid circle indicates two Au NPs formed a dimer. c) SERS spectra obtained from a single NIR SERS dot$_{[4FBT]}$ and a single Au NP$_{[4FBT]}$. d) Distribution of enhancement factors for the 1075 cm^{-1} Raman band of the NIR SERS dot$_{[4FBT]}$. All measurements were performed with 785 nm photo-excitation of 2.3 mW at sample and acquisition time of 2 s.

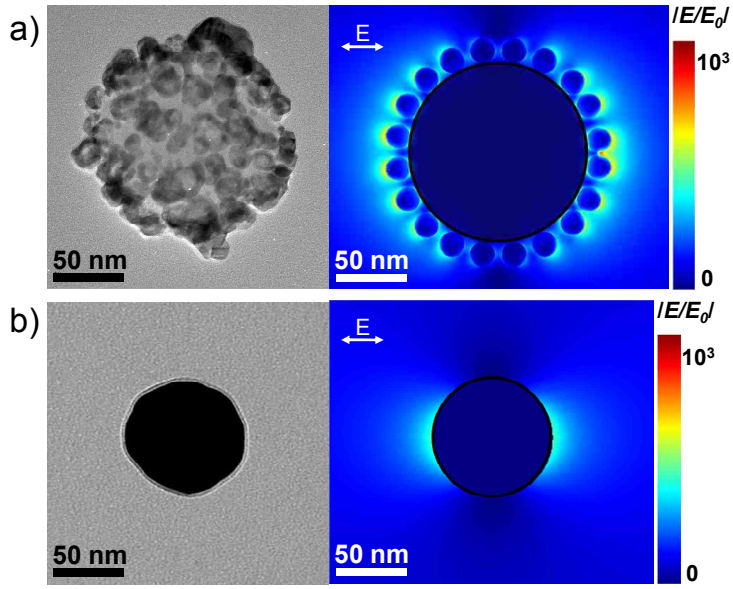

Figure 2-6. Calculated near-field electromagnetic field distribution of a single Au/Ag HSA and Au nanoparticle (NP). a) TEM images and near-field electromagnetic field distribution calculated by finite element method (FEM) for single Au/Ag HSA and b) for single Au NP.

2.4. SERS Signal Penetration Capability of NIR SERS Dots through Animal Tissue

We investigated signal penetration capability of the NIR SERS dots through animal tissues. After the Au/Ag HSA was coated with a silica shell to provide biocompatibility and for easy subsequent functionalization, a 10 μL aliquot of 4-chlorobenzenethiol (4-CBT) coded NIR SERS dots (0.72 nM) was injected into porcine tissues over different injection depths of 1–9 mm. Then, the SERS signals were measured from each depth using a micro Raman system with NIR excitation laser (Figure 2-7a). As expected and shown in Figure 2-7b, the intensity of the SERS signals decreased with injection depth. Notably, a strong SERS signal was still detectable even from an injection depth of 8 mm. These results indicate that the SERS signals generated from NIR SERS dots can be detected effectively from deep tissues for *in vivo* multiplex detection of target molecules.

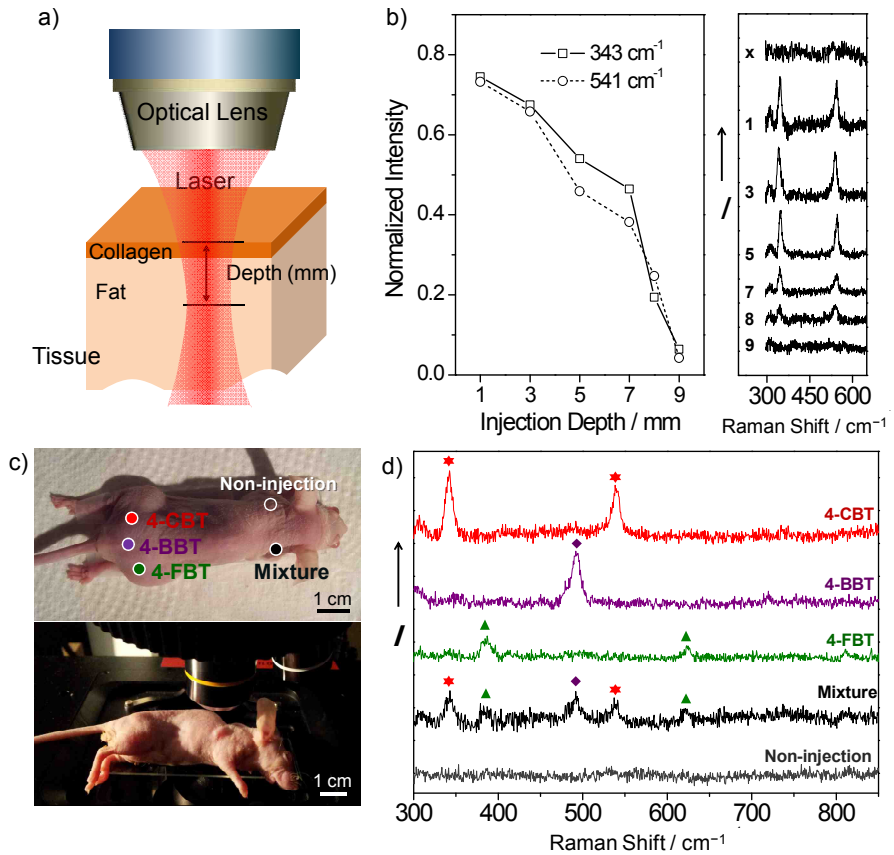

Figure 2-7. *In vivo* multiplex detection using NIR SERS dots. a) Schematic illustration of penetration-depth profiling with a 785 nm laser line. b) Normalized SERS intensity and SERS spectra of NIR SERS dots coded with 4-CBT as a function of injection depth (10 s-acquisition and 60 mW laser power). c) Photographs of a mouse in which the NIR SERS dots (4-FBT, 4-CBT, 4-BBT, and their mixture, respectively) were injected (upper) and of the micro Raman measurement for *in vivo* multiplex detection (lower). d) SERS spectra from NIR SERS dots injected inside the mouse with the 785 nm photo-excitation of 53 mW laser power and light acquisition time of 100 s.

2.5. *In Vivo* Multiplex Detection of SERS Signal with NIR SERS Dots

Finally, we applied NIR SERS dots to an *in vivo* multiplex detection in a mouse. NIR SERS dots labeled with simple aromatic compounds, such as 4-aminothiophenol (4-ATP), 4-bromobenzenethiol (4-BBT), 4-CBT and 4-FBT, were prepared for multiplex detection. Each NIR SERS dot had its own characteristic Raman signal, which was much easier to distinguish from mixed signals in a multiplex detection system, particularly when compared to SERS probes using conventional NIR-fluorescent dyes, such as 3,3'-diethylthiatricarbocyanine iodide (DTTC, λ_{max} = 765 nm), which produced complicated Raman fingerprints (Figure 2-8). Hence, many simple aromatic compounds can be used as Raman label compounds to fabricate NIR SERS dots. This is very advantageous in terms of multiplexing-capability, cost, and signal deconvolution. A 10 μL aliquot of each NIR SERS dot or their mixture (0.72 nM) was then subcutaneously injected into a nude mouse, as shown in Figure 2-7c (upper photograph), and their SERS spectra were measured using a micro Raman system with 785 nm photo-excitation (lower photograph, Figure 2-7c). As shown in Figure 2-7d, we obatained intense and simple Raman signals for 4-CBT (541 cm^{-1}), 4-BBT (492 cm^{-1}), and 4-FBT (386 cm^{-1}) through the mouse tissues from a mixture of NIR SERS dots as well as from an individual NIR SERS dot. It was also very easy to decode

the mixed signals from three different NIR SERS dots. Our NIR SERS dots are different from the NIR SERS nanoprobe system using NIR dyes, as they afford intrinsically simple Raman spectra; thus, it is more convenient to deconvolute the mixed signals and to eventually detect several targets from the same area.

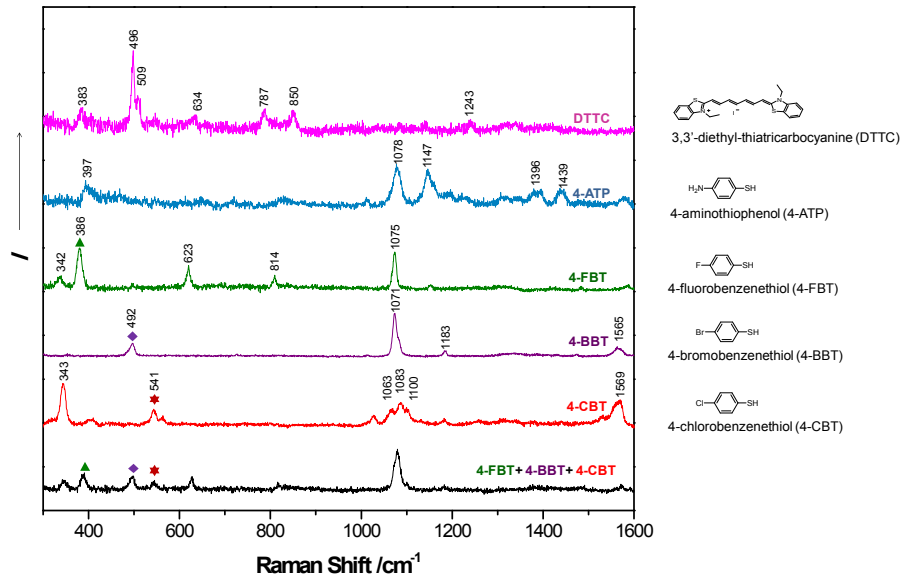

Figure 2-8. SERS spectra of NIR fluorescence dye (DTTC, absorption λ_{max} = 655 nm) and simple aromatic compounds on Au/Ag HSA and their chemical structures.

3. Conclusion

We developed NIR SERS nanoprobes based on plasmonic Au/Ag HSA, which produced intense SERS signals in the NIR optical window. A single NIR SERS dot generated strong SERS signals (average EF value 2.8×10^5) with high reproducibility. In addition, the NIR SERS dot signals were detected effectively from deep tissues of up to 8 mm depth, and they exhibited a capability for use in an *in vivo* multiplex detection system from a live animal study. The high sensitivity, reproducibility and multiplexing-capacity of NIR SERS dots enables us to detect various biological molecules at the same time from a live animal and decipher their unknown functions in a high throughput manner.

Chapter 3 Seedless Fabrication of Bumpy Silver Nanoshells for *In Vivo* Cell Tracking with Near-IR SERS

1. Experimental Section

1.1 Chemicals and Materials

Tetraethylorthosilicate (TEOS), 3-mercaptopropyl trimethoxysilane (MPTS), ethylene glycol (EG), poly(vinyl pyrrolidone) (PVP, Mw ~40,000), silver nitrate ($AgNO_3$, 99.99+%), octylamine (OA), dimethylsulfoxide, 3-(4,5-dimethylthiazol-2-yl)-2,5-diphenyltetrazolium bromide, 4-fluorothiophenol (4-FBT), 4-aminobenzenthiol (4-ABT), 4-chlorobenzenethiol (4-CBT), and 4-bromobenzenethiol (4-BBT) were purchased from Sigma-Aldrich (St. Louis, MO, USA) and used without further purification. Methoxy poly(ethylene glycol) sulfhydryl (mPEG-SH) (Mw 5,000) was purchased from Sunbio (Anyang, Korea). Ammonium hydroxide (NH_4OH, 27%) and ethanol (98%) were purchased from Daejung (Busan, Korea). Deionized (DI) water was used for all the experiments.

1.2 Preparation of Bumpy Ag Nanoshell (AgNS)

Tetraethylorthosilicate (TEOS, 1.6 mL) was dissolved in 40 mL of absolute ethanol, followed by addition of a 3 mL portion of aqueous ammonium hydroxide (27%). The resulting mixture was vigorously stirred using a magnetic bar for 20 h at 25 ^{o}C. The synthesized silica nanoparticles (NPs) were centrifuged and washed with ethanol several times to remove the excess reagents. These silica NPs were then functionalized with the thiol group. Silica NPs (300 mg) were dispersed in 6 mL of ethanol containing 300 μL of MPTS and 60 μL of aqueous ammonium hydroxide (27%). The mixture was stirred for 12 h at 25 ^{o}C. The resulting MPTS-treated silica NPs were centrifuged and washed with ethanol several times. A 5 mg portion of PVP was mixed with 25 mL of ethylene glycol, followed by the addition of various amounts of MPTS-treated silica NPs. Then, a 25 mL portion of $AgNO_3$ solution (in ethylene glycol) was added to the silica NP solution and thoroughly mixed (final concentration of $AgNO_3$ was 3.5 mM). A 41.3 μL portion of octylamine (final concentration of octylamine was 5 mM) was then rapidly added to the above solution. The resulting dispersion was stirred for 1 h at 25 ^{o}C. Afterwards, the particles were centrifuged and washed with ethanol several times for purification.

1.3 Preparation of PEGylated Bumpy AgNS

A 1 mL portion of Raman label compound (2 mM in ethanol) was added to 1 mg of AgNSs. The resulting dispersion was shaken for 1 h at 25 ^{o}C. The AgNSs, bearing adsorbed Raman label compound at their surface, were centrifuged and washed with ethanol several times. In order to improve the biocompatibility of AgNSs, their surface was grafted with PEG. A 1mL portion of mPEG-SH (2 mM in ethanol) was mixed with 1 mg of AgNSs bearing Raman labels for 1 h, followed by centrifugation several times and resuspension in DI water.

1.4 Cytotoxicity Studies of NIR-SERS probe

A549 cells (adenocarcinomic human alveolar basal epithelial cells) were maintained in F-12 medium containing 10% fetal bovine serum (FBS) and 1% penicilline/streptomycin at 37 ^{o}C and 5% CO_2. After incubation for 18 h at 37 °C, the cellular toxicity was examined using the MTT [3-(4,5-dimethylthiazol-2-yl)-2, 5-diphenyltetrazolium bromide] assay. A 20 μl MTT solution (5 mg/ml) was added to the cell containing wells, and the cells were incubated for 4 h at 37 ^{o}C. The cells were treated with 100 μl of dimethylsulfoxide and the absorbance at 540 nm was quantified using an ELISA reader (BioRad, Hercules, CA, USA).

1.5 *In Vivo* Toxicity Studies of NIR-SERS Probe

A 400 μl of NIR-SERS probes (0.5 nM) dispersed in PBS (pH 7.0) containing 3% BSA were intravenously administered to the three mice with 50 mg/kg NIR-SERS probe. The other three mice were injected with 400 μl PBS and this group was treated as a control. Mice were anesthetized via an intraperitoneal injection of ketamine (50 mg kg^{-1}) and xylazine (2.5 mg kg^{-1}). NIR-SERS Probes were then injected in the tail vein. All mice were sacrificed at the same time after 3 day from NIR-SERS probe injection and SERS spectra were measured at major organ such as liver, spleen, kidney and heart in order to confirm SERS probe deposition at organ site. Then, 1.5 mL of whole blood was collected by heart puncture; 0.5 mL blood was collected in 10% EDTA for complete blood count (CBC) and the remaining 1 mL whole blood was collected and serum was separated for biochemistry panel assay. The test includes examining the level of various enzymes such as alanine aminotransferase (ALT), γ-glutamyl transferase (GGT), alkaline phosphatase (ALP), and protein such as albumin and bilirubin.

1.6 Cell Internalization and Cell-tracking *In Vivo*

A Lab-tek glass chamber slide (Nalge Nunc International) containing A549 cells (6×10^5) was incubated for 24 h and mixed with the as-prepared NIR-SERS probe solution for 12 h. After washing the slide several times with PBS solution, the cells were fixed with paraformaldehyde (4%) for 10 min at 37 ^{o}C. The chamber slides were washed and dried for Raman measurements. For cell-tracking *in vivo* with SERS spectroscopy, the A549 cells (6×10^5) were incubated with the NIR-SERS probe$_{[4FBT]}$ (0.1 nM in PBS) for 18 h. After trypsinization, the harvested A549 cells containing the NIR-SERS probe$_{[4FBT]}$ (in 100 μL PBS) were subcutaneously implanted into a gluteal region of a 8-week-old male nude mouse. This study was approved by the Seoul National University Institutional Animal Care and Use Committee (IACUC No. SNU-130423-2).

1.7 Discrete Dipole Approximation (DDA) Calculation for Local Field Distribution of Bumpy AgNS

The electric field near AgNSs was calculated by the DDSCAT 7.1 package. In our simulation, isotropic dipoles are evenly placed in an Ag shell at dipole–dipole distances of 3 nm. These nanoshells were 27 nm in thickness and 204 nm in diameter, and silica core was 150 nm in diameter. The bumpy nanostructures were assumed half sphere structures with 21 nm in radius. The bumpy AgNS has ~250000 dipoles. The incident radiation is along the *z* direction, with a y direction polarization. E-field distribution was calculated as $/E/E_0/^2$, where E is magnitude of the scattered electromagnetic field and E_0 is magnitude of the incident electromagnetic field.

1.8 Raman Instrument

Raman measurement was conducted using a confocal microscope Raman system (LabRam 300, JY-Horiba, Edison, NJ, USA) equipped with an optical microscope (Olympus, Tokyo, Japan) and optical fiber coupled portable-Raman system (B&W TEK, i-Raman). In the micro Raman system, Raman scattering signals were collected in a back-scattering geometry and detected using a spectrometer equipped with a thermo-electrically cooled (-70 ^{o}C) CCD detector. The excitation laser was focused and the Raman signals were collected using a 100× objective lens (NA 0.90, Olympus). In the portable-Raman system, the system is equipped with a diode laser emitting at 785 nm. The diffraction grating limits the spectral range of 3200–175 cm^{-1} with a spectral resolution of 3 cm^{-1}. The maximal output power of the diode laser at the source is 300 mW.

1.9 SERS Measurement

For single particle SERS mearsurement, the Raman label-adsorbed AgNS suspension (0.1 mg/mL in ethanol) was dropped on a patterned slide glass, and SERS spectra was measured by point-by-point mapping with a 1 μm step size. The mapping experiments were carried out using a ×100 objective lens (NA 0.90) with 785 nm photo-excitation of 28 μW laser power and a 10 s acquisition time. After the SERS measurement, the same area of Raman mapping was observed using field emission-scanning electron microscopy (JSM-6701F, JEOL, Tokyo, Japan) to ensure that only single particles For in vivo SERS measurement, each male mouse was anesthetized via an intraperitoneal injection of ketamine (50 mg kg^{-1}) and xylazine (2.5 mg kg^{-1}). SERS spectra were obtained from NIR-SERS $probe_{[4FBT]}$ labeled A549 cells injected site using the portable-Raman system with a 785 nm excitation of 90 mW laser power and 30 s acquisition time.

2. Results and Discussion

2.1 Synthesis of Bumpy AgNS

The synthetic scheme for bump-structured AgNS as a SERS substrate is shown in Figure 3-1. For the seedless and single-step fabrication of AgNS with a uniform bumpy surface, thiol-functionalized silica nanospheres (*ca.* 150 nm in diameter) were used as a dielectric core. The thiol functional group plays a crucial role in the complete and uniform formation of AgNS on the silica surface due to its high affinity with Ag. Bumpy AgNS were then synthesized via direct and fast reduction of a silver precursor ($AgNO_3$) on the silica surface in the presence of octylamine without deposition of seed metals. In this process, octylamine was used as a reducing agent[160] as well as a capping ligand,[161] which is very important for the fast formation of the silver shell under a mild condition (1h, 25 ^{o}C) and for the control of its morphology and coverage on the silica surface.[66,162] Silver ions (Ag^{+}) can be readily reduced by octylamine via a single electron transfer from an amino group in a symmetric diol solution (ethylene glycol), which leads to the nucleation of Ag^{0} to form a silver shell on the silica surface. The fast reduction kinetics of Ag^{+} at room temperature might be attributed to an increase in the reduction potential of Ag^{+} by creating an Ag^{+}/symmetric diol chelate, compared to that of Ag^{+}/ethanol chelate[163,164] (A comparison of

reduction potential from the cyclic voltammetry data was shown in Figure 3-2). This increased reduction potential of Ag^+ ions enables them to be effectively reduced by the octylamine at room temperature, which leads to the facile formation of the silver shell in a short period of time. However, in the absence of octylamine, the silver shell did not form on the silica surface. In addition, when ethylene glycol monoethyl ether or ethanol was used as a reaction medium instead of ethylene glycol, AgNS did not form on the silica surface at 25 ^oC as shown in Figure 3-3. This result clearly indicates that the monohydroxyl group could not chelate Ag^+ ions as effectively as a symmetric diol.

The typical scanning electron microscopy (SEM) images of the AgNSs, which were synthesized from 1mg of thiol-functionalized silica nanospheres, 3.5 mM of $AgNO_3$, and 5 mM of octylamine, are shown in Figures 3-1b and 3-1c. The low magnification of SEM image suggests that the size of AgNS is uniform (301 ± 17 nm) and a portion of the incompletely covered AgNS was less than 1 % (counted from ~400 AgNSs). According to the elemental mapping results with energy dispersive X-ray spectroscopy (EDX), the only Ag atom was observed and there was no Si atom detected from the silica particle (Figure 3-4), indicating that the thick silver shell fully covers the silica surface without any vacant sites. As shown in Figure 3-1c, it is interesting that, without post-treatment such as further deposition or chemical etching process,[151,165] the surface topography of AgNS has a very

rough structure with 20-30 nm sized bumps rather than a smooth surface. This bumpy surface can induce stronger electromagnetic field enhancement than a smooth surface, which amplifies the SERS signal.[44,134,147] The typical X-ray diffraction (XRD) pattern of the bumpy AgNS is shown in Figure 3-1d. The sharp diffraction peaks corresponding to the metallic Ag with a face-centered-cubic (fcc) phase suggest the formation of high crystalline Ag.[138]

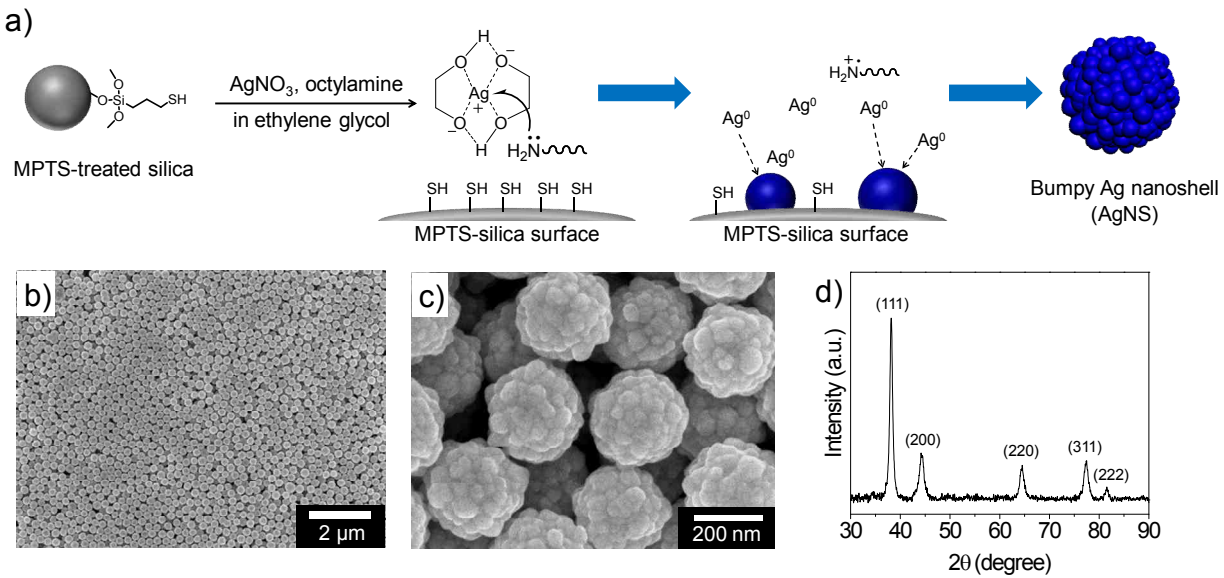

Figure 3-1. Synthesis and characterization of bumpy Ag nanoshell (AgNS). a) Schematic illustration for the seedless and single-step synthesis of bumpy AgNS via reduction of Ag^+ by octhylamine in ethylene glycol solution. Representative SEM image of bumpy AgNS at low magnification and, c) at high magnification, showing narrow size distribution and bumpy surface nanostructure. d) XRD pattern of bumpy AgNS showing metallic Ag with a face-centered-cubic (fcc) phase.

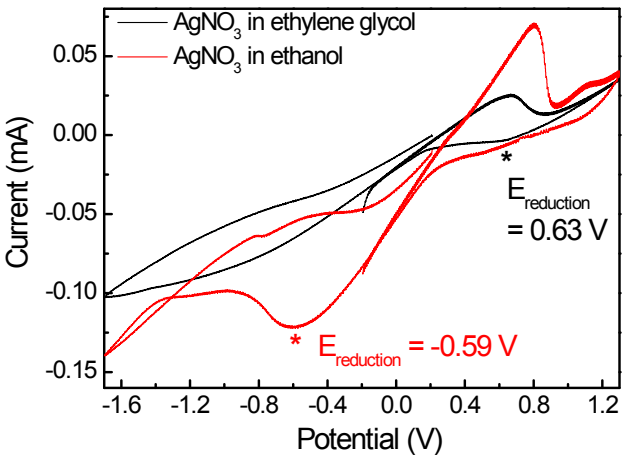

Figure 3-2. Cyclic voltammograms for comparison of reduction potential between $AgNO_3$ in ethylene glycol and in ethanol. Experimental condition; 10mM concentration of $AgNO_3$, Au working electrode, Pt counter electrode, Ag/AgCl reference electrode, scan range from −1.7 to 1.3 V, scan rate of 50 mV s^{-1}.

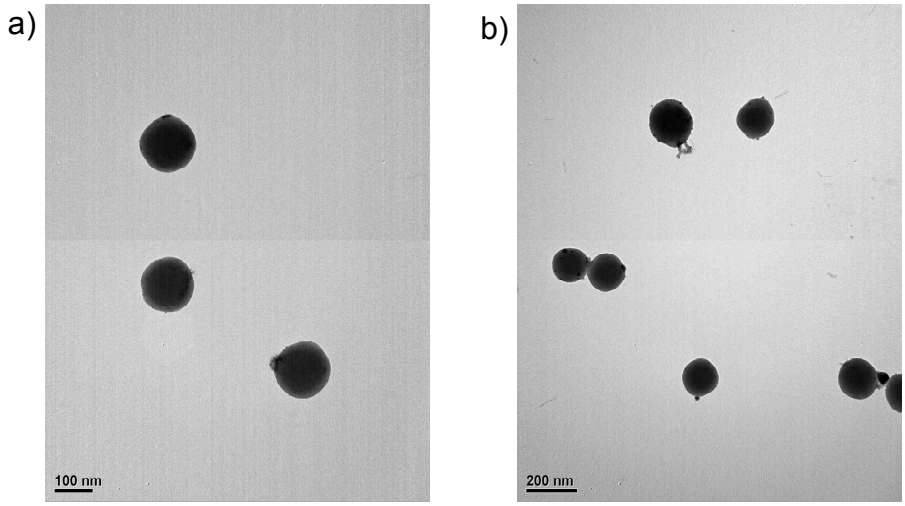

Figure 3-3. TEM images of silica nanoparticles after treating with $AgNO_3$ and octylamine in (a) ethanol, and (b) ethylene glycol monoethyl ether for 1h at room temperature.

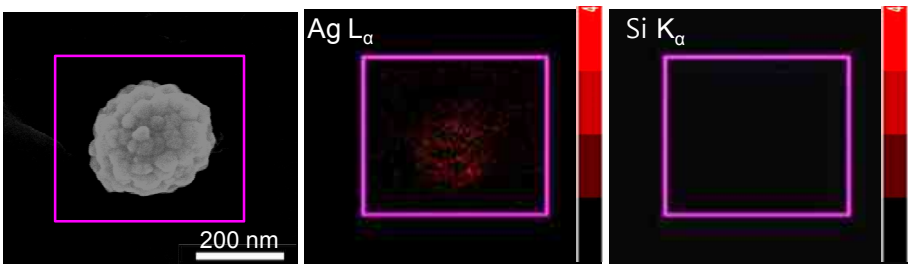

Figure 3-4. Elemental mapping images of bumpy AgNS by EDX analysis.

2.1 Thickness Control of Bumpy AgNS

Next, we attempted to determine whether this seedless and single-step method could tune the thickness of the silver shell. The weight ratio of $AgNO_3$ to silica nanospheres (SiNP) [$AgNO_3$/SiNP] in solution was varied from 7.5 to 30 by decreasing the amount of SiNP. For the expression of weight ratio of each sample, the AgNS synthesized at weight ratio of 7.5, for example, was denoted as AgNS-7.5, in which the number indicates the weight ratio. Transmission electron microscopy (TEM) images of AgNS obtained from each reaction condition are shown in Figures 3-5a–3-5d. The thickness of the silver shell gradually increases from ~32 nm (AgNS-7.5) to ~76 nm (AgNS-30) with an increase in the weight ratio of $AgNO_3$ to SiNP, suggesting that the thickness of the silver shell can be easily controlled in the seedless and single-step synthesis (details of their size and shell thickness are shown in Table 3-1). It should be noted that the surface topography of AgNS remains bumpy, regardless of the silver shell thickness (Figure 3-6). The plasmonic absorption spectra of AgNS are shown in Figure 3-5e. All AgNSs exhibit broad extinction bands from the visible to NIR region (560 nm - 1000 nm). The large extension of the plasmonic absorption bands of AgNS is attributed to the shell and bumpy structure. The broad absorption feature of AgNS from the visible region to the NIR region is beneficial to the effective excitation of AgNS by NIR incident light. The color of the bumpy

AgNS solution was changed from bluish to brownish with the increase of shell thickness (Figure 3-5f).

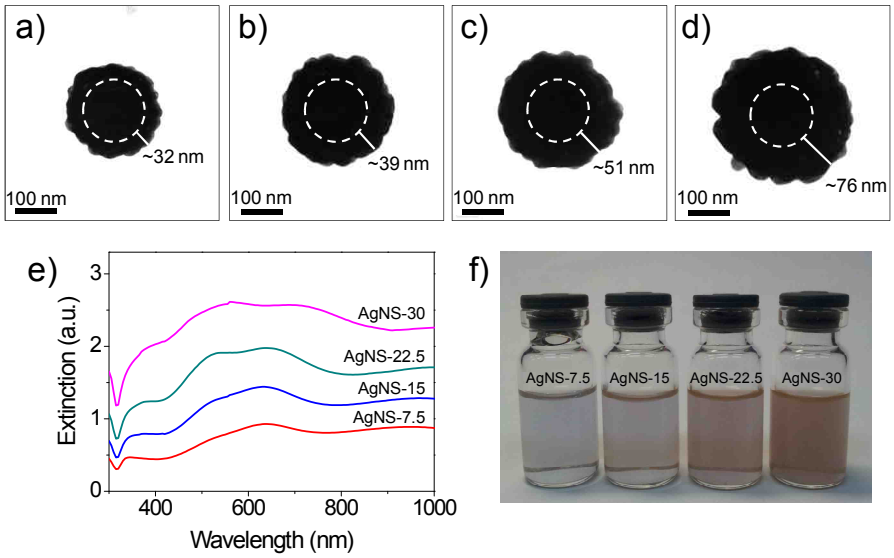

Figure 3-5. Control of silver shell thickness of bumpy AgNS and its optical properties. a) TEM images of AgNS obtained at a weight ratio [$AgNO_3$/SiNP] of 7.5, b) 15, c) 22.5, and d) 30, respectively. White dotted circles indicate a silica nanosphere core (~150 nm in diameter). The silver shell thickness increased gradually from ~32 nm to ~76 nm. e) Absorption spectra of bumpy AgNS. f) Photographs of bumpy AgNS solutions. The numbers in abbreviation AgNS indicate a weight ratio, [$AgNO_3$/SiNP], during synthesis.

Table 3-1. Size and Silver shell Thickness of AgNS as a Function of Weight Ratio of $AgNO_3$ to Silica Nanoparticles, [$AgNO_3$/SiNP] (Counted from 30 AgNSs).

[$AgNO_3$/SiNP]	Size of silver shell (nm)	Shell Thickness (nm)
7.5	214 ± 16	~32
15	228 ± 16	~39
22.5	251 ± 16	~51
30	301 ± 17	~76

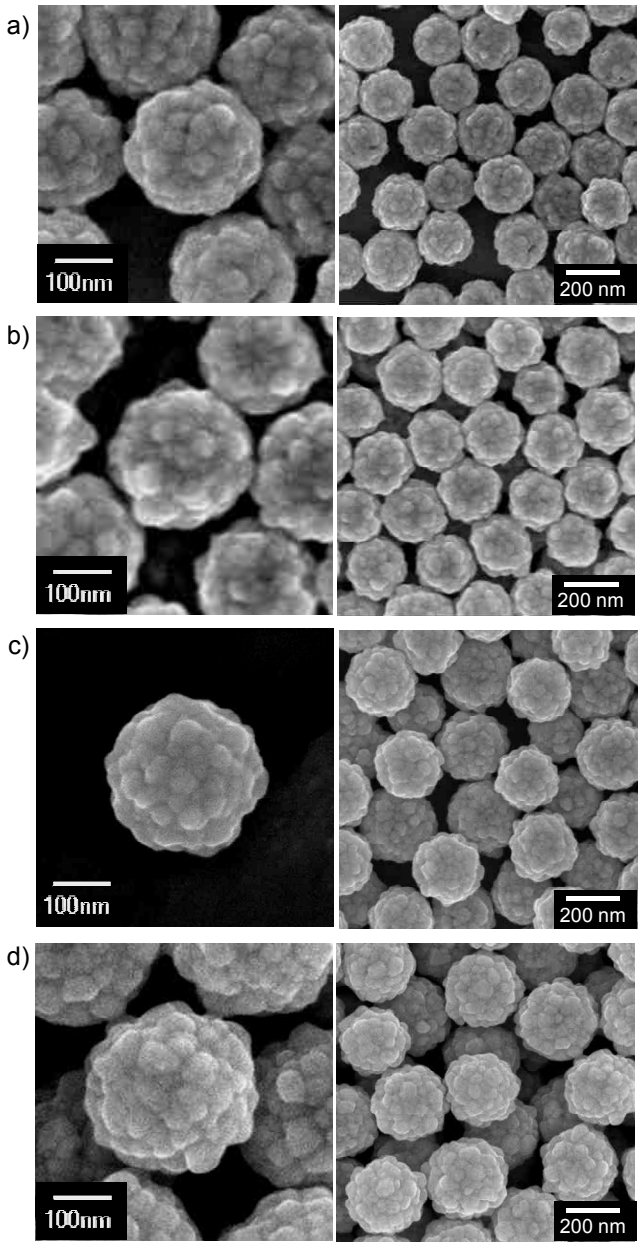

Figure 3-6. SEM images showing the size and surface morphology of bumpy AgNSs that were synthesized at different weight ratios of AgNO3 to SiNP. High magnification (left) and low magnification (right); Weight ratios of $AgNO_3$ to SiNP are a) 7.5, b) 15, c) 22.5, and d) 30, respectively.

2.3 Evaluation of SERS Activity of Bumpy AgNS

We then conducted SERS measurements on bumpy AgNSs (AgNS-7.5, 15, 22.5, and 30) of different thickness to evaluate their SERS activity in the NIR window. After 4-fluorobenzenethiol (4-FBT) was adsorbed on the surface of AgNSs as a Raman label, the SERS intensity of 4-FBT Raman band at 1075 cm^{-1} was measured by NIR photo-excitation (785 nm). As shown in Figure 3-7a, AgNS-15 with a shell thickness of ~39-nm exhibited the strongest SERS intensity under NIR laser excitation. In order to get further insights on the SERS effect of AgNS as a function of excitation wavelength, laser lights with three different wavelengths (532, 647, and 785 nm) were irradiated to AgNS-15. Bumpy AgNS-15 generates SERS signals of 4-FBT for all the laser-lines as can be anticipated from its broad extinction band (Figure 3-7b). However, the strongest SERS intensity was obtained by NIR excitation at 785 nm, which is 1.7 times larger than that by the visible excitation at 532 nm. In order to understand the optical features of broad excitation of SERS and wavelength dependence from visible to NIR range, the electric field (E-field) enhancements on the bumpy AgNS was calculated using the discrete dipole approximation (DDA) at three different excitation laser lines at 532, 647, and 785 nm (Figures 3-7c–3-7e). The dimension of bumpy Ag NS was defined based on the electron microscope images. The DDA calculation revealed that the E-field is enhanced near the

bumpy AgNS surface for all wavelengths and its distribution gradually increased as wavelength of incident light caries from visible to NIR region. In addition, highly localized E-field at the tip of the bumpy AgNS surface was shown under the NIR incidence (785 nm), which is 2.3 times larger than that under visible incidence (532 nm). These simulation results demonstrate that AgNS can generate strongest SERS signals at the NIR excitation.

Furthermore, we performed SERS measurement on a single AgNS particle in the NIR window as previously reported.[60] Briefly, after the AgNS suspension was drop-cast on a patterned silicon wafer, SERS was measured by point-by-point mapping with a step size of 1 μm, an integration time of 10 s, and 785-nm photo-excitation of 28-μW laser power. Then, the same area of Raman mapping was imaged with SEM to correlate the Raman map and SEM image to ensure single particles. Figure 3-8a shows the overlaid image of the SERS intensity map with the SEM image of single AgNS particles, indicating that SERS mapping exactly corresponds to the position of each single particle. In addition, Figure 3-8b shows a typical spectrum obtained from single particle SERS measurement. Figures 3-8a and 3-8b demonstrate that the SERS signals of 4-FBT adsorbed on single AgNS particles is strong enough to be detected in the NIR window (average SERS enhancement factor value is 6.4×10^5). Such highly sensitive SERS effect can be attributed to the bumpy structure of AgNS that has four times stronger E-field enhancement than smooth AgNS or AuNS (Figure 3-9).

According to the results achieved so far, bumpy AgNS-15 with a thickness of 39 nm is the most suitable NIR-active SERS substrate for sensitive detection and bio-imaging. We then prepared four kinds of SERS nanoprobes by introducing different Raman labels including 4-bromobenzenethiol (4-BBT), 4-FBT, 4-chlorobenzenethiol (4-CBT), and 4-aminobenzenethiol (4-ABT) on bumpy AgNS, which are denoted NIR-SERS probe$_{[4BBT]}$, NIR-SERS probe$_{[4FBT]}$, NIR-SERS probe$_{[4CBT]}$ and NIR-SERS probe$_{[4ABT]}$, respectively. Each NIR-SERS probe has its own SERS spectrum without overlapping with the others (Figure 3-8c), and thus can be used as a unique barcode in the multiplexed detection of various target molecules.

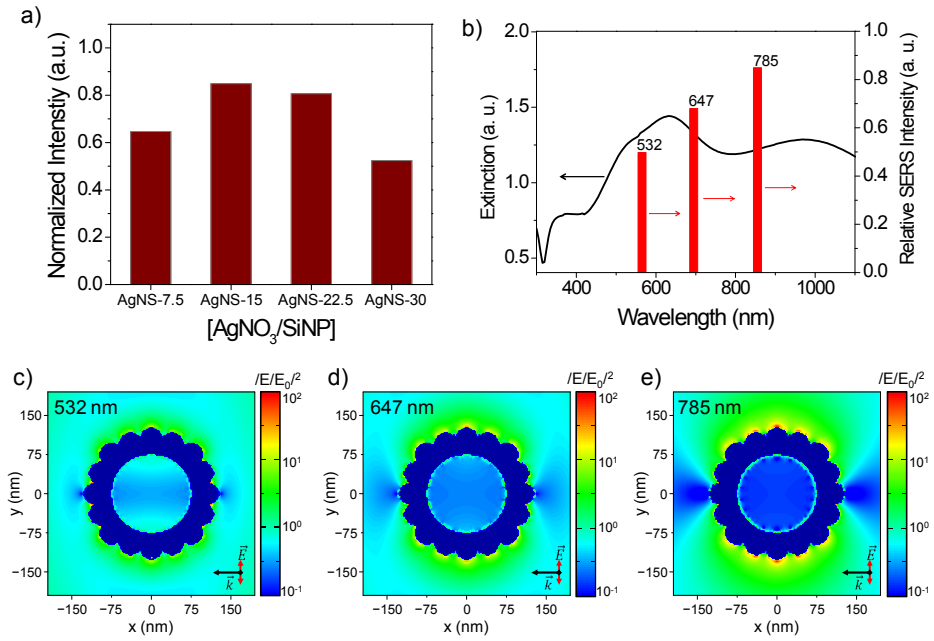

Figure 3-7. SERS effect and E-field distribution of bumpy AgNS. a) Normalized SERS intensity of the peak at 1075 cm^{-1} for 4-fluorobenzenethiol (4-FBT) adsorbed on four kinds of AgNSs prepared at the different weight ratios of $AgNO_3$ to SiNP from 7.5 to 30. SERS intensities were normalized by the Raman intensity of the ethanol peak at 882 cm^{-1} b) Relative SERS intensity of the peak at 1075 cm^{-1} for 4-FBT on AgNS-15 under different excitation laser lines (532, 647, and 785 nm, respectively). Calculated E-field distribution of bumpy AgNS-15 under c) 532, d) 647, and e) 785 nm excitation laser lines using discrete dipole approximation (DDA). The nanoshells have a 27 nm of shell thickness, a 204 nm of diameter, and a 150 nm of silica core. The bumpy nanostructures were assumed to have half sphere structures with 21 nm in radius.

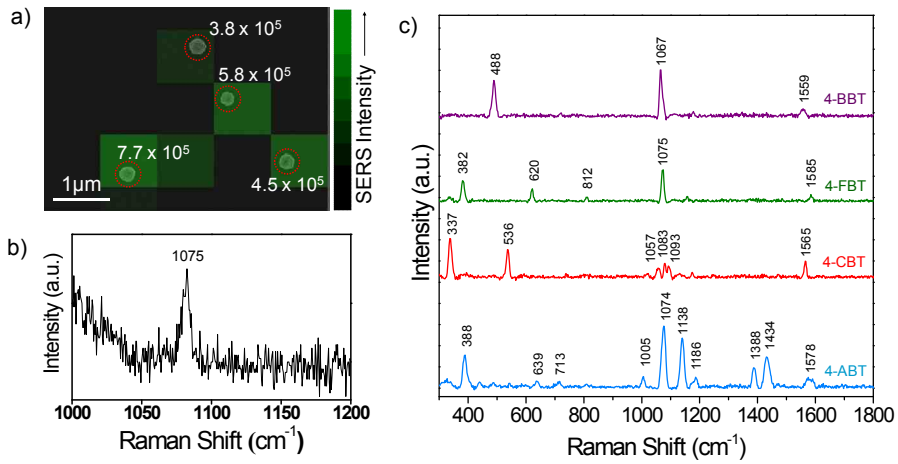

Figure 3-8. Signal sensitivity and multiplexcity of bumpy AgNS basedNIR-SERS probes. a) SERS intensity map with enhancement factor values of single AgNS particle bearing 4-FBT; the intensity map was overlaid with its corresponding SEM image. d) SERS spectrum obtained from a single AgNS particle bearing 4-FBT. e) SERS spectra of simple aromatic compounds such as 4-bromobenzenethiol (4-BBT), 4-FBT, 4-chlorobenzenethiol (4-CBT), and 4-aminobenzenethiol (4-ABT) on bumpy AgNS.

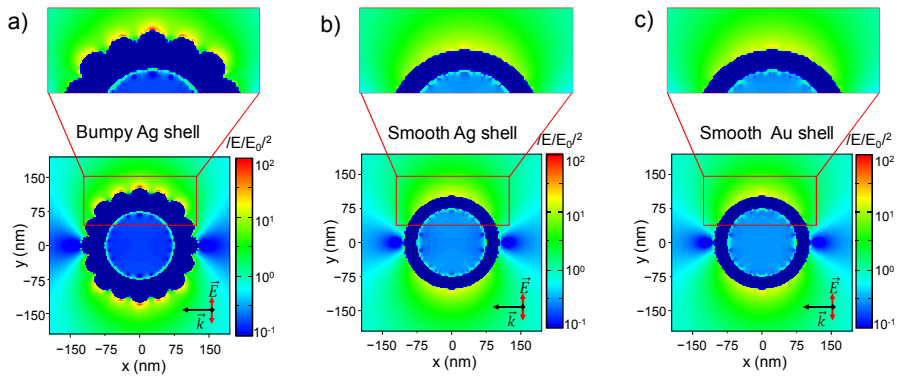

Figure 3-9. Calculated local electric field distribution of a) bumpy AgNS-15, b) smooth Ag shell, and c) smooth Au shell under 785 nm excitation laser lines using discrete dipole approximation (DDA). These nanoshells were 27 nm in thickness and 204 nm in diameter, and silica core was 150 nm in diameter. The bumpy nanostructures were assumed half sphere structures with 21 nm in radius.

2.4 Toxicity and Colloidal Stability Tests of PEGylated NIR-SERS Probe

To improve a biocompatibility and a colloidal stability of the NIR-SERS probes, their surface was treated with methoxy poly(ethylene glycol) sulfhydryl (mPEG-SH, MW 5000) (Figure 3-10a). PEG polymers are well known to not only prevent NPs from their aggregation and degradation in biological systems but also improve their circulation time *in vivo*.[24,126] In order to confirm the effect of PEGylation on the colloidal and signal stability of NIR-SERS probes$_{[4FBT]}$, the SERS signals of a PEGylated NIR-SERS probe$_{[4FBT]}$ and a non-PEGylated NIR-SERS probe$_{[4FBT]}$ were obtained in the course of time. As shown in Figure 3-11, no significant decrease in the SERS intensities was observed from both NIR-SERS probes$_{[4FBT]}$ stored at room temperature and PEGylated NIR-SERS probe$_{[4FBT]}$ at relatively higher temperature (50 ^{o}C). However, the two-fold higher SERS signal was obtained from the non-PEGylated NIR-SERS probe$_{[4FBT]}$ due to its aggregation creating "SERS hot spots" after 1 day incubating at 50 ^{o}C. The surface morphology of both NIR-SERS probes$_{[4FBT]}$ remained same after the stability test for a certain period of time according to TEM analysis (Figure 3-12). Therefore, we concluded that the PEGylated NIR-SERS probe is so quite stable to be applicable to long-term cell tracking *in vivo*. To investigate *in vivo* toxicity of the PEGylated NIR-SERS probe$_{[4FBT]}$, we conducted

hematologic evaluation and liver function test and histologic evaluation after tail vein injection of the PEGylated NIR-SERS probe$_{[4FBT]}$ (dose=50 mg/kg; based on Ag weight) to live mice. All mice were sacrificed at the same time, 3 days after injection of the NIR-SERS probe. As shown in Figure 3-13, SERS signals of the NIR-SERS probe$_{[4FBT]}$ were detected from the major organs such as liver and spleen where nanoparticles are normally accumulated[166]. Hematologic evaluation result showed that hematological markers' level for analysis, white blood cells, hemoglobin, and platelets were not significantly changed in the NIR-SERS probe treated mice compared with a control group (Table 3-2). In addition, no significant changes in the level of alkaline phosphate (ALP), alanine aminotransferase (ALT), total bilirubin, albumin, cholesterol, and γ-glutamyl transferase (GGT) (Table 3-3) were observed. There was no tissue damage, inflammation, or morphological change in any organs (liver, spleen, kidney, and heart), and no significant difference of histologic evaluation as well between the NIR-SERS probe treated mice and the control mice (Figure 3-14). These results obtained so far indicate that a testing dose of NIR-SERS probe (< 50 mg/kg) did not cause any *in vivo* toxicity, which is very important for further biomedical applications.

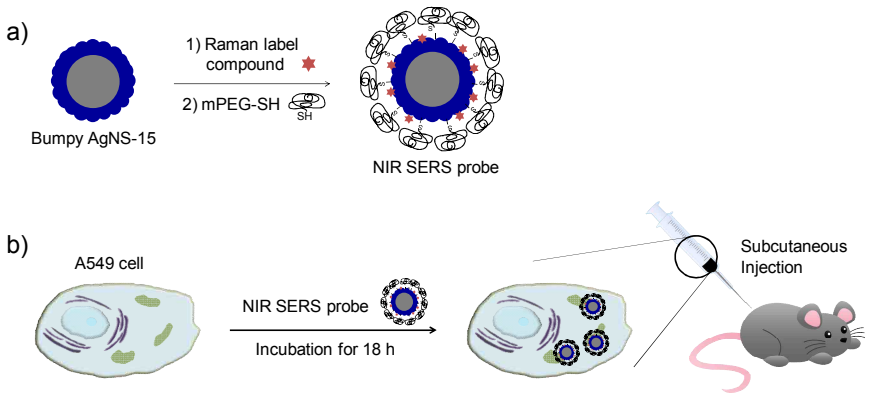

Figure 3-10. Schematic illustration for a) SERS coding and PEGylation of bumpy AgNS for NIR-SERS probe coded with 4-FBT, denoted as NIR-SERS probes$_{[4FBT]}$, and b) cellular uptake of NIR-SERS probes$_{[4FBT]}$ and subcutaneous injection of the cell suspension into a mouse.

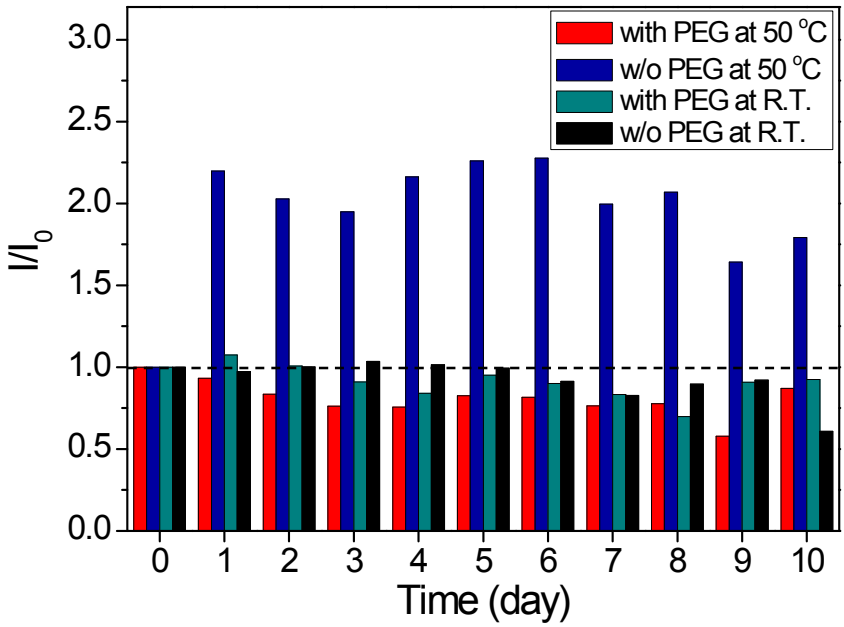

Figure 3-11. SERS signal intensities from various conditions of NIR-SERS probes; NIR-SERS probe$_{[4FBT]}$ stored at 50 °C with PEG ligands (red) and without PEG ligands (blue). And, NIR-SERS probe$_{[4FBT]}$ stored at room-temperature with PEG ligands (dark cyan) and without PEG ligands (black).

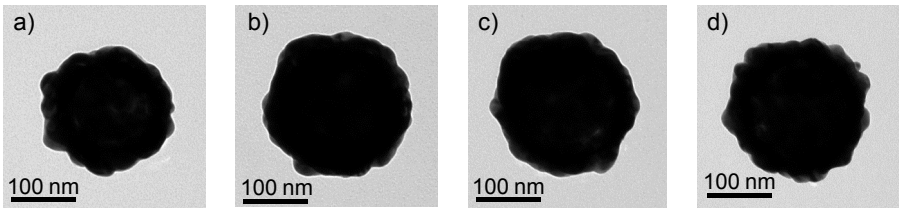

Figure 3-12. TEM images of NIR-SERS probes after 9 days storing; a) NIR-SERS probe$_{[4FBT]}$ stored at 50 ^{o}C with PEG ligands and b) without PEG ligands. c) NIR-SERS probe$_{[4FBT]}$ stored at room-temperature with PEG ligands and d) without PEG ligands.

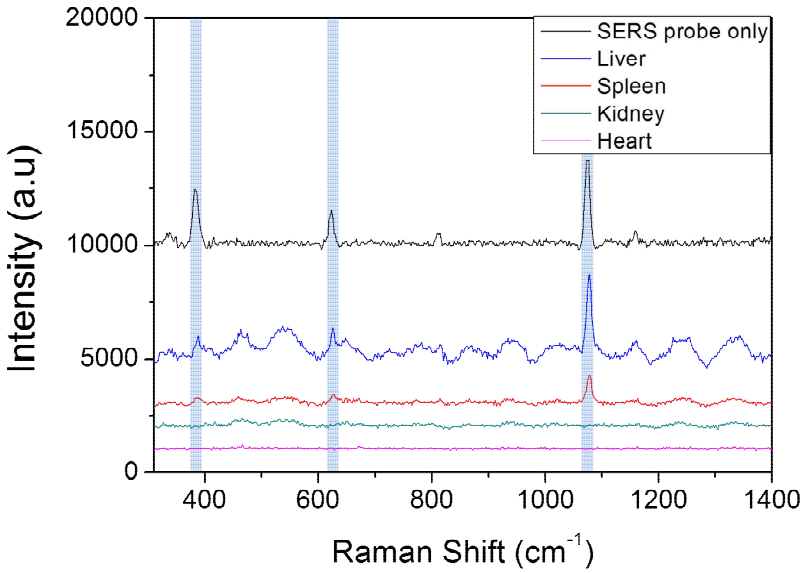

Figure 3-13. Raman spectra from mice major organs (liver, spleen, kidney, and heart) after tail vein injection of NIR-SERS probes$_{[4FBT]}$ (dose=50 mg/kg).

Table 3-2. Hematology Results from Animals Treated with NIR SERS Probes

	White blood cells (Counts/μL)	Hemoglobin (g/dL)	Platelets (Counts/μL)
Control	4600±1800	12.0±1.2	675700±236400
50 mg/kg[a] treatment	5600±1900	10.9±0.9	564300±201800

[a]Concentration based on Ag weight in Ag NSs.

Table 3-3. Liver Function Results from Mice Treated with NIR-SERS Probes

	Alkaline phosphatase (U/L)	Alanine aminotransferase (U/L)	Total bilirubin (mg/dL)	Albumin (g/dL)	Cholesterol (mg/dL)	γ-Glutamyl transferase (U/L)
Control	61.7±14.2	46.7±1.5	0.3±0	3.1±0.06	97.0±11.5	<5
50 mg/kg[a] treatment	81.7±5.9	49.3±2.4	0.3±0	2.7±0.15	96.3±11.6	<5

[a]Concentration based on Ag weight in Ag NSs.

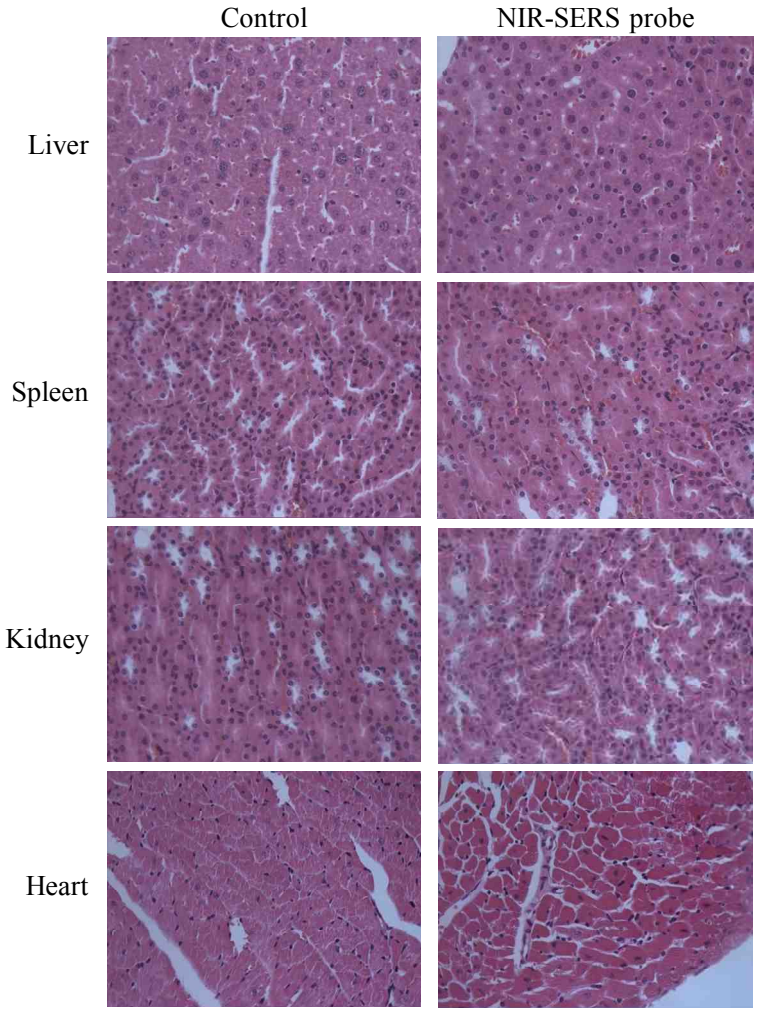

Figure 3-14. Histological staining of major organs from NIR-SERS probes-treated mice. H&E staining for liver, spleen, kidney, and heart (top to bottom). The left column shows tissues from control mice. The right column shows tissues from NIR-SERS probe treated mice.

2.5 Application of NIR-SERS Probes to *In Vivo* Cell Tracking

Finally, NIR-SERS probes were applied to cell-tracking in a xenograft mouse model. After internalization of the NIR-SERS probes$_{[4FBT]}$ into adenocarcinomic human alveolar basal epithelial cells (A549 cells), the A549 cell suspension was subcutaneously injected into a nude mouse (Figure 3-10b). First, we confirmed whether or not the NIR-SERS probes$_{[4FBT]}$ were successfully internalized into A549 cells by using a confocal micro-Raman system before cell-tracking *in vivo*. As shown in Figures 3-15a and 3-15b, the intense SERS signal of the NIR-SERS probe$_{[4FBT]}$ was observed from the A549 cells after incubation with the NIR-SERS probes$_{[4FBT]}$ while there was no SERS signal from the cells without treatment of NIR-SERS probes. This result indicates that NIR-SERS probes can be internalized into A549 cells via natural endocytosis. In addition, the NIR-SERS probe$_{[4FBT]}$ showed no significant cytotoxicity in A549 cells up to 0.1 nM (100 μL) concentration as shown in Figure 3-16 in Supporting Information. After the subcutaneous injection of A549 cells (100 μL, 6×10^5 mL^{-1}) containing the NIR-SERS probes$_{[4FBT]}$ into a gluteal region of a nude mouse, the SERS spectra were measured from the injected region using an optical fiber coupled portable Raman with 785 nm photo-excitation (Figure 3-15c). As shown in Figures 3-15d and 3-15e, the intense SERS signal of the NIR-SERS probe$_{[4FBT]}$ was observed from the injected area of the mouse

immediately after cell injection. In addition, the SERS signal remained intense for two days after injection. However, the SERS intensity of the peak at 1075 cm^{-1} decreased after three days. We speculate that this diminution of the SERS signal could be caused by cell division that leads to the dilution of the NIR-SERS $probe_{[4FBT]}$ inside the cells as previously reported.[167] This result reveals that NIR-SERS probes based on bumpy AgNS were successfully applied to cell tracking in living animals using a portable Raman system.

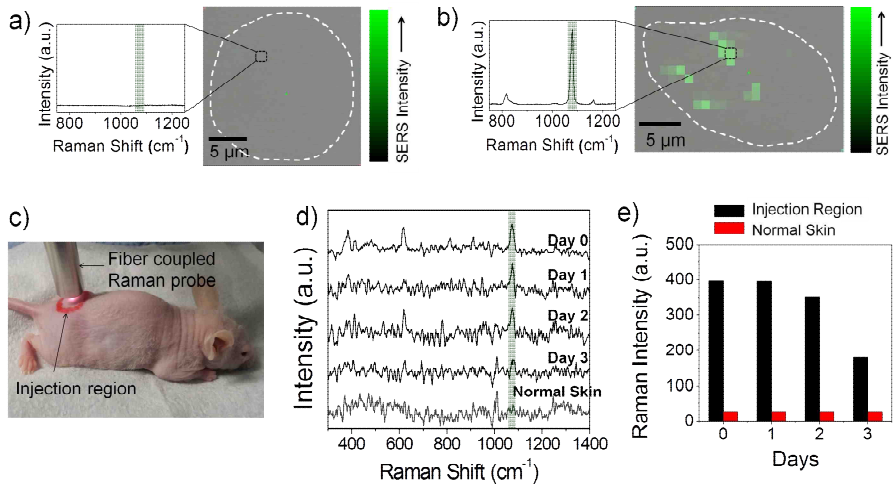

Figure 3-15. *In vivo* cell tracking using NIR-SERS probes. a) SERS intensity map of A549 cell without treatment of NIR-SERS probes$_{[4FBT]}$, and b) with treatment of NIR-SERS probes$_{[4FBT]}$; The SERS intensity map was overlaid with the optical image of the cell. White dotted lines indicate a cell boundary. The 785 nm photo-excitation of 31 mW laser power and light acquisition time of 1 s. c) A photograph showing the area of a mouse where A549 cells containing NIR-SERS probes$_{[4FBT]}$ were injected, and an optical fiber coupled Raman probe. d) SERS spectra of NIR-SERS probes$_{[4FBT]}$ obtained from a mouse as a function of time after injection periods from 0 to 3 days with the 785 nm photo-excitation of 90 mW laser power and light acquisition time of 30 s. e) SERS intensity of the peak appearing at 1075 cm^{-1} in the spectra shown in (d).

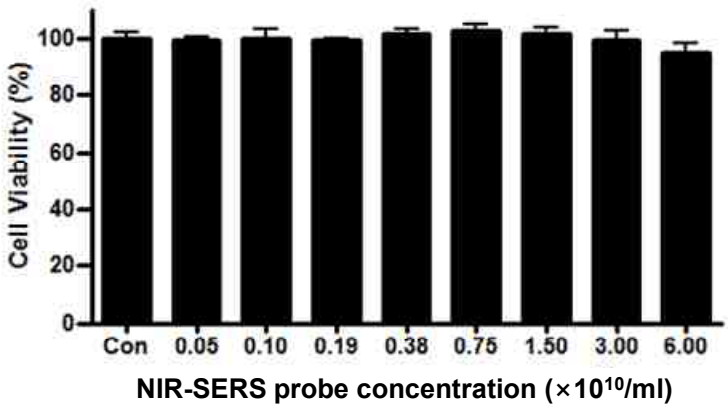

Figure 3-16. Cytotoxicity of NIR-SERS probes using MTT assay. The MTT assay was performed against A549 cells at 37 °C as a function of NIR-SERS probe concentrations (100 μl) after incubation of the cells with NIR-SERS probes for 18 h.

3. Conclusion

We developed a seedless and single-step synthetic method for the fast and uniform fabrication of bumpy AgNS, of which plasmonic absorption was tuned by adjusting the thickness of the silver shell. Bumpy AgNS significantly amplified the Raman signals of small aromatic compounds under NIR photo-excitation. The AgNS-based nanoprobes (NIR-SERS probes), were successfully applied to cell tracking *in vivo* without any cytotoxicity. In addition to cell tracking *in vivo*, the NIR-SERS probes have high potential to be applied to various biological systems as sensitive and multiplexing nanoparticle labels.

References

1. Wang, Y. and Schlücker, S. Rational design and synthesis of SERS labels. *Analyst* **138**, 2224-2238, (2013).

2. Nie, S. and Emory, S. R. Probing single molecules and single nanoparticles by surface-enhanced Raman scattering. *Science* **275**, 1102, (1997).

3. Kneipp, K., Wang, Y., Kneipp, H., Perelman, L. T., Itzkan, I., Dasari, R. R. and Feld, M. S. Single molecule detection using surface-enhanced Raman scattering (SERS). *Physical Review Letters* **78**, 1667-1670, (1997).

4. Kottmann, J. P. and Martin, O. J. Retardation-induced plasmon resonances in coupled nanoparticles. *Optics Letters* **26**, 1096-1098, (2001).

5. Xu, H., Aizpurua, J., Käll, M. and Apell, P. Electromagnetic contributions to single-molecule sensitivity in surface-enhanced Raman scattering. *Physical Review E* **62**, 4318-4324, (2000).

6. Campion, A. and Kambhampati, P. Surface-enhanced Raman scattering. *Chemical Society Reviews* **27**, 241-250, (1998).

7. Moskovits, M. Surface-enhanced spectroscopy. *Reviews of Modern Physics* **57**, 783-826, (1985).

8. Vo-Dinh, T. Surface-enhanced Raman spectroscopy using metallic nanostructures. *TrAC Trends in Analytical Chemistry* **17**, 557-582, (1998).

9. Jeong, D. H., Kim, G., Lee, Y.-S. and Jun, B.-H. (ed Challa S. S. R. Kumar) 261-289 (Springer Berlin Heidelberg, 2012).

10. Sun, L., Yu, C. and Irudayaraj, J. Surface-enhanced Raman scattering based nonfluorescent probe for multiplex DNA detection. *Analytical Chemistry* **79**, 3981-3988, (2007).

11. Lutz, B. R., Dentinger, C. E., Nguyen, L. N., Sun, L., Zhang, J., Allen, A. N., Chan, S. and Knudsen, B. S. Spectral analysis of multiplex Raman probe signatures. *ACS Nano* **2**, 2306-2314, (2008).

12. Gellner, M., Küstner, B. and Schlücker, S. Optical properties and SERS efficiency of tunable gold/silver nanoshells. *Vibrational Spectroscopy* **50**, 43-47, (2009).

13. Sanles-Sobrido, M., Exner, W., Rodríguez-Lorenzo, L., Rodríguez-González, B., Correa-Duarte, M. A., Álvarez-Puebla, R. A. and Liz-Marzán, L. M. Design of SERS-encoded, submicron, hollow particles through confined growth of encapsulated metal nanoparticles. *Journal of the American Chemical Society* **131**, 2699-2705, (2009).

14. Doering, W. E., Piotti, M. E., Natan, M. J. and Freeman, R. G. SERS as a foundation for nanoscale, optically detected biological labels. *Advanced Materials* **19**, 3100-3108, (2007).

15. Schlücker, S. SERS microscopy: nanoparticle probes and biomedical applications. *ChemPhysChem* **10**, 1344-1354, (2009).

16. Jun, B. H., Kim, G., Noh, M. S., Kang, H., Kim, Y. K., Cho, M. H., Jeong, D. H. and Lee, Y. S. Surface-enhanced Raman scattering-active nanostructures and strategies for bioassays. *Nanomedicine* **6**, 1463-1480, (2011).

17. Rohr, T., Cotton, T., Fan, N. and Tarcha, P. Immunoassay employing surface-enhanced Raman spectroscopy. *Analytical biochemistry* **182**, 388-398, (1989).

18. Qian, X., Peng, X. H., Ansari, D. O., Yin-Goen, Q., Chen, G. Z., Shin, D. M., Yang, L., Young, A. N., Wang, M. D. and Nie, S. In vivo tumor targeting and spectroscopic detection with surface-enhanced Raman nanoparticle tags. *Nature Biotechnology* **26**, 83-90, (2008).

19. Stuart, D. A., Yuen, J. M., Shah, N., Lyandres, O., Yonzon, C. R., Glucksberg, M. R., Walsh, J. T. and Van Duyne, R. P. In vivo glucose

measurement by surface-enhanced Raman spectroscopy. *Analytical Chemistry* **78**, 7211-7215, (2006).

20. Stone, N., Faulds, K., Graham, D. and Matousek, P. Prospects of deep Raman spectroscopy for noninvasive detection of conjugated surface enhanced resonance Raman scattering nanoparticles buried within 25 mm of mammalian tissue. *Analytical Chemistry* **82**, 3969-3973, (2010).

21. Wang, Y., Seebald, J. L., Szeto, D. P. and Irudayaraj, J. Biocompatibility and biodistribution of surface-enhanced Raman scattering nanoprobes in Zebrafish embryos: *In vivo* and multiplex imaging. *ACS Nano* **4**, 4039-4053, (2010).

22. Zavaleta, C. L., Smith, B. R., Walton, I., Doering, W., Davis, G., Shojaei, B., Natan, M. J. and Gambhir, S. S. Multiplexed imaging of surface enhanced Raman scattering nanotags in living mice using noninvasive Raman spectroscopy. *Proceedings of the National Academy of Sciences of the United States of America* **106**, 13511-13516, (2009).

23. Keren, S., Zavaleta, C., Cheng, Z., de la Zerda, A., Gheysens, O. and Gambhir, S. S. Noninvasive molecular imaging of small living subjects using Raman spectroscopy. *Proceedings of the National Academy of Sciences of the United States of America* **105**, 5844-5849, (2008).

24. Qian, J., Jiang, L., Cai, F., Wang, D. and He, S. Fluorescence-surface enhanced Raman scattering co-functionalized gold nanorods as near-infrared probes for purely optical *in vivo* imaging. *Biomaterials* **32**, 1601-1610, (2011).

25. von Maltzahn, G., Centrone, A., Park, J. H., Ramanathan, R., Sailor, M. J., Hatton, T. A. and Bhatia, S. N. SERS-Coded Gold Nanorods as a Multifunctional Platform for Densely Multiplexed Near-infrared Imaging and Photothermal Heating. *Advanced Materials* **21**, 3175-3180, (2009).

26. Samanta, A., Maiti, K. K., Soh, K. S., Liao, X., Vendrell, M., Dinish, U.

S., Yun, S. W., Bhuvaneswari, R., Kim, H., Rautela, S., Chung, J., Olivo, M. and Chang, Y. T. Ultrasensitive near-infrared Raman reporters for SERS-based in vivo cancer detection. *Angewandte Chemie International Edition* **50**, 6089-6092, (2011).

27. Maiti, K. K., Dinish, U. S., Samanta, A., Vendrell, M., Soh, K. S., Park, S. J., Olivo, M. and Chang, Y. T. Multiplex targeted *in vivo* cancer detection using sensitive near-infrared SERS nanotags. *Nano Today* **7**, 85-93, (2012).

28. Yigit, M. V., Zhu, L., Ifediba, M. A., Zhang, Y., Carr, K., Moore, A. and Medarova, Z. Noninvasive MRI-SERS imaging in living mice using an innately bimodal nanomaterial. *ACS Nano* **5**, 1056-1066, (2011).

29. Zhang, Y., Qian, J., Wang, D., Wang, Y. and He, S. Multifunctional gold nanorods with ultrahigh stability and tunability for in vivo fluorescence imaging, SERS detection, and photodynamic therapy. *Angewandte Chemie International Edition* **52**, 1148-1151, (2013).

30. McVeigh, P. Z., Mallia, R. J., Veilleux, I. and Wilson, B. C. Widefield quantitative multiplex surface enhanced Raman scattering imaging *in vivo*. *Journal of biomedical optics* **18**, 046011, (2013).

31. Zavaleta, C. L., Garai, E., Liu, J. T., Sensarn, S., Mandella, M. J., Van de Sompel, D., Friedland, S., Van Dam, J., Contag, C. H. and Gambhir, S. S. A Raman-based endoscopic strategy for multiplexed molecular imaging. *Proceedings of the National Academy of Sciences of the United States of America* **110**, E2288-E2297, (2013).

32. Bohndiek, S. E., Wagadarikar, A., Zavaleta, C. L., Van de Sompel, D., Garai, E., Jokerst, J. V., Yazdanfar, S. and Gambhir, S. S. A small animal Raman instrument for rapid, wide-area, spectroscopic imaging. *Proceedings of the National Academy of Sciences of the United States of America* **110**, 12408-12413, (2013).

33. Graham, D., Smith, W. E., Linacre, A. M., Munro, C. H., Watson, N. D. and White, P. C. Selective detection of deoxyribonucleic acid at

ultralow concentrations by SERRS. *Analytical Chemistry* **69**, 4703-4707, (1997).

34. Ni, J., Lipert, R. J., Dawson, G. B. and Porter, M. D. Immunoassay readout method using extrinsic Raman labels adsorbed on immunogold colloids. *Analytical Chemistry* **71**, 4903-4908, (1999).

35. Cao, Y. W. C., Jin, R. and Mirkin, C. A. Nanoparticles with Raman spectroscopic fingerprints for DNA and RNA detection. *Science* **297**, 1536-1540, (2002).

36. Mulvaney, S. P., Musick, M. D., Keating, C. D. and Natan, M. J. Glass-coated, analyte-tagged nanoparticles: a new tagging system based on detection with surface-enhanced Raman scattering. *Langmuir* **19**, 4784-4790, (2003).

37. Doering, W. E. and Nie, S. Spectroscopic tags using dye-embedded nanoparticles and surface-enhanced Raman scattering. *Analytical Chemistry* **75**, 6171-6176, (2003).

38. Liu, G. L., Lu, Y., Kim, J., Doll, J. C. and Lee, L. P. Magnetic nanocrescents as controllable surface-enhanced Raman scattering nanoprobes for biomolecular imaging. *Advanced Materials* **17**, 2683-2688, (2005).

39. Kneipp, J., Kneipp, H., McLaughlin, M., Brown, D. and Kneipp, K. In vivo molecular probing of cellular compartments with gold nanoparticles and nanoaggregates. *Nano Letters* **6**, 2225-2231, (2006).

40. Chon, H., Lee, S., Son, S. W., Oh, C. H. and Choo, J. Highly sensitive immunoassay of lung cancer marker carcinoembryonic antigen using surface-enhanced Raman scattering of hollow gold nanospheres. *Analytical Chemistry* **81**, 3029-3034, (2009).

41. Sha, M. Y., Xu, H., Natan, M. J. and Cromer, R. Surface-enhanced Raman scattering tags for rapid and homogeneous detection of circulating tumor cells in the presence of human whole blood. *Journal*

of the American Chemical Society **130**, 17214-17215, (2008).

42. Álvarez-Puebla, R. A., Ross, D. J., Nazri, G. A. and Aroca, R. F. Surface-enhanced Raman scattering on nanoshells with tunable surface plasmon resonance. *Langmuir* **21**, 10504-10508, (2005).

43. Küstner, B., Gellner, M., Schütz, M., Schöppler, F., Marx, A., Ströbel, P., Adam, P., Schmuck, C. and Schlücker, S. SERS labels for red laser excitation: Silica encapsulated SAMs on tunable gold/silver nanoshells. *Angewandte Chemie International Edition* **48**, 1950-1953, (2009).

44. Talley, C. E., Jackson, J. B., Oubre, C., Grady, N. K., Hollars, C. W., Lane, S. M., Huser, T. R., Nordlander, P. and Halas, N. J. Surface-enhanced Raman scattering from individual Au nanoparticles and nanoparticle dimer substrates. *Nano Letters* **5**, 1569-1574, (2005).

45. Jackson, J. B. and Halas, N. J. Surface-enhanced Raman scattering on tunable plasmonic nanoparticle substrates. *Proceedings of the National Academy of Sciences of the United States of America* **101**, 17930-17935, (2004).

46. Kircher, M. F., de la Zerda, A., Jokerst, J. V., Zavaleta, C. L., Kempen, P. J., Mittra, E., Pitter, K., Huang, R., Campos, C. and Habte, F. A brain tumor molecular imaging strategy using a new triple-modality MRI-photoacoustic-Raman nanoparticle. *Nature medicine* **18**, 829-834, (2012).

47. Jokerst, J. V., Cole, A. J., Van de Sompel, D. and Gambhir, S. S. Gold nanorods for ovarian cancer detection with photoacoustic imaging and resection guidance via Raman imaging in living mice. *ACS Nano* **6**, 10366-10377, (2012).

48. Park, H., Lee, S., Chen, L., Lee, E. K., Shin, S. Y., Lee, Y. H., Son, S. W., Oh, C. H., Song, J. M., Kang, S. H. and Choo, J. SERS imaging of HER2-overexpressed MCF7 cells using antibody-conjugated gold nanorods. *Physical Chemistry Chemical Physics* **11**, 7444-7449, (2009).

49. McLellan, J. M., Li, Z.-Y., Siekkinen, A. R. and Xia, Y. The SERS activity of a supported Ag nanocube strongly depends on its orientation relative to laser polarization. *Nano Letters* **7**, 1013-1017, (2007).

50. Narayanan, R., Lipert, R. J. and Porter, M. D. Cetyltrimethylammonium bromide-modified spherical and cube-like gold nanoparticles as extrinsic Raman labels in surface-enhanced Raman spectroscopy based heterogeneous immunoassays. *Analytical Chemistry* **80**, 2265-2271, (2008).

51. Fu, X., Bei, F., Wang, X., Yang, X. and Lu, L. Surface-enhanced Raman scattering of 4-mercaptopyridine on sub-monolayers of α-Fe_2O_3 nanocrystals (sphere, spindle, cube). *Journal of Raman Spectroscopy* **40**, 1290-1295, (2009).

52. Moran, C. H., Rycenga, M., Zhang, Q. and Xia, Y. Replacement of poly (vinyl pyrrolidone) by thiols: A systematic study of Ag nanocube functionalization by surface-enhanced Raman scattering. *The Journal of Physical Chemistry C* **115**, 21852-21857, (2011).

53. Yuan, H., Fales, A. M., Khoury, C. G., Liu, J. and Vo-Dinh, T. Spectral characterization and intracellular detection of Surface-Enhanced Raman Scattering (SERS)-encoded plasmonic gold nanostars. *Journal of Raman Spectroscopy* **44**, 234-239, (2013).

54. Rodríguez-Lorenzo, L., Krpetic, Z., Barbosa, S., Álvarez-Puebla, R. A., Liz-Marzán, L. M., Prior, I. A. and Brust, M. Intracellular mapping with SERS-encoded gold nanostars. *Integrative Biology* **3**, 922-926, (2011).

55. Mulvihill, M. J., Ling, X. Y., Henzie, J. and Yang, P. Anisotropic etching of silver nanoparticles for plasmonic structures capable of single-particle SERS. *Journal of the American Chemical Society* **132**, 268-274, (2010).

56. Xie, J., Zhang, Q., Lee, J. and Wang, D. The synthesis of SERS-active gold nanoflower tags for *in vivo* applications. *ACS Nano* **2**, 2473-2480, (2008).

57. Xu, D., Gu, J., Wang, W., Yu, X., Xi, K. and Jia, X. Development of chitosan-coated gold nanoflowers as SERS-active probes. *Nanotechnology* **21**, 375101, (2010).

58. Yuan, H., Liu, Y., Fales, A. M., Li, Y. L., Liu, J. and Vo-Dinh, T. Quantitative surface-enhanced resonant Raman scattering multiplexing of biocompatible gold nanostars for in vitro and ex vivo detection. *Analytical Chemistry* **85**, 208-212, (2013).

59. Kim, J. H., Kim, J. S., Choi, H., Lee, S. M., Jun, B. H., Yu, K. N., Kuk, E., Kim, Y. K., Jeong, D. H., Cho, M. H. and Lee, Y. S. Nanoparticle probes with surface enhanced Raman spectroscopic tags for cellular cancer targeting. *Analytical Chemistry* **78**, 6967-6973, (2006).

60. Kang, H., Jeong, S., Park, Y., Yim, J., Jun, B.-H., Kyeong, S., Yang, J.-K., Kim, G., Hong, S., Lee, L. P., Kim, J.-H., Lee, H.-Y., Jeong, D. H. and Lee, Y.-S. Near-infrared SERS nanoprobes with plasmonic Au/Ag hollow-shell assemblies for in vivo multiplex detection. *Advanced Functional Materials* **23**, 3719–3727, (2013).

61. Su, X., Zhang, J., Sun, L., Koo, T.-W., Chan, S., Sundararajan, N., Yamakawa, M. and Berlin, A. A. Composite organic-inorganic nanoparticles (COINs) with chemically encoded optical signatures. *Nano Letters* **5**, 49-54, (2005).

62. Huang, P. J., Chau, L. K., Yang, T. S., Tay, L. L. and Lin, T. T. Nanoaggregate-embedded beads as novel Raman labels for biodetection. *Advanced Functional Materials* **19**, 242-248, (2009).

63. Gellner, M., Steinigeweg, D., Ichilmann, S., Salehi, M., Schütz, M., Kömpe, K., Haase, M. and Schlücker, S. 3D self-assembled plasmonic superstructures of gold nanospheres: Synthesis and characterization at the single-particle level. *Small* **7**, 3445-3451, (2011).

64. Yoon, J. H., Lim, J. and Yoon, S. Controlled assembly and plasmonic properties of asymmetric core–satellite nanoassemblies. *ACS Nano* **6**, 7199-7208, (2012).

65. Kim, J. H., Kang, H., Kim, S., Jun, B. H., Kang, T., Chae, J., Jeong, S., Kim, J., Jeong, D. H. and Lee, Y. S. Encoding peptide sequences with surface-enhanced Raman spectroscopic nanoparticles. *Chemical Communications* **47**, 2306-2308, (2011).

66. Kang, H., Kang, T., Kim, S., Kim, J. H., Jun, B. H., Chae, J., Park, J., Jeong, D. H. and Lee, Y. S. Base effects on fabrication of silver nanoparticles embedded silica nanocomposite for surface-enhanced Raman scattering (SERS). *Journal of Nanoscience and Nanotechnology* **11**, 579-583, (2011).

67. Pande, S., Ghosh, S. K., Praharaj, S., Panigrahi, S., Basu, S., Jana, S., Pal, A., Tsukuda, T. and Pal, T. Synthesis of normal and inverted gold-silver core-shell architectures in β-Cyclodextrin and their applications in SERS. *The Journal of Physical Chemistry C* **111**, 10806-10813, (2007).

68. Wang, Z., Zong, S., Li, W., Wang, C., Xu, S., Chen, H. and Cui, Y. SERS-fluorescence joint spectral encoding using organic–metal–QD hybrid nanoparticles with a huge encoding capacity for high-throughput biodetection: putting theory into practice. *Journal of the American Chemical Society* **134**, 2993-3000, (2012).

69. Chung, E., Gao, R., Ko, J., Choi, N., Lim, D. W., Lee, E. K., Chang, S.-I. and Choo, J. Trace analysis of mercury (II) ions using aptamer-modified Au/Ag core–shell nanoparticles and SERS spectroscopy in a microdroplet channel. *Lab on a Chip* **13**, 260-266, (2013).

70. Wang, Y., Yan, B. and Chen, L. SERS tags: novel optical nanoprobes for bioanalysis. *Chemical Reviews* **113**, 1391-1428, (2012).

71. Jun, B. H., Kim, J. H., Park, H., Kim, J. S., Yu, K. N., Lee, S. M., Choi, H., Kwak, S. Y., Kim, Y. K., Jeong, D. H., Cho, M. H. and Lee, Y. S. Surface-enhanced Raman spectroscopic-encoded beads for multiplex immunoassay. *Journal of Combinatorial Chemistry* **9**, 237-244, (2007).

72. Maiti, K. K., Dinish, U., Fu, C. Y., Lee, J.-J., Soh, K.-S., Yun, S.-W.,

Bhuvaneswari, R., Olivo, M. and Chang, Y.-T. Development of biocompatible SERS nanotag with increased stability by chemisorption of reporter molecule for *in vivo* cancer detection. *Biosensors and Bioelectronics* **26**, 398-403, (2010).

73. Sun, L., Sung, K.-B., Dentinger, C., Lutz, B., Nguyen, L., Zhang, J., Qin, H., Yamakawa, M., Cao, M., Lu, Y., Chmura, A., Zhu, J., Su, X., Berlin, A. A., Selena Chan and Knudsen, B. Composite organic-inorganic nanoparticles as Raman labels for tissue analysis. *Nano Letters* **7**, 351-356, (2007).

74. Jun, B.-H., Kang, H., Lee, Y.-S. and Jeong, D. H. Fluorescence-based multiplex protein detection using optically encoded microbeads. *Molecules* **17**, 2474-2490, (2012).

75. Gellner, M., Küstner, B. and Schlücker, S. Multiplexing with SERS labels using mixed SAMs of Raman reporter molecules. *Analytical and Bioanalytical Chemistry* **394**, 1839-1844, (2009).

76. Sun, L., Yu, C. and Irudayaraj, J. Raman multiplexers for alternative gene splicing. *Analytical Chemistry* **80**, 3342-3349, (2008).

77. Lam, K. S., Lebl, M. and Krchnák, V. The "one-bead-one-compound" combinatorial library method. *Chemical Reviews* **97**, 411-448, (1997).

78. Lam, K. S., Salmon, S. E., Hersh, E. M., Hruby, V. J., Kazmierski, W. M. and Knapp, R. J. A new type of synthetic peptide library for identifying ligand-binding activity. *Nature* **354**, 82-84, (1991).

79. Aina, O. H., Liu, R. W., Sutcliffe, J. L., Marik, J., Pan, C. X. and Lam, K. S. From combinatorial chemistry to cancer-targeting peptides. *Molecular Pharmaceutics* **4**, 631-651, (2007).

80. Rinnová, M. and Lebl, M. Molecular diversity and libraries of structures: Synthesis and screening. *Collection of Czechoslovak Chemical Communications* **61**, 171-231, (1996).

81. Terrett, N. K., Gardner, M., Gordon, D. W., Kobylecki, R. J. and Steele,

J. Combinatorial synthesis - the design of compound libraries and their application to drug discovery. *Tetrahedron* **51**, 8135-8173, (1995).

82. Wilson, R., Cossins, A. R. and Spiller, D. G. Encoded Microcarriers For High-Throughput Multiplexed Detection. *Angewandte Chemie International Edition* **45**, 6104-6117, (2006).

83. Braeckmans, K., De Smedt, S. C., Leblans, M., Pauwels, R. and Demeester, J. Encoding microcarriers: present and future technologies. *Nature Reviews Drug Discovery* **1**, 447-456, (2002).

84. Czarnik, A. Encoding strategies in combinatorial chemistry. *Proceedings of the National Academy of Sciences of the United States of America* **94**, 12738-12739, (1997).

85. Egner, B. J., Rana, S., Smith, H., Bouloc, N., Frey, J. G., Brocklesby, W. S. and Bradley, M. Tagging in combinatorial chemistry: The use of coloured and fluorescent beads. *Chemical Communications*, 735-736, (1997).

86. Fenniri, H., Chun, S., Ding, L. H., Zyrianov, Y. and Hallenga, K. Preparation, physical properties, on-bead binding assay and spectroscopic reliability of 25 barcoded polystyrene-poly(ethylene glycol) graft copolymers. *Journal of the American Chemical Society* **125**, 10546-10560, (2003).

87. Fenniri, H., Chun, S., Terreau, O. and Bravo-Vasquez, J. P. Preparation and infrared/Raman classification of 630 spectroscopically encoded styrene copolymers. *Journal of Combinatorial Chemistry* **10**, 31-36, (2008).

88. Fenniri, H., Ding, L. H., Ribbe, A. E. and Zyrianov, Y. Barcoded resins: A new concept for polymer-supported combinatorial library self-deconvolution. *Journal of the American Chemical Society* **123**, 8151-8152, (2001).

89. Kim, S. H., Shim, J. W. and Yang, S. M. Microfluidic multicolor

encoding of microspheres with nanoscopic surface complexity for multiplex immunoassays. *Angewandte Chemie International Edition* **50**, 1171-1174, (2011).

90. Zhi, Z.-l., Morita, Y., Hasan, Q. and Tamiya, E. Micromachining microcarrier-based biomolecular encoding for miniaturized and multiplexed immunoassay. *Analytical Chemistry* **75**, 4125-4131, (2003).

91. Chung, S. E., Park, W., Park, H., Yu, K., Park, N. and Kwon, S. Optofluidic maskless lithography system for real-time synthesis of photopolymerized microstructures in microfluidic channels. *Applied Physics Letters* **91**, 041106, (2007).

92. Chen, H.-Y., Rouillard, J.-M., Gulari, E. and Lahann, J. Colloids with high-definition surface structures. *Proceedings of the National Academy of Sciences of the United States of America* **104**, 11173-11178, (2007).

93. Braeckmans, K., De Smedt, S. C., Roelant, C., Leblans, M., Pauwels, R. and Demeester, J. Encoding microcarriers by spatial selective photobleaching. *Nature Materials* **2**, 169-173, (2003).

94. Nicewarner-Pena, S. R., Freeman, R. G., Reiss, B. D., He, L., Peña, D. J., Walton, I. D., Cromer, R., Keating, C. D. and Natan, M. J. Submicrometer metallic barcodes. *Science* **294**, 137-141, (2001).

95. Michael, Y. S., Walton, I. D., Norton, S. M., Taylor, M., Yamanaka, M., Natan, M. J., Xu, C., Drmanac, S., Huang, S., Borcherding, A., Drmanac, R. and Penn, S. G. Multiplexed SNP genotyping using nanobarcode particle technology. *Analytical and Bioanalytical Chemistry* **384**, 658-666, (2006).

96. Evans, M., Sewter, C. and Hill, E. An encoded particle array tool for multiplex bioassays. *Assay and Drug Development Technologies* **1**, 199-207, (2003).

97. Pregibon, D. C., Toner, M. and Doyle, P. S. Multifunctional encoded

particles for high-throughput biomolecule analysis. *Science* **315**, 1393-1396, (2007).

98. Battersby, B. J., Bryant, D., Meutermans, W., Matthews, D., Smythe, M. L. and Trau, M. Toward larger chemical libraries: Encoding with fluorescent colloids in combinatorial chemistry. *Journal of the American Chemical Society* **122**, 2138-2139, (2000).

99. Grondahl, L., Battersby, B. J., Bryant, D. and Trau, M. Encoding combinatorial libraries: A novel application of fluorescent silica colloids. *Langmuir* **16**, 9709-9715, (2000).

100. Marcon, L., Spriet, C., Meehan, T. D., Battersby, B. J., Lawrie, G. A., Heliot, L. and Trau, M. Synthesis and application of FRET nanoparticles in the profiling of a protease. *Small* **5**, 2053-2056, (2009).

101. Marcon, L., Battersby, B. J., Ruhmann, A., Ford, K., Daley, M., Lawrie, G. A. and Trau, M. 'On-the-fly' optical encoding of combinatorial peptide libraries for profiling of protease specificity. *Molecular BioSystems* **6**, 225-233, (2010).

102. Eastman, P. S., Ruan, W., Doctolero, M., Nuttall, R., de Feo, G., Park, J. S., Chu, J. S., Cooke, P., Gray, J. W., Li, S. and Chen, F. F. Qdot nanobarcodes for multiplexed gene expression analysis. *Nano Letters* **6**, 1059-1064, (2006).

103. Han, M., Gao, X., Su, J. Z. and Nie, S. Quantum-dot-tagged microbeads for multiplexed optical coding of biomolecules. *Nature Biotechnology* **19**, 631-635, (2001).

104. Cunin, F., Schmedake, T. A., Link, J. R., Li, Y. Y., Koh, J., Bhatia, S. N. and Sailor, M. J. Biomolecular screening with encoded porous-silicon photonic crystals. *Nature Materials* **1**, 39-41, (2002).

105. Lee, H., Kim, J., Kim, H., Kim, J. and Kwon, S. Colour-barcoded magnetic microparticles for multiplexed bioassays. *Nature Materials* **9**, 745-749, (2010).

106. Battersby, B. J., Lawrie, G. A., Johnston, A. P. R. and Trau, M. Optical barcoding of colloidal suspensions: applications in genomics, proteomics and drug discovery. *Chemical Communications*, 1435-1441, (2002).

107. Brindle, K. New approaches for imaging tumour responses to treatment. *Nature Reviews Cancer* **8**, 94-107, (2008).

108. Willmann, J. K., van Bruggen, N., Dinkelborg, L. M. and Gambhir, S. S. Molecular imaging in drug development. *Nature Reviews Drug Discovery* **7**, 591-607, (2008).

109. Lyons, S. K. Advances in imaging mouse tumour models in vivo. *The Journal of pathology* **205**, 194-205, (2005).

110. Montet, X., Ntziachristos, V., Grimm, J. and Weissleder, R. Tomographic fluorescence mapping of tumor targets. *Cancer Research* **65**, 6330-6336, (2005).

111. Weissleder, R. A clearer vision for in vivo imaging. *Nature Biotechnology* **19**, 316-317, (2001).

112. Weissleder, R., Tung, C. H., Mahmood, U. and Bogdanov, A. In vivo imaging of tumors with protease-activated near-infrared fluorescent probes. *Nature Biotechnology* **17**, 375-378, (1999).

113. Kobayashi, H., Koyama, Y., Barrett, T., Hama, Y., Regino, C. A. S., Shin, I. S., Jang, B. S., Le, N., Paik, C. H., Choyke, P. L. and Urano, Y. Multimodal nanoprobes for radionuclide and five-color near-infrared optical lymphatic imaging. *ACS Nano* **1**, 258-264, (2007).

114. Barone, P. W., Baik, S., Heller, D. A. and Strano, M. S. Near-infrared optical sensors based on single-walled carbon nanotubes. *Nature Materials* **4**, 86-92, (2005).

115. Kim, J. H., Heller, D. A., Jin, H., Barone, P. W., Song, C., Zhang, J., Trudel, L. J., Wogan, G. N., Tannenbaum, S. R. and Strano, M. S. The rational design of nitric oxide selectivity in single-walled carbon

nanotube near-infrared fluorescence sensors for biological detection. *Nature Chemistry* **1**, 473-481, (2009).

116. Welsher, K., Liu, Z., Sherlock, S. P., Robinson, J. T., Chen, Z., Daranciang, D. and Dai, H. A route to brightly fluorescent carbon nanotubes for near-infrared imaging in mice. *Nature Nanotechnology* **4**, 773-780, (2009).

117. Kim, S., Lim, Y. T., Soltesz, E. G., De Grand, A. M., Lee, J., Nakayama, A., Parker, J. A., Mihaljevic, T., Laurence, R. G., Dor, D. M., Cohn, L. H., Bawendi, M. G. and Frangioni, J. V. Near-infrared fluorescent type II quantum dots for sentinel lymph node mapping. *Nature Biotechnology* **22**, 93-97, (2004).

118. Choi, H. S., Ipe, B. I., Misra, P., Lee, J. H., Bawendi, M. G. and Frangioni, J. V. Tissue-and organ-selective biodistribution of NIR fluorescent quantum dots. *Nano Letters* **9**, 2354-2359, (2009).

119. Grubisha, D. S., Lipert, R. J., Park, H. Y., Driskell, J. and Porter, M. D. Femtomolar detection of prostate-specific antigen: an immunoassay based on surface-enhanced Raman scattering and immunogold labels. *Analytical Chemistry* **75**, 5936-5943, (2003).

120. Schlücker, S., Küstner, B., Punge, A., Bonfig, R., Marx, A. and Ströbel, P. Immuno-Raman microspectroscopy: In situ detection of antigens in tissue specimens by surface-enhanced Raman scattering. *Journal of Raman Spectroscopy* **37**, 719-721, (2006).

121. Lee, S., Kim, S., Choo, J., Shin, S. Y., Lee, Y. H., Choi, H. Y., Ha, S., Kang, K. and Oh, C. H. Biological imaging of HEK293 cells expressing PLCγ1 using surface-enhanced Raman microscopy. *Analytical Chemistry* **79**, 916-922, (2007).

122. Jun, B. H., Noh, M. S., Kim, J., Kim, G., Kang, H., Kim, M. S., Seo, Y. T., Baek, J., Kim, J. H., Park, J., Kim, S., Kim, Y. K., Hyeon, T., Cho, M. H., Jeong, D. H. and Lee, Y. S. Multifunctional silver-embedded magnetic nanoparticles as SERS nanoprobes and their applications.

Small **6**, 119-125, (2010).

123. Kim, K., Choi, J. Y., Lee, H. B. and Shin, K. S. Silanization of Ag-deposited magnetite particles: An efficient route to fabricate magnetic nanoparticle-based Raman barcode materials. *ACS Applied Materials & Interfaces* **2**, 1872-1878, (2010).

124. Li, J. F., Huang, Y. F., Ding, Y., Yang, Z. L., Li, S. B., Zhou, X. S., Fan, F. R., Zhang, W., Zhou, Z. Y., Wu, D. Y., Ren, B., Wang, Z. L. and Tian, Z. Q. Shell-isolated nanoparticle-enhanced Raman spectroscopy. *Nature* **464**, 392-395, (2010).

125. Pallaoro, A., Braun, G. B., Reich, N. O. and Moskovits, M. Mapping local pH in live cells using encapsulated fluorescent SERS nanotags. *Small* **6**, 618-622, (2010).

126. Qian, X., Peng, X. H., Ansari, D. O., Yin-Goen, Q., Chen, G. Z., Shin, D. M., Yang, L., Young, A. N., Wang, M. D. and Nie, S. M. In vivo tumor targeting and spectroscopic detection with surface-enhanced Raman nanoparticle tags. *Nature Biotechnology* **26**, 83-90, (2008).

127. Xie, H. n., Stevenson, R., Stone, N., Hernandez-Santana, A., Faulds, K. and Graham, D. Tracking bisphosphonates through a 20 mm thick porcine tissue by using surface-enhanced spatially offset Raman spectroscopy. *Angewandte Chemie International Edition* **51**, 8509-8511, (2012).

128. McKenzie, F., Ingram, A., Stokes, R. and Graham, D. SERRS coded nanoparticles for biomolecular labelling with wavelength-tunable discrimination. *Analyst* **134**, 549-556, (2009).

129. Liu, X. W., Lin, J., Jiang, T. F., Zhu, Z. F., Zhan, Q. Q., Qian, J. and He, S. Surface plasmon properties of hollow AuAg alloyed triangular nanoboxes and its applications in SERS imaging and potential drug delivery. *Progress In Electromagnetics Research* **128**, 35-53, (2012).

130. Oldenburg, S., Averitt, R., Westcott, S. and Halas, N. Nanoengineering

of optical resonances. *Chemical Physics Letters* **288**, 243-247, (1998).

131. Jackson, J. and Halas, N. Silver nanoshells: variations in morphologies and optical properties. *The Journal of Physical Chemistry B* **105**, 2743-2746, (2001).

132. Skrabalak, S. E., Au, L., Li, X. and Xia, Y. Facile synthesis of Ag nanocubes and Au nanocages. *Nature Protocols* **2**, 2182-2190, (2007).

133. Chen, J., Wiley, B., Li, Z. Y., Campbell, D., Saeki, F., Cang, H., Au, L., Lee, J., Li, X. and Xia, Y. Gold nanocages: engineering their structure for biomedical applications. *Advanced Materials* **17**, 2255-2261, (2005).

134. Dong, A., Wang, Y., Tang, Y., Ren, N., Yang, W. and Gao, Z. Fabrication of compact silver nanoshells on polystyrene spheres through electrostatic attraction. *Chemical Communications*, 350-351, (2002).

135. Liang, Z., Susha, A. S. and Caruso, F. Metallodielectric opals of layer-by-layer processed coated colloids. *Advanced Materials* **14**, 1160, (2002).

136. Wu, Q., Zhang, C. and Li, F. Preparation of spindle-shape silver core-shell particles. *Materials Letters* **59**, 3672-3677, (2005).

137. Yong, K.-T., Sahoo, Y., Swihart, M. T. and Prasad, P. N. Synthesis and plasmonic properties of silver and gold nanoshells on polystyrene cores of different size and of gold–silver core–shell nanostructures. *Colloids and Surfaces, A: Physicochemical and Engineering Aspects* **290**, 89-105, (2006).

138. Jiang, Z.-j. and Liu, C.-y. Seed-mediated growth technique for the preparation of a silver nanoshell on a silica sphere. *The Journal of Physical Chemistry B* **107**, 12411-12415, (2003).

139. Kim, J.-H., Bryan, W. W. and Randall Lee, T. Preparation, characterization, and optical properties of gold, silver, and gold−silver alloy nanoshells having silica cores. *Langmuir* **24**, 11147-11152, (2008).

140. Long, S., Li, L., Guo, H., Yang, W. and Lu, F. Preparation of stable core-shell dye adsorbent Ag-coated silica nanospheres as a highly active surfaced-enhanced Raman scattering substrate for detection of Rhodamine 6G. *Dyes and Pigments*, (2012).

141. Zhang, J., Liu, J., Wang, S., Zhan, P., Wang, Z. and Ming, N. Facile methods to coat polystyrene and silica colloids with metal. *Advanced Functional Materials* **14**, 1089-1096, (2004).

142. Chen, L., Han, X., Yang, J., Zhou, J., Song, W., Zhao, B., Xu, W. and Ozaki, Y. Detection of proteins on Silica–Silver Core–Shell substrates by surface-enhanced Raman spectroscopy. *Journal of Colloid and Interface Science* **360**, 482-487, (2011).

143. Zhang, C., Zhu, X., Li, H., Khan, I., Imran, M., Wang, L., Bao, J. and Cheng, X. Controllable fabrication of PS/Ag core-shell-shaped nanostructures. *Nanoscale research letters* **7**, 580, (2012).

144. Liu, T., Li, D., Yang, D. and Jiang, M. An improved seed-mediated growth method to coat complete silver shells onto silica spheres for surface-enhanced Raman scattering. *Colloids and Surfaces A: Physicochemical and Engineering Aspects* **387**, 17-22, (2011).

145. Zhang, J., Liu, H., Wang, Z. and Ming, N. A solvent-assisted route for coating polystyrene colloids with Ag and the corresponding hollow Ag spheres. *Materials Letters* **61**, 4579-4582, (2007).

146. Pol, V. G., Srivastava, D., Palchik, O., Palchik, V., Slifkin, M., Weiss, A. and Gedanken, A. Sonochemical deposition of silver nanoparticles on silica spheres. *Langmuir* **18**, 3352-3357, (2002).

147. Kalele, S., Ashtaputre, S., Hebalkar, N., Gosavi, S., Deobagkar, D., Deobagkar, D. and Kulkarni, S. Optical detection of antibody using silica–silver core–shell particles. *Chemical Physics Letters* **404**, 136-141, (2005).

148. Tang, S., Tang, Y., Zhu, S., Lu, H. and Meng, X. Synthesis and

characterization of silica–silver core–shell composite particles with uniform thin silver layers. *Journal of Solid State Chemistry* **180**, 2871-2876, (2007).

149. Tian, C., Wang, E., Kang, Z., Mao, B., Zhang, C., Lan, Y., Wang, C. and Song, Y. Synthesis of Ag-coated polystyrene colloids by an improved surface seeding and shell growth technique. *Journal of Solid State Chemistry* **179**, 3270-3276, (2006).

150. Flores, J. C., Torres, V., Popa, M., Crespo, D. and Calderón-Moreno, J. M. Variations in morphologies of silver nanoshells on silica spheres. *Colloids and Surfaces A: Physicochemical and Engineering Aspects* **330**, 86-90, (2008).

151. Wang, H., Goodrich, G. P., Tam, F., Oubre, C., Nordlander, P. and Halas, N. J. Controlled texturing modifies the surface topography and plasmonic properties of Au nanoshells. *The Journal of Physical Chemistry B* **109**, 11083-11087, (2005).

152. Chan, W. C. and White, P. D. *Fmoc solid phase peptide synthesis : a practical approach*. (Oxford University Press, 2000).

153. Jiang, P., Deng, K., Fichou, D., Xie, S. S., Nion, A. and Wang, C. STM Imaging ortho-and para-Fluorothiophenol Self-Assembled Monolayers on Au (111). *Langmuir* **25**, 5012-5017, (2009).

154. Etchegoin, P. G., Le Ru, E. C. and Meyer, M. An analytic model for the optical properties of gold. *The Journal of chemical physics* **125**, 164705, (2006).

155. Hao, E. and Schatz, G. C. Electromagnetic fields around silver nanoparticles and dimers. *The Journal of chemical physics* **120**, 357, (2004).

156. Grosges, T., Vial, A. and Barchiesi, D. Models of near-field spectroscopic studies: comparison between Finite-Element and Finite-Difference methods. *Optics express* **13**, 8483-8497, (2005).

157. Seo, D. and Song, H. Asymmetric hollow nanorod formation through a partial galvanic replacement reaction. *Journal of the American Chemical Society* **131**, 18210-18211, (2009).

158. Álvarez-Puebla, R. A. Effects of the excitation wavelength on the SERS spectrum. *The Journal of Physical Chemistry Letters* **3**, 857-866, (2012).

159. Fang, Y., Seong, N. H. and Dlott, D. D. Measurement of the distribution of site enhancements in surface-enhanced Raman scattering. *Science* **321**, 388-392, (2008).

160. Newman, J. and Blanchard, G. Formation of gold nanoparticles using amine reducing agents. *Langmuir* **22**, 5882-5887, (2006).

161. Naka, K. and Chujo, Y. in *Nanohybridization of Organic-Inorganic Materials* 3-40 (Springer, 2009).

162. Jun, B. H., Kim, G., Baek, J., Kang, H., Kim, T., Hyeon, T., Jeong, D. H. and Lee, Y. S. Magnetic field induced aggregation of nanoparticles for sensitive molecular detection. *Physical Chemistry Chemical Physics* **13**, 7298-7303, (2011).

163. Carter, M. J., Rillema, D. P. and Basolo, F. Oxygen carrier and redox properties of some neutral cobalt chelates. Axial and in-plane ligand effects. *Journal of the American Chemical Society* **96**, 392-400, (1974).

164. Sivagnanam, U. and Palaniandavar, M. Influence of chelate-ring size and number of sulfur-donor atoms on spectra and redox behaviour of copper (II) bis (benzimidazolyl) tetra-and penta-thloether complexes. *Journal of the Chemical Society, Dalton Transactions: Inorganic Chemistry*, 2277-2283, (1994).

165. Wang, H., Fu, K., Drezek, R. and Halas, N. Light scattering from spherical plasmonic nanoantennas: effects of nanoscale roughness. *Applied Physics B* **84**, 191-195, (2006).

166. Tiwari, D. K., Jin, T. and Behari, J. Dose-dependent in-vivo toxicity

assessment of silver nanoparticle in Wistar rats. *Toxicology Mechanisms and Methods* **21**, 13-24, (2011).

167. Jun, B.-H., Hwang, D. W., Jung, H. S., Jang, J., Kim, H., Kang, H., Kang, T., Kyeong, S., Lee, H., Jeong, D. H., Kang, K. W., Youn, H., Lee, D. S. and Lee, Y.-S. Ultrasensitive, biocompatible, quantum-dot-embedded silica nanoparticles for bioimaging. *Advanced Functional Materials* **22**, 1843-1849, (2012).

요약 (국문 초록)

인코딩과 체내/외 다중 검출을 위한 표면 증강 라만 산란 활성
플라즈모닉 나노입자에 관한 연구

강호만
협동과정 나노과학기술 전공
서울대학교 대학원

바이오 응용 분야에서 다중 분석을 위해선 여러 가지 대상 물질을 동시에 검출하기 위한 다중 신호를 내는 프로브가 필요한데, 이러한 프로브는 신호간 중첩이 적어야 할 뿐만 아니라, 미량의 생체표지자를 대상으로 하여 정량이 가능하고 측정 민감도가 높아야 한다. 현재 가장 많이 사용하고 있는 형광 프로브 및 양자점(Quantum dot)은 신호 대역폭(bandwidth)이 넓어서 여러 신호를 동시에 서로 구별하기 어려울 뿐 아니라, 체내 자가 발광 현상으로 인한 민감도 저하, 별개의 광원을 사용해야 하는 번거로움 등 제한요소가 다수 존재하게 된다. 최근 다중 분석의 필요성이 강조되면서 다양한 방법이 제안되어 왔는데, 특히 신호 민감도가 뛰어난 것으로 알려진 광신호를 이용한 다중 정량 분석 기술은 아직까지 많은 개발이 이루어지지 않아 주목 받는 기술이라 할 수 있다. 광신호를 이용한 다중 분석 방법 중 라만 산란 신호는 형광에 비해 100배 이상 좁은 신호대역폭을 가지므로 가장 우수한 다중 신호표지 방법으로 인정받고 있으며, 나노 플라즈모닉스를 기반으로 한 표면 증강 라만 산란(SERS, Surface-enhanced Raman Scattering) 신호를 이용하면 형광에 준하는 신호 민감도를 얻을 수 있게 된다.

본 논문에서는 펩타이드 인코딩 및 체내에서 다중 검출을 위한 표면 증강 라만 나노입자들(SERS probe/dot)의 개발 및 표지 방법을 고안하였다.

첫째로 간단하고 효과적인 표면 증강 라만 산란 기반의 펩타이드 인코딩 방법을 개발 하였다. 진단 시약 선도물질을 탐색하기 위해 가장 많이 사용되고 있는 방법에는 레진 비드를 이용한 조합화학 방법이 있으며, 비교적 손쉽게 수백만 종류의 화합물 혹은 펩타이드 등의 라이브러리를 합성하고, 이러한 라이브러리로부터 생물학적 분석을 통해 진단 시약 선도 물질을 발굴해 낸다. 진단 시약 탐색은 매우 많은 수를 대상으로 분석 해야 하기 때문에, 이러한 일련의 작업을 보다 쉽고 빠르게 하기 위해서는 수백만 개의 표적을 효율적으로 표지하고 탐색하는 인코딩 기술이 요구된다. Fmoc 합성법을 이용하여 펩타이드를 텐타젤 비드(35 μm)에 합성하였다. 펩타이드를 합성하는 과정에서 텐타젤 비드에 여러 종류의 신호를 내는 SERS dot을 조합하여 인코딩하였고, 이러한 인코딩은 SERS dot이 마이크로 비드 표면에 물리적인 흡착을 함으로서 이루어 졌다. 마이크로 비드는 2종류의 SERS dot을 조합하여 인코딩 할 경우, 이론적으로 약 10,000 개 이상의 각기 다른 코드를 부여할 수 있다. SERS dot을 이용한 인코딩의 경우의 장점은 다음과 같다. 몇 종류의 라만 표지 화합물부터도 수 많은 수의 코드를 만들 수 있고, 라만 신호의 선 폭이 매우 좁아 신호간의 겹침이 거의 없고, 하나의 레이져 광원으로 여러 종류의 신호를 동시에 읽어낼 수 있다.

둘째로는 약 125 nm 크기의 실리카 나노입자 표면에 수 십 개의 은 나노입자를 도입하고, 이를 금 이온과의 환원력 차이를 이용해 속이 빈 금/은 합금 나노 구조체를 만들었다. 이때 넣어준 금 이온

의 양에 따라 점차적으로 속이 빈 구조체가 형성됨을 확인하였고, 속이 빈 나노 구조체가 형성됨에 따라 나노프로브의 최대 흡광 파장이 최초 490 nm 영역에서 최대 840 nm 영역까지 적색 편이 (red shift) 하게 되었다. 따라서, 근적외선 영역에서 민감한 나노프로브는 금 이온 전구체의 양을 조절함으로써 신호의 세기를 최적할 수 있었고, 최적화 된 나노프로브는 근적외선 광원 (785 nm)을 사용하여 SERS 스펙트럼을 측정하였을 경우, 은 나노입자로 구성된 초기 상태와 비교하여 약 4 배 가량의 신호 증가효과가 있었다. 이렇게 제조된 나노프로브는 근적외선 영역의 빛을 사용하였을 때 도입된 분자의 라만 산란신호가 약 10^5 배 증가되었고, 이렇게 증강된 라만 신호로 인해 각각의 개별 나노프로브에서도 라만신호를 검출 할 수 있었다. 이것과는 대조적으로 기존에 주로 사용하던 구형의 금 나노입자(80 nm)에서는 각각의 개별 나노입자 수준에서는 라만 신호를 얻을 수 없었다. 개별 나노프로브의 신호 특성을 살펴보았을 때 개발된 나노프로브는 신호의 세기뿐만 아니라, ensemble average 효과로 인해 신호의 균일성 또한 비교적 우수한 것으로 관측되어 추후 정량적인 분석을 더욱 용이하게 할 수 있는 가능성을 나타내었다. 또한, 개발된 근적외선 민감 나노프로브를 살아있는 실험 쥐에 주입하였고, 라만 측정 장치를 사용하여 실험 쥐의 체내에 존재하는 나노프로브의 신호를 측정하는데 성공하였다. 더 나아가 예시로써 세 가지 종류의 서로 다른 나노 프로브를 생체 내에 동시 주입하여, 각각의 특정 신호가 구별될 수 있음을 보여 줌으로써 다수의 대상 물질에 선택적으로 결합한 각각의 나노 프로브를 동시에 분석해 낼 수 있음을 보였다.

마지막으로 은 나노쉘 기반의 근적외선 라만 표지 나노입자를 개발하였다. 실리카나노 중심입자와 은나노 껍질 구조로 이루어져 있

는 은 나노쉘은 우수한 라만 증강 효과와 가시광영역에서 근적외선 영역까지 표면 플라즈몬 파장이 쉽게 변조될 수 있기 때문에 현재 많은 주목을 받고 있다. 하지만 현재까지 알려진 은 나노쉘을 만드는 방법은 상대적으로 복잡한 합성과정이 문제가 되어왔다. 본 논문에서는 은 나노쉘기반의 근적외선에서 민감한 표면증강라만 산란 나노입자를 복잡한 과정이나, 금속 씨앗이 없이 만드는 방법을 고안하였다. 제조된 은 나노쉘표면은 울퉁불퉁한 모양으로 실리카 표면을 완전히 덥고 있었으며, 은 나노쉘의 두께는 약 32 nm에서 76 nm까지 쉽게 조절 가능하였다. 은나노쉘 기반의 근적외선 민감 표면 증강 라만 산란 나노입자는 우수한 라만 신호세기를 나타내었고, 증강 인수는 6.4×10^5 이었다. 또한, 이 나노 프로브를 세포 내로 흡입시키고, 이를 살아 있는 쥐의 조직에 주입하고, 추적한 결과 살아있는 쥐의 생체조직 내에서도 3일 가량 추적이 가능함을 보였다.

주요어 : 표면 증강 라만 산란, 표면 증강 라만 산란 나노입자, 나노프로브, 클러스터, 어셈블리, 금/은 할로우쉘, 나노쉘, 범피 나노구조체, 다중 검출, 광학 인코딩, 펩타이드 인코딩, 바이오 이미징, 근적외선 이미징, 단일 입자 검출, 세포 추적

학 번 : 2007-20461